Anti-aging and avalanche dynamics in ultrastable metallic glasses by X-ray photon correlation spectroscopy

Dissertation

for the award of the degree
"Doctor rerum naturalium" (Dr. rer. nat.)
of the Georg-August-Universität Göttingen

within the doctoral program Physik
of the Georg-August University School of Science (GAUSS)

submitted by
Martin Lüttich
from Blankenburg (Harz)

Göttingen, 2023

Thesis committee

Prof. Dr. Konrad Samwer
I. Physikalisches Institut, Georg-August-Universität Göttingen

Dr. Beatrice Ruta
Light Matter Institute, UMR5306, Université Lyon 1

Prof. Dr. Matthias Krüger
Institut für Theoretische Physik, Georg-August-Universität Göttingen

Members of the examination board

Reviewer:
Prof. Dr. Konrad Samwer
I. Physikalisches Institut, Georg-August-Universität Göttingen

Second reviewer:
Prof. Dr. Matthias Krüger
Institut für Theoretische Physik, Georg-August-Universität Göttingen

Further members of the examination board

Dr. Beatrice Ruta
Light Matter Institute, UMR5306, Université Lyon 1

Prof. Dr. Michael Seibt
IV. Physikalisches Institut, Georg-August-Universität Göttingen

Prof. Dr. Vasily Moshnyaga
I. Physikalisches Institut, Georg-August-Universität Göttingen

Prof. Cynthia A. Volkert, PhD
Institut für Materialphysik, Georg-August-Universität Göttingen

Date of the oral examination: 9 May 2023

τα πάντα ρει!

Abstract

Within this thesis, structural relaxation dynamics of vapour deposited as well as conventionally produced metallic glasses are studied. Vapour deposition enables to crucially tune the surface diffusion during the deposition process, so metallic glasses with much lower potential energy can be fabricated – so-called ultrastable metallic glasses (UMGs). X-ray photon correlation spectroscopy (XPCS) studies of UMGs reveal a particular anti-aging behaviour upon annealing, which underlines the intrinsic low potential energy of UMGs. Furthermore, a new data processing method was developed in order to analyse the statistics of relaxation time changes along with the evolution of the relaxation behaviour, uncovering evidence for avalanche-like dynamics upon non-directional excitation of local rearrangements in annealed vapour deposited metallic glasses.

Contents

List of Figures

List of Tables

Acronyms

ACS alternative coordinate system

ADU analogue-to-digital unit

AFM atomic force microscopy

ap as-prepared

CCS conventional coordinate system

CCD charge-coupled device

DESY Deutsches Elektronen-Synchrotron

DLS dynamical light scattering

DMA dynamical mechanical analysis

DSC differential scanning calorimetry

EBS Extremely Brilliant Source

ECM electron correlation microscopy

EH experimental hutch

ESRF European Synchrotron Radiation Facility

EDX energy-dispersive X-ray spectroscopy

FEM fluctuation electron microscopy

FQ fast quenched

FFT Fast Fourier Transformation

FSDP first sharp diffraction peak

FT Fourier transformation

FWHM full width half maximum

ISF intermediate scattering function

KWW Kohlrausch-Williams-Watts

MD molecular dynamics

MG metallic glass

OH optics hutch

PCS photon correlation spectroscopy

PDF pair distribution function

PEL potential energy landscape

PID proportional-integral-derivative

ROI region of interest

SCL supercooled liquid

SEM scanning electron microscope

SNR signal-to-noise ratio

STZ shear transformation zone

TTCF two-time correlation function

UMG ultrastable metallic glass

USG ultrastable glass

X-FEL X-ray free electron laser

VD vapour deposited

XPCS X-ray photon correlation spectroscopy

XRD X-ray diffraction

Symbols

Characters, set in bold font, denote mathematical vectors.

$\mathcal{B}$ brilliance

ξ_l longitudinal coherence length

ξ_l longitudinal coherence length

c_p specific heat capacity

$f(\boldsymbol{q}, t)$ intermediate scattering function

$g(r)$ radial distribution function

$\langle g^{(2)}(t) \rangle_{t_\mathrm{exp}}$ intensity auto-correlation function

δs path length difference

$n(\boldsymbol{r})$ scatterer number density

$S(q)$ static structure factor

$S(\boldsymbol{q})$ static structure factor

T_a annealing temperature

T_f fictive temperature

T_g glass transition temperature

T_sub substrate temperature

T_x crystallisation temperature

Chapter 1

Introduction

Glasses. Brightening the sites of human shelter, they are more than just a separator between inside and outside. While this is most likely a description of glass most people would agree on, indeed glasses span an entire class of materials. Glasses may be polymers such as polyvinlychloride (PVC), polycarboante [BBH69] or polymethylmethacrylate (PMMA) [Fin16], network glasses as for instance composed of SiO_2 [Mic16], chalcogenide glasses [Bur+04], organic glasses such as indomethacin (IMC), toluene or ethylbenzene [Woj+09; Ell90], metallic glasses such as AuSi or CuZr [KWD60; PDG78; WLG05] and many other types. Despite their chemical differences, under certain conditions they can all be subjected to glass formation upon cooling from the melt. However, the cooling rate necessary to omit crystallisation crucially depends on the chemical nature of the glass former [Ell90]. When entering the glassy state, a glass former falls out of thermodynamic equilibrium, reaching a metastable state, featured throughout the lag of long-range order. The nature of this state gives rise to spontaneous changes of the physical and chemical properties of a glass, summarised under the term *aging* [Kov64; Str77; Hod95; KB97]. Although known for over half a century, the underlying mechanisms of aging are still unknown and under vibrant debate [Pas+19; Rie+22; Zha+22].

A new kind of glasses was introduced when the first report on an ultrastable glass (USG) was published displaying exceptional thermodynamic and kinetic stability [Swa+07]. Throughout a new preparation technique, a glass former is deposited by means of physical vapour deposition onto a substrate

while particular process parameters have to be adjusted. After their discovery, ultrastable glasses (USGs) of different types of glasses attracted interest in the scientific community, spanning from organic [Kea+08], to chalcogenide [Zha+17], and subsequently, to metallic [YLS13; Cao+14; DLS20] USGs. Besides, molecular dynamics [LEP13] and Ising modelling [LH10] numerically mimicked the underlying physics of this particular preparation technique. The experimental realisations all share alike preparation parameters of a high substrate temperature being in the range of 0.7 to 0.9 T_g and a low deposition rate ranging from 10 nm s^{-1} to 20 nm s^{-1} [Swa+07; Kea+07; Kea+08] to orders of 1 nm s^{-1} to 0.1 nm s^{-1} [Kea+08; Fak+11; YLS13; Rie+19; DLS20]. Experimental [FF08; BY13; Cao+15; Nga+17] and computational [SP11; Ber+17] studies of glasses' surface and bulk mobility suggest that the essential underlying mechanism which leads to ultrastability is an enhanced surface mobility during the preparation process. In that way, vapour deposited glasses seem to directly access a low energy state in the potential energy landscape by their preparation [PS13; Edi17; Rod+22].

From the discovery of USGs, it was commonly accepted that it takes centuries to thousands of years of annealing or aging a conventionally produced glass to reach similar stability [SEP13; Ber+17]. Moreover, recent studies on bulk metallic glasses (MGs) show that only several decades of aging time for a Ce-based MG suffices to reach comparable stability as in metallic USGs [Zha+22].

Different techniques have been developed to study the underlying dynamics; for instance dielectric spectroscopy [Lun+00; Ric17], mechanical spectroscopy [HS16; RS17], surface sensitive techniques such as atomic force microscopy (AFM) or nano-indentation [Wag+11; DM16], calorimetry [Zhe+19], and X-ray diffraction [DWB21]. Although these techniques cover a large spectrum of time and spatial scales, there is still a blind spot which a recently developing technique perfectly fills. Because X-ray photon correlation spectroscopy (XPCS) is capable of accessing spatial scales on the nanometre scale, together with an observable time scale spanning from 10^{-3} s to 10^{5} s it is designated to be the perfect tool to fill that gap [GMR08; MFR15]. Hence, XPCS enables new perspectives to study *local* rearrangements during slow

relaxation processes in MGs. After the first publication on the atomic-scale relaxation dynamics in MGs [Rut+12], the method could show its valuable contribution to the metallic glass community by revealing a particular *anti-aging* effect in ultrastable metallic glasses (UMGs) [Lüt+18] as presented in this thesis, and uncovering intermittent dynamics and indications of a dynamical crossover [Eve+15; Gal+18; Hec+18]. Young, complementary techniques to study the dynamics of medium-range order such as fluctuation electron microscopy (FEM) or electron correlation microscopy (ECM) have been published and demonstrate their impact [VGT00; TV18].

To understand how relaxation processes of local rearrangements relate to cooperative effects such as the formation of shear bands [SWS07], XPCS data may provide insight thanks to its temporal resolution along with the evolution of relaxation processes. Statistical imprints of avalanche dynamics can reveal the activation of cooperatively rearranging regions [LC09]. It have been found in MGs by means of mechanical spectroscopy [Kri+14]. The connection between statistical measures, i.e. the statistics of avalanches, in the evolution of the dynamics and cooperatively rearranging regions throughout shear transformation zones (STZs) is addressed within the here presented work.

In contrast to all aforementioned techniques, machine learning has recently been used to predict dynamical features and plastic deformations solely based on the initial particle positions [Bap+20]. It will be of great interest to follow the development of such techniques in the near future.

The central theme of this thesis is as follows. After the introductory chapter, chapter 2 introduces metallic glasses, in particular the framework of the potential energy landscape, and gives a brief introduction to relaxations and aging. While the preparation of ultrastable metallic glasses is explained, the compositions and fundamental characterisations of the herein discussed samples, in particular of ultrastable metallic glasses, are lined out in this chapter. Chapter 3 puts its focus on X-ray photon correlation spectroscopy (XPCS) with an introduction to coherent synchrotron radiation, and on an overview of X-ray scattering. It culminates in a phenomenological view on a coherent scattering phenomenon – speckles – and their capabilities in order to detect

density changes on the atomic length scale. How XPCS is realised at a beamline and how therewith captured data are commonly processed is provided, and the perspectives of XPCS experiments at future X-ray light sources are debated. Results according to publication [Lüt+18] on anti-aging in ultrastable metallic glasses are reported and discussed in chapter 4. Besides, aging phenomena of annealed UMGs are addressed. Eventually, new data processing tools for XPCS data are presented in chapter 5. These tools statistically analyse quantified changes of the relaxation time evolution of MGs, unlocking power-law distributed amplitudes of the mentioned changes, and are discussed in the scheme of avalanche dynamics. Finally, a general discussion of all aforementioned chapters is hold in chapter 6.

Chapter 2

Metallic glasses

Contents

2.1 Introduction

MGs are neither necessarily transparent nor usually colourless[1]. They are called *metallic* because of their composition and electrical resistivity. They are called *glass* due to their structural properties and thermodynamic behaviour as will be stated in the this chapter. All MGs have in common that at least one of their constituents is a chemical element belonging to the group of metals.

MGs span a wide variety of materials. There are tens of different material compositions and over hundreds of configurations forming MGs [Gre95; Wan12]. All of them have in common that typical behaviour of glass forming materials, showing a continuous variation of some physical properties', a slope upon temperature change, such as volume V, enthalpy H or configurational entropy S_c. That change of slope manifests in a region around $^2/_3$ of the melting temperature [Ang+00].

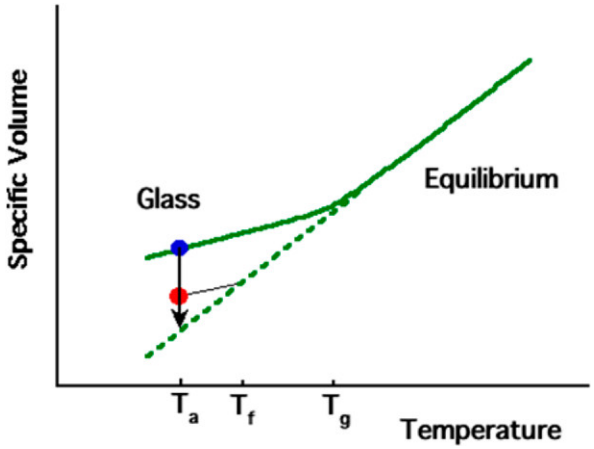

Figure 2.1: Schematic representation of the specific volume – temperature – dependency of a glass building material. The dashed line represents the extrapolation of the equilibrium line while T_g stands for the glass transition temperature, T_f the fictive temperature and T_a stands for a temperature at which the material is kept and aging progresses. Reprinted with permission from [MS17]. Copyright 2024 American Chemical Society.

Upon cooling, at temperatures lower than that region, a material that de-

[1] Both optical properties refer to the visible spectrum of a human eye.

viates from the former slope of the equilibrium line forms a glass. That is why this region of changing slope defines the glass transition temperature (T_g) (see fig. 2.1). T_g depends on the material and on the temperature rate $\dot{T}$ as well[2]. At higher cooling rates T_g sets on earlier while lower cooling rates lead to lower T_g [Guo+11]. However, the cooling rate needs to be sufficiently high in order to prevent crystallisation. Glass formers of a more complex composition generally urge less high cooling rates [Gre95]. Substantially different covalent radii of the compounding elements, e.g. involving beryllium (Be), contribute to a lesser need of a high temperature rate while cooling [Gre95].

All those different paths forming a glass lead to different manifestations of glasses the same composition. Another procedure which results in different glasses happens spontaneously. By simply leaving a glass to itself, the physical properties of the glass change. This process is sketched in figure 2.1 on the pathway from the blue (upper) to the red (lower) dot and below when the glass transits from one glassy state into a different one. All that even happens at constant temperature – here called annealing temperature T_a. The process just described is called *aging* and is depicted throughout a lowering of the volume in the named figure. Besides, aging affects numerous mechanical properties [Cui+21] and is a crucial scientific mystery to understand as it affects the usability of MGs in diverse applications.

Each glassy state can be attributed an intersection of a parallel path to the former (initial) glassy states path and the equilibrium line, defining the fictive temperature T_f. This fictive temperature represents the theoretical glass transition temperature which that glassy state belongs to as if the glass was produced directly into that state [Bad+07]. As the aging process itself decelerates, glasses aged throughout annealing become kinetically more stable over time. However, this aging process can take very long time [Kov64; SEP13; MZ15], leading to unpractical demands in order to form (more) stable glasses. This is why different paths to form stable glasses are sought for.

[2]The dot on top of the variable T denotes the "dot notation" or NEWTON's notation denoting the time derivative of a variable x, hence $\frac{\mathrm{d}}{\mathrm{d}t}x$.

To predict or even guide the aging process and with that the transit of physical and chemical properties of a glass is the main impetus of this thesis. The findings will contribute to the general understanding of the aging process which is of particular interest in material science.

2.2 Properties

2.2.1 Structure

As amorphous materials are disordered systems, they are often suggested with a chaotic or random structure. In fact, by definition the atomic structure of amorphous metals exhibits no long-range order.

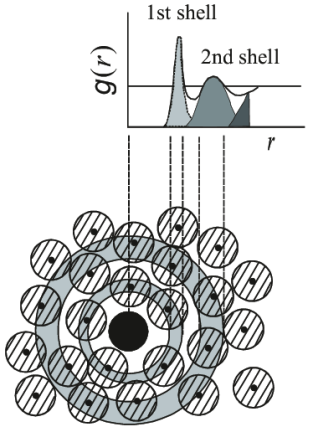

Figure 2.2: Schematic 2-dimensional projection of a radial distribution function. Taken and adopted from [Was+08].

However, the absence of long-range order in a glass can still be structurally described. Such a structure can be pictured starting from a single reference particle which is surrounded by other particles which are distributed in unalike distance to each other. When then the radial occurrence of a particle in three dimensions, i.e. its density distribution, is integrated azimuthally and resolved radially, the so called radial distribution function (RDF) $g(r)$ is calculated. $g(r)$ can be understood as the distribution of coordination shells of surrounding particles with respect to a reference particle at $r = 0$ – in other words, it tells the probability of finding a particle at radius r from a reference particle. Especially, the first coordination shells develop well pronounced features in the RDF while for large r the function $g(r)$ converges towards a constant value, the average density of the material. The described arrangement of particles is illustrated schematically in figure 2.2. The inset in the upper right depicts the $g(r)$ function with the first three underlying shells.

The mathematical description of the arrangement of particles within disordered systems is of particular importance as it is experimentally accessible. By means of X-ray diffraction (XRD), the equivalent of the $g(r)$ function in reciprocal space – the so called static structure factor $S(q)$ – can be assessed. The static structure factor is related to $g(r)$ throughout FOURIER transformation as follows [DWB21]:

$$S(q) = 1 + 4\pi\rho \int_0^\infty \mathrm{d}r \; r^2 \frac{\sin qr}{qr} \left(g(r) - 1\right) \quad . \tag{2.1}$$

Therein ρ denotes the particle number density, q denotes the momentum transfer (for details see sec. 3.3) and r denotes the radius with respect to a reference particle at $r = 0$. For simplicity reasons a two-dimensional picture is drawn here with q and r being treated as scalar quantities; however, the mathematical description can be easily expanded to three dimensions. The first peak in diffraction data of disordered systems corresponds to the first coordination shell in real space, which denotes its particular importance. It is also called the first sharp diffraction peak (FSDP) and particularly characterises the *local* structure as it represents next neighbour coordination [Ell91; EB03; Cav09; DWB21]. Characterisations of $S(q)$ represented by measurements of XRD are depicted in section 2.5.2.

2.2.2 The potential energy landscape

The concept of the potential energy landscape (PEL) is substantial for understanding relaxation processes in disordered systems. Initially introduced to the field of glasses by Goldstein [Gol69] and brought up or extended by others [SW84; LS87; Ang95; Sti95; DS01; Sci05; Heu08; RAA15], the concept remains essential to describe the structural configuration in terms of a multi-dimensional topographic energy map composed of energy barriers, basins and wells.

Figure 2.3 shows a schematic representation of the PEL (left panel). It illustrates the multi-dimensional potential energy function $\Phi(\boldsymbol{r}_1, \boldsymbol{r}_2, \ldots, \boldsymbol{r}_N)$ as a function of coordination space $\boldsymbol{R} \equiv (\boldsymbol{r}_1, \boldsymbol{r}_2, \ldots, \boldsymbol{r}_N)$. All coordinates $\boldsymbol{r}_i \in \boldsymbol{R}$ comprise position, orientation and vibration coordinates of each particle in

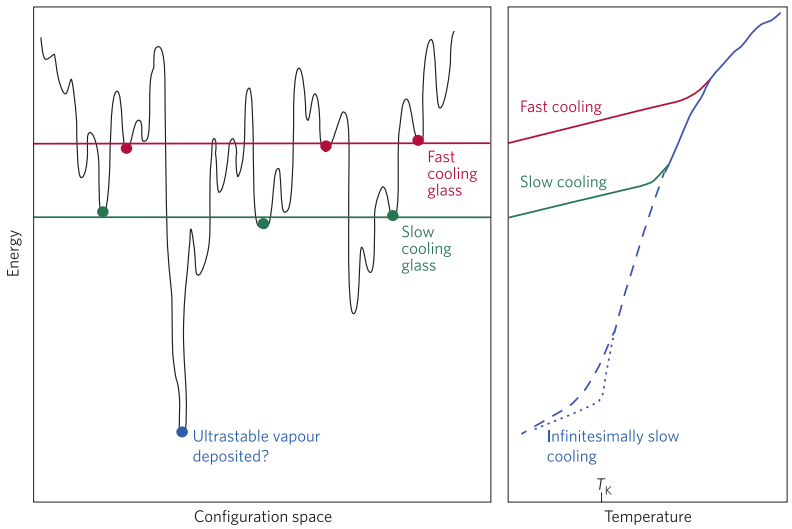

Figure 2.3: Schematic one-dimensional projection of the potential energy landscape (left) and temperature dependent (right) energy of a glass, published by Parisi et al. [PS13]. Reproduced with permission from Springer Nature. The crystalline configuration is not displayed.

an N particle system and are referred to when in the following the term *state* is used. The PEL consists of various local minima with relatively small or large local maxima[3] in between. Each local minimum reflects the configuration $\boldsymbol{r}_i$ of a metastable arrangement. These states are called *inherent states*. The *barriers* around those minima separate inherent states while two contiguous local maxima span a *basin* in between. Moreover, a region of multiple similar, contiguous local minima, which are enclosed by relatively large barriers is called a *metabasin*. Within such a metabasin, structural transitions are rather associated with β relaxations related to gradual rearrangements of the local arrangement, while transitions from one metabasin

[3] In this thesis, the term *(local) maximum* (or to be more general *local extremum*) differs from the term *saddle point*. A maximum of a function $f(x)$ at x_0 is defined throughout two conditions which both need to be fulfilled. (1) The first derivative $\frac{\mathrm{d}f(x)}{\mathrm{d}x}|_{x=x_0}$ needs to vanish. (2) The second derivative $\frac{\mathrm{d}^2f(x)}{\mathrm{d}x^2}|_{x=x_0}$ must not vanish. In contrast, a saddle point is defined by its first derivative vanishing while the second derivative must vanish as well at x_0. For simplicity reasons, this definition is made in two dimensions, yet can be easily extended to multiple dimensions. As an example, the two dimensional function $f(x) = -x^2$ has a maximum pronounced at $x_0 = 0$; this is not seen as a saddle point. In contrast the function $f(x) = x^3$ holds a saddle point at $x_0 = 0$. Other authors may use a different definition of the term saddle point.

to another are rather associated with α relaxations [Heu08; Sti95]. In a simple system consisting of structureless single particles, minima of identical hight are achievable through permutation of identical particles. It is important to stress that the potential energy function $\Phi(\boldsymbol{R})$ itself is not a function of temperature. Yet, transitions and relaxation processes are highly temperature dependent.

Having an essential impact on the potential energy landscape of the glass, the preparation process itself predefines the thermodynamic metastable state of the glass in which it will find itself after falling out of equilibrium. In other words, the preparation process dictates in which position of the PEL an MG is initially located. The cooling rate (upon fast quenching methods; introduced in sec. 2.3) plays a crucial role: at a relatively high cooling rate, the viscosity increases rapidly on the path from liquid to supercooled liquid, and especially when the system falls out of equilibrium at the end of the supercooled liquid phase. This process is accompanied by a continuous reduction of particle mobility. Lower cooling rates, however, consequently allow the particles to stay in equilibrium following the equilibrium line until lower temperatures (see fig 2.3, right panel). Considering that the glassy state deviates from the equilibrium line at lower temperature, slower cooling intrinsically enables the glass to reach a configuration associated with a lower $\Phi(\boldsymbol{R})$. Yet, the cooling rate has a lower limit as to omit crystallisation which can effectively be prevented by sufficiently fast cooling. Lower regions in the PEL are associated with states of higher stability or higher (longer) relaxation times, respectively. If it was possible to cool a liquid infinitesimally slow – while preventing crystallisation – the lowest minima and hence highest stability could be reached. This configuration might be called an *ideal glass*. However, infinitesimally slow cooling is not possible because of two reasons. First, practical reasons do not allow to cool infinitesimally slow as that would take more time than available on human time scales, relaxation times increase reciprocally with temperature according to the Vogel-Fulcher-Tamman (VFT) relation [Ruo+04]. In the Krausser-Samwer-Zaccone (KSZ) model, this is explicitly described by two exponential dependencies from the local structure parameter λ [KSZ15]. Second, especially metallic glasses tend to crystallise upon slow cooling. From that a lower limit cool-

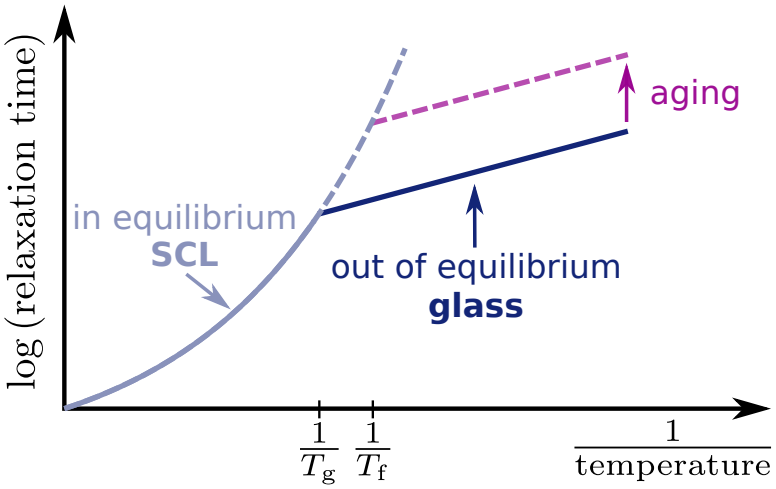

Figure 2.4: Schematic representation (own work) of an Arrhenius plot of the relaxation time and temperature of amorphous materials. At higher temperatures the system is *in equilibrium* while upon cooling, around the glass transition temperature, it falls *out of equilibrium*. With time the systems relaxes further towards equilibrium, this aging process is indicated by the arrow.

ing rate emerges and a practically explorable temperature range for cooling metallic liquids can be conducted.

Throughout a different technique named vapour deposition, which will be shed more light on in section 2.3.2, the limitations described above seem to be possible to overcome. The relaxation behaviour of samples fabricated by vapour deposition is addressed and discussed in the framework of the PEL in section 4.9.

2.2.3 Relaxations and aging

MGs undergo several kinds of relaxations [Max67; Ang+00]. The focus of this section lies on structural relaxation, also called α or primary relaxation [Lun+00], which is the most prominent relaxation within the studies of this thesis. Relaxations such as the secondary or β relaxation as well as the Boson peak, which are promoted at higher frequencies, are not subjected within this section. At temperatures below the glass transition T_g, amorphous

systems fall out of their equilibrium (liquid or supercooled liquid) state. As a consequence, the system is able to occupy numerous metastable states governed through irreversible processes which strongly depend on the history of the system, in especially on applied experimental protocols. With that, based on the ongoing relaxation processes, physical properties of the system evolve with time towards the corresponding equilibrium state. This behaviour is called *physical aging* (in the following simply "aging") and is indicated by the up-pointing arrow in figure 2.4 [Kov64; Str77; Hod95; McK12; SEP13; MZ15; RPE17; Rie+22].

The foundation of the underlying structural relaxations manifests through atomic motions, which can be described conveniently through density fluctuations. For their mathematical description the intermediate scattering function (ISF) holds, which writes in its normalised form [GMR08]

$$F(q,t) = \frac{\left\langle \rho_q^*(q,0), \rho_q(q,t) \right\rangle}{\left\langle \rho_q^*(q,0), \rho_q(q,0) \right\rangle} \quad , \tag{2.2}$$

where ρ_q denotes the k-space equivalent of the particle density operator $\rho(\boldsymbol{r},t) = \sum_j \delta\left\{\boldsymbol{r} - \boldsymbol{R}_j(t)\right\}$ after the formalism by van Hove [Van54]. Chevrons (angle brackets) $\langle\cdots\rangle$ denote the average of the expectation value of the enclosed term. The denominator of the ISF is equivalent to the static structure factor $S(q) = \left\langle \rho_q^*(q,0), \rho_q(q,0) \right\rangle$. For simplicity reasons and because of the isotropic character of MGs, the vector form in equation 2.2 is omitted, i.e. $q = |\boldsymbol{q}|$. These density fluctuations can be experimentally captured and analysed. The experimental implementation is elucidated in chapter 3, while the experimental implementation is applied in the following chapters chapters 4 and 5.

The described aging process with its indications on physical properties of the glass is a huge drawback regarding practical applications of glasses. In especially the drive to explore lower states in the PEL connected to rearrangement processes, and hence aging, limits application-oriented feasibilities where stability of physical properties are fundamental. This flaw seems possible to be overcome by a new preparation technique. The new approach demonstrates

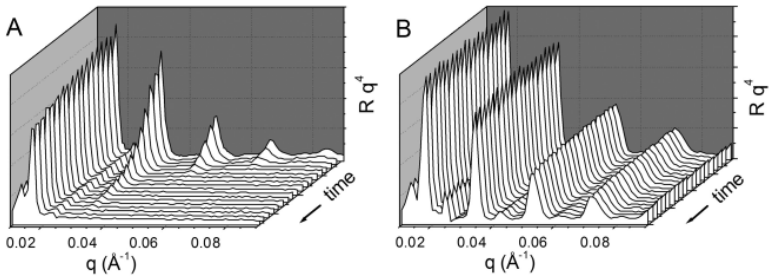

Figure 2.5: Neutron reflectivity data for USG continuously annealed closely below T_g over a time span of 16 h. (A) Conventionally fabricated organic glass showing a prompt decay of the multilayer structure peaks along with the continuous measurement. (B) Ultrastable organic glass showing no decay of the structure peaks at all. Adopted from [Swa+07], reprinted with permission from AAAS.

the ability to cut short the hike down the PEL [Swa+07; Kea+08; YLS13] which would take longer than human time scales [SEP13; Wel+13; RAA15] by conventional means such as annealing. By means of vapour deposition (details are given in sec. 2.3.2), so called USGs with exceptional thermodynamic and kinetic stability can be produced directly by their fabrication process. The process allows the particles to explore the PEL directly by preparation and hence occupy a deeply relaxed state deep down in the energy landscape. Parisi et al. [PS13] relate such a glass to a deepest possible not crystalline state in their schematic sketch of the PEL in figure 2.3.

Swallen et al. [Swa+07] could demonstrate the production of such a USG and therewith its exceptional thermodynamic and kinetic stability. Figure 2.5 shows neutron reflectivity data versus wave vector q of an organic glass multilayer along with 16 hours of continuous annealing closely below T_g by Swallen et al. [Swa+07]. While the left graph (A) shows a complete decay of the multilayer-structure peaks over time already after the first few measurements, the structure peaks on the right side graph (B), in contrast, remain stable over 16 hours, not even showing an indication of peak intensity reduction, hence inter-layer diffusion. Similarly, Yu et al. [YLS13] fabricated the first ultrastable metallic glass throughout vapour deposition technique.

2.3 Preparation

MGs can be prepared throughout different approaches. One may either start with a ordered (crystalline) system and destroy the long range order or – and this is the approach used in this thesis – one starts with a disordered system like a liquid or a gas. Within the here presented studies two methods to prepare metallic glasses are used, fast quenching of a melt as well as a vapour deposition technique.

2.3.1 Fast quenched metallic glasses

Fast quenching (FQ; also known as melt quenching) is a commonly used method to create metallic glasses [Gre95; Ell90, Chpt. 1.3]. For this purpose a melt is cooled sufficiently fast to prevent crystallisation of the composition. For metallic glass formers this has to happen very fast – the melts need to be *quenched*. Several techniques have been developed in order to perform such a rapid cooling, and almost all of them involve a large heat sink to dissipate the heat. A "chill-block" made of copper is usually used to realise that heat sink. One realisation of such a fast quench method is called *melt spinning*. It is used to prepare the herein presented fast quenched (FQ) MGs samples. Figure 2.6 shows a photograph of such a ribbon exemplary. In this procedure the liquid melt of the alloy is spilled through a small nozzle onto a polished rotating copper wheel. This wheel takes the thermal energy of the melt and hence quenches it to form the amorphous solid. Parameters such as the rotation frequency of the Cu, the finish of its surface, the diameter and throughput of the melt jet and the ambient gas pressure influence the effective cooling rate. Typically, cooling rates of $10^6\,\mathrm{K\,s^{-1}}$ to $10^8\,\mathrm{K\,s^{-1}}$ are achieved by this procedure [Ell90; Gre95].

Figure 2.6: Photograph (own work) of a melt spun MG ribbon of $Zr_{65}Cu_{27.5}Al_{7.5}$.

In the following, the term fast quenched (FQ) refers to melt spun ribbons and is commonly used for producing *conventional* MG systems, to which vapour deposited (VD) samples (see next section 2.3.2) get compared to. In chapters chapter 4 FQ samples prepared by melt spinning are discussed.

2.3.2 Vapour deposited metallic glasses

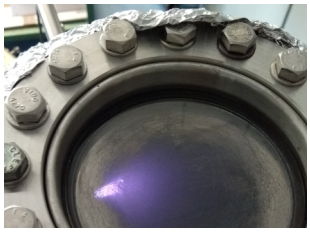

Figure 2.7: Photograph (own work) of purple glowing plasma of the DC magnetron sputtering, observed through a window in the vacuum chamber.

A second method to produce metallic glasses is physical vapour deposition (PVD). This method makes use of physical deposition of particles onto a substrate to grow a MG layer by layer without provoking a chemical reaction. That is why it is called *physical* vapour deposition. In contrast to physical VD, another deposition method called chemical vapour deposition is neither described nor referred to in this thesis. Consequently, physical vapour deposition will be simply called vapour deposited (VD) from here on. In this work, vapour deposited (VD) is realised through *DC magnetron sputtering*. In brief, DC magnetron sputtering makes use of a low-pressure plasma's ions, which bombard a (polycrystalline) target. This target is made of the same composition of which the metallic glass should be composed of. Hot ions[4] from the plasma erode the target and deposit atoms onto the substrate, gradually growing a film. In the vacuum chamber used within the herein presented work, the substrate itself can be either cooled with water or a cryogenic fluid, and heated by a halogen lamps filament. The home made substrate holder is equipped with two temperature sensors and a proportional-integral-derivative (PID) controller regulating the substrates temperature. With this setup, it is possible to control T_{sub} in a range of at least 100 K to 600 K.

Two rectangular slices of polished NaCl crystals with surface dimensions of 20 mm × 30 mm are used as substrates, to potentially being dissolved in wa-

[4] With an energy in the order of a few ten keV.

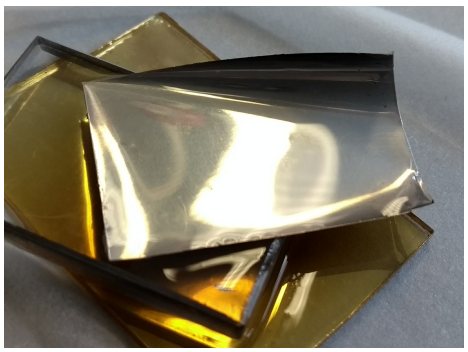

(a) With isopropyl alcohol wetted film on top of NaCl crystal on a coloured silicate lass plate.

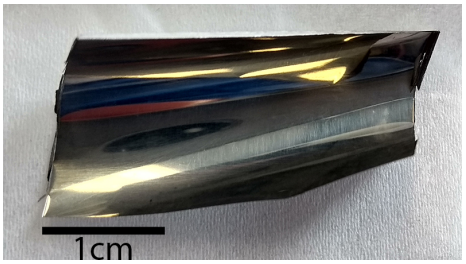

(b) Free standing film

Figure 2.8: Photographs (own work) of vapour deposited $Pd_{77.5}Cu_6Si_{16.5}$ MG immediately after preparation.

ter if the deposited films did not separate easily. Eventually they separate easily after deposition by gently scraping along the edges of the film or – even more simple – pouring isopropyl alcohol on the film as indicated in figure 2.8a. From each sputtering process two films of VD MG are produced.

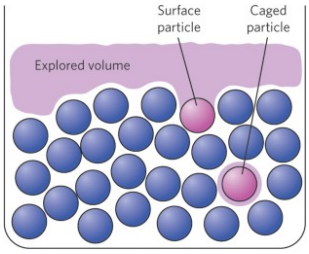

Figure 2.9: Schematic drawing of enhanced mobility of a surface particle exploring the layers proximal to the free surface during vapour deposition. Reproduced with permission from Springer Nature [PS13].

Producing ultrastable metallic glasses In order to produce amorphous MG films throughout vapour deposition, DC magnetron sputtering process parameters are used as listed in table 2.1. Amorphous targets of $Cu_{50}Zr_{50}$ and $Pd_{77.5}Cu_6Si_{16.5}$ were used. To make an *ultrastable* MG, sputter rate and substrate temperature are crucial parameters during preparation. Low sputter rate in conjunction with high T_{sub} (in the range of $T_{sub} = 0.8 - 0.9\,T_g$) are parameters to successfully produce UMGs as previously shown by [YLS13; DLS20], and reproduced in the herewith presented work (see fig. 4.1), published in [Lüt+18].

parameter	quantity
sputter gas	Argon
Ar pressue	6×10^{-4} mbar
sputter rate	$1.76(1)\,\mathrm{nm\,s^{-1}}$
substrate temperature (T_{sub})	variable; ca. 100 K to 600 K
film thickness	5 µm

Table 2.1: Sputtering parameters used for producing amorphous MG films.

The conjunction of a low sputter rate together with a T_{sub} closely below T_{g} allows an enhanced surface mobility of the top layer particles of the sputtered film. The alliance of both parameters allows impacting particles to explore the surface of the sputtered film and hence the PEL in order to reduce the potential energy $\Phi(\boldsymbol{R})$, bypassing long time aging processes which are usually necessary to reach those low energy states in the PEL. Conventional relaxation processes would require nearly impossible time spans of aging to reach such a state. An elevated substrate temperature facilitates this process as the thermal energy provides enhanced surface mobility of the top layer atoms [Swa+07; PS13; YLS13; MMS16; Ber+17; Yan+21].

Figure 2.9 schematically depicts the enhanced surface mobility of a deposited particle and the picture of an explorable volume of a surface particle in comparison to a caged particle which is already built in. A T_{sub} far below T_{g} decreases also the surface mobility, and with that the ability of the just arriving sputtered particles to explore the topology for the site with lowest potential energy before the next sputtered particles arrive at the surface, which would effectively suppress the creation of a UMG (see further details in sec. 4.2 and fig. 4.1).

2.4 Characterisation techniques

MGs show several properties and behaviour which are particularly characteristic for them. To check and monitor them, there are several techniques available. A selection of the most common ones, which are considered within

this work and have been applied to the studied samples, are briefly illustrated within this section. For more detailed explanations, several textbooks or review articles exist and should be considered for consultation in case of profounder interest [Ell90; Zhe+19].

2.4.1 Calorimetric analysis by differential scanning calorimetry

Differential scanning calorimetry (DSC) is a common technique to study heat dissipation in MGs. The instrument used at University of Göttingen is a *DSC 7* manufactured by Perkin Elmer. To perform DSC two identical crucibles made of aluminium, gold or other materials simultaneously follow a defined temperature protocol, heated by two independent furnaces. Only one crucible is equipped with the material which is about to be analysed while the second crucible remains empty. Afterwards, both furnaces follow the same temperature protocol which dictate temperature range and rate. While following the temperature protocol, the heat Q necessary to follow the protocol is measured for each furnace. Assuming that the crucibles are identical, the difference of both captured heat flows gives the heat flow contribution of the sample itself to follow the temperature protocol. In order to prevent the influence of oxidation processes and to improve thermal coupling between crucible and furnace, a low, constant flow of the noble gas argon (order of $10\,\mathrm{mL\,min^{-1}}$) is maintained. Exothermic sample behaviour results in a lower, while endothermic behaviour results in a higher heat flow difference. The results are usually depicted in a $c_p - T$ diagram.

Before starting an analysis procedure, the DSC instrument is calibrated by scans of zinc and indium standards. The onset of melting temperature of both materials is determined, and for indium the melting enthalpy is evaluated. A comparison to literature data allows to calibrate temperature and heat flow. Usually, scans are performed in a range of 310 K to 820 K using a temperature rate of $0.1\overline{6}\,\mathrm{K\,s^{-1}}$ ($\widehat{=}\,10\,\mathrm{K\,min^{-1}}$); the melting temperature of the crucible must not be attained. The amount of sample examined is in the order of 20 mg, however, if necessary, samples of around 1 mg may give reasonable results.

In order to obtain the contribution of the amorphous state to the specific heat only, a samples heat flow is measured twice following the same temperature protocol which exceeds the crystallisation temperature. The data from the second run is subtracted from the first. As the specific heat of the glassy and of the crystalline state is close to each other, their difference is close to zero in the glassy region. At higher temperatures, a well pronounced positive deviation from zero forms starting from T_g until the latent heat switches the signal to negative when approaching T_x. The onset of T_g is determined by the *(double-)tangent method* [Per94; Zhe+19].

2.4.2 Static structure analysis using X-ray diffraction

Static structure X-ray analyses are performed to confirm the amorphous structure of the produced MGs as well as to monitor their amorphous state after treating them, for instance by annealing, aging or applying tensile stress. This is done throughout *wide angle* X-ray scattering also called wide angle X-ray diffraction (XRD). This section only covers a brief outline to the physics behind it. For a more detailed insight section 3.3 may be consulted to gain a general insight into the fundamentals of scattering.

XRD is performed regularly in order to confirm the desired structure of the produced or treated samples. It is commonly performed at a laboratory at University of Göttingen using a Bruker *D8 Advance* diffractometer. This diffractometer uses a Cu-K_α source operating at a wavelength $\lambda = 0.154\,06\,\text{nm}$. Another diffractometer which was used within the work of this thesis is a *Diffraktometer D5000* by Siemens using a Mo X-ray source which operates at a wavelength $\lambda = 0.070\,93\,\text{nm}$.

2.4.3 Compositional analysis by energy-dispersive X-ray spectroscopy

To analyse the composition of the studied samples, energy-dispersive X-ray spectroscopy (EDX) analysis is carried out, using a scanning electron microscope (SEM) *LEO SUPRA 35* by Carl Zeiss NTS GmbH equipped with an EDX instrument by Thermo Fisher Scientific GmbH.

sample name	nominal composition ($\%_{atom}$)	preparation technique
`Cu50Zr50-VD_014`	$Cu_{50}Zr_{50}$	vapour deposition
`Cu50Zr50-VD_015`	$Cu_{50}Zr_{50}$	vapour deposition
`Cu50Zr50-FQ_001`	$Cu_{50}Zr_{50}$	fast quenching
`PdCuSi-VD_003`	$Pd_{77.5}Cu_6Si_{16.5}$	vapour deposition
`PdCuSi-VD_004`	$Pd_{77.5}Cu_6Si_{16.5}$	vapour deposition
`PdCuSi-VD_005`	$Pd_{77.5}Cu_6Si_{16.5}$	vapour deposition
`PdCuSi-VD_006`	$Pd_{77.5}Cu_6Si_{16.5}$	vapour deposition

Table 2.2: Overview of the parental samples discussed within this thesis. `Cu50Zr50-FQ_001` was given by Eloi Pineda (Dpt. de Física, ESAB, UPC BarcelonaTech, Spain).

In order to perform an EDX analysis a high energy electron beam is emitted from an electron gun within a SEM. Those high energy electrons are capable of exciting electrons from an inner shell and creating free electrons. Thus, a series of electron relaxation processes is likely to happen, where subsequently electrons drop from an outer shell towards the vacancy of an inner one. In case a high-energy transition, each of these drops result in emission of characteristic electromagnetic radiation in form of X-rays. The characteristic emission can be unambiguously attributed to a specific element and thus identify the chemical constitution of the examined area. Moreover, the relative intensities of each element's characteristic emission carry information on the compositional ratio of the elements in $\%_{atom}$ (atomic percent) [Ins83].

2.5 Sample characterisation

Table 2.2 shows all samples which are used within the work of this thesis. From each sample, pieces are used for the referred studies. Each piece can by identified with its unique identifier. The identifier starts with the nominal composition (with or without elemental quantities), followed by a hyphen, a tag for the preparation process (`FQ`/`VD`), an underscore, and a sequential number. If the sample was not produced by myself, the initials of this person precede that sequential number. Whenever a piece is separated from a sample, a letter (`a-z`) or a numeral (`00-99`) is appended to the parental piece

(e.g. `Cu50Zr50-FQ_001f` or `Cu50Zr50-VD_015a11`) in an alternating manner.

2.5.1 Calorimetric characterisation

DSC measurements have been performed at Göttingen University at the *DSC 7* instrument (Perkin-Elmer) in order to achieve calorimetric characterisations of FQ as well as VD metallic glasses. In order to prepare ribbon (FQ) samples for analysis, their edges are straightened in case they are spiky – hence, spikes get cut off. Afterwards, samples are cut into small pieces and stapled to 15 to 20 layers into the provided 30 µL vented Al crucible[5]. VD samples are cut into small squares and stacked as well. This allows to pile up to approximately 13 mg of material into the crucible. As FQ samples are intrinsically thicker, they stack up to approximately 32 mg. A constant flow of approximately 10 mL min^{-1} of 99.999 % pure Ar gas equipped with an oxygen filter ("Alphagaz – purifier O_2-free", Airliquide) flushes the sample chamber to prevent oxidation.

Before a sample's calorimetric behaviour is measured, it is cleaned first with acetone and second isopropyl alcohol in an ultrasound bath for approximately 5 min each. Then one sample is cut and stapled into a crucible as described above and loaded into the DSC instrument. An individual, unused Al crucible is used as reference and loaded into the reference furnace.

Figure 2.10 shows the results of the data obtained by DSC measurements of CuZr-based FQ (orange-like colours) and VD (blue colour) samples. The data show subtracted differential heat flow, normalised by the samples mass, and rescaled by a linear function $f_{\mathrm{corr}}(T)$ to correct from drift. The function $f_{\mathrm{corr}}(T)$ is used such that the DSC signal from the first and second run match in the crystalline region. A linear signal drift is assumed. The detailed temperature protocol of the DSC measurement is given in appendix B. The UMG sample `VD_015b` shows a smooth signal with an onset temperature $T_{\mathrm{on}} = 671\,\mathrm{K}$. The three FQ samples `FQ_001a`, `FQ_001b` and `FQ_001f`

[5] `VD_015` was measured in not-vented Al crucible.

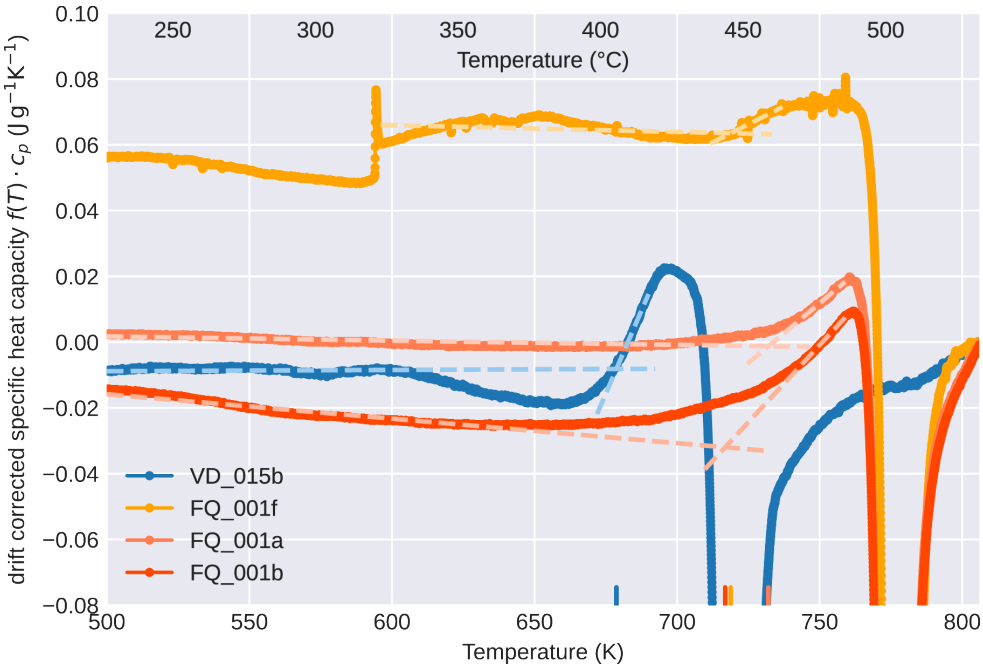

Figure 2.10: DSC data (coloured bullets) of the drift corrected specific heat capacity $f(T) \cdot c_p$ of CuZr-based VD and FQ samples at a heating rate of $10\,\mathrm{K\,min^{-1}}$. The data are corrected by a linear function $f_{\mathrm{corr}}(T)$ in order to handle a signal drift. Dashed lines of lighter colour (matching with the corresponding DSC data) signal linear fit functions to baseline and ascending regimes, respectively. Their intersection defines T_{g} by the tangent method. The determined values of T_{g} are indicated by coloured vertical short lines on the abscissae.

show differing results. The signals of `FQ_001a` and `FQ_001b` evolve with a similar shape, although the latter displays a slightly falling curve below the onset temperature, what results in the determination of the $T_{\mathrm{on}} = 717\,\mathrm{K}$ at a lower value (`FQ_001a` quantifies $T_{\mathrm{on}} = 732\,\mathrm{K}$). A third sample of the same batch, `FQ_001f`, shows a similar $T_{\mathrm{on}} = 719\,\mathrm{K}$ as `FQ_001b`, although its signal is highly unsmooth. It seems that the thermal contact of this sample within the crucible was insufficient, which would also explain the spike in the data at approximately 595 K. However, the results of all FQ samples support each other, while in especially their exothermic peak due to crystallisation lie on top of each over. Later determinations of the chemical composition of these samples will show, that UMG and FQ samples do not have the same composition as initially expected, and may explain the large difference in the

calorimetric analysis of the two.

2.5.2 Static structure characterisation

Figure 2.11 depicts wide angle XRD data of four $Pd_{77.5}Cu_6Si_{16.5}$ VD samples, sputtered at different substrate temperatures: `PdCuSi-VD_003a`, `PdCuSi-VD_004a`, `PdCuSi-VD_005a` and `PdCuSi-VD_006a`. It shows the intensity sequentially captured over the range from 17.5 nm^{-1} to 37.5 nm^{-1} around the FSDP. All samples reveal a single, wide peak distribution with no sharp bragg or bragg-like peak at all, confirming all samples are amorphous. No quantitative difference between the samples can be determined in the static structure analysis. The position of the samples' maximum of the FSDP notes at 28.1(1) nm^{-1}. The only difference between the depicted samples is the lowering of the absolute intensity along with lower T_{sub}, which is, however, not of great interest in this analysis. Similar XRD results are found for all other samples stated in table 2.2.

X-ray sources with higher photon energy and more sophisticated detectors allow to examine a wider range in reciprocal space. Figure 2.12 shows the static structure factor of a VD $Cu_{50}Zr_{50}$ sample (`Cu50Zr50-VD_015`) analysed at the European Synchrotron Radiation Facility (ESRF) beamline ID15 at

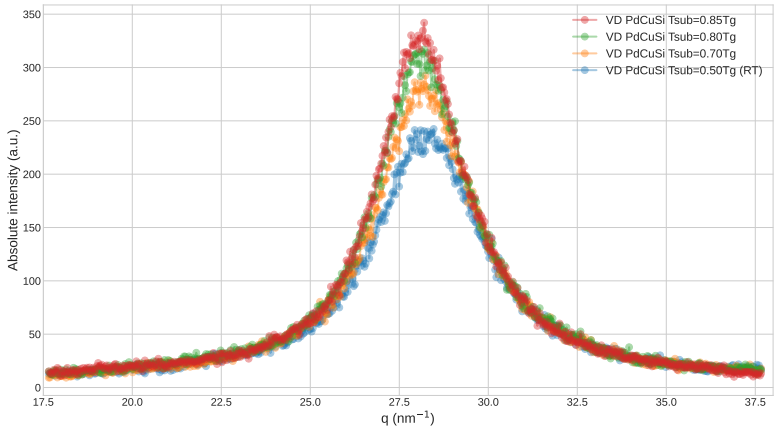

Figure 2.11: Wide angle XRD of `PdCuSi-VD` samples performed using a Cu-K_α source at 15.406 nm wavelength. The scattering vector ranges from 17.5 nm^{-1} to 37.5 nm^{-1}, including the FSDP of the static structure factor.

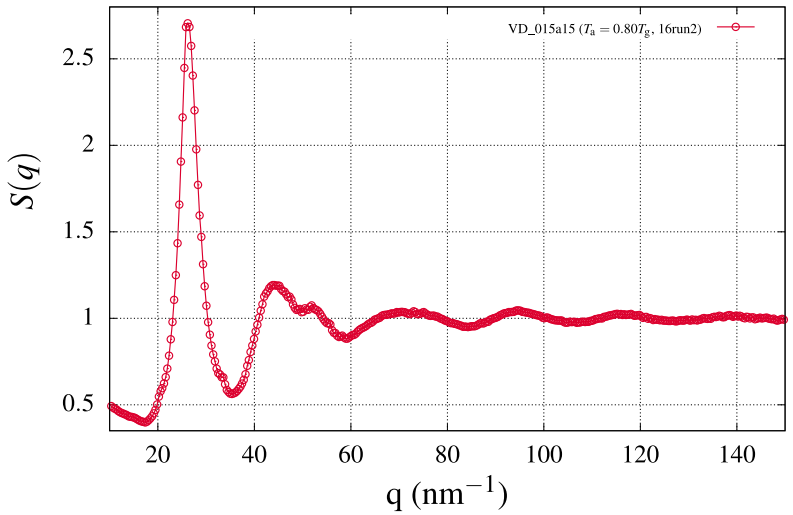

Figure 2.12: Wide angle XRD of `Cu50Zr50-VD_015` after being used in XPCS experiments, covering a wide range of the static structure factor. The measurement has been performed at ESRF beamline ID15.

a photon energy of 75 keV using a Dectris *PILATUS3 X CdTe 2M* detector.

2.5.3 Compositional characterisation

To characterise the composition of all studied samples as stated in table 2.2, EDX analyses were performed. Therefore, the samples were mounted individually on aluminium carriers, fixated to them with a carbon-based glue pad. Hence, impurities of Al or C may be expected in the captured data and are not necessarily constituents of the analysed area itself. The SEM was operated at an acceleration voltage of 20 keV. Of each sample, three to five different areas were probed, while irradiated areas, from which the emission signal is analysed throughout EDX, spanned dimensions of 20 µm × 30 µm. The determined compositions are as follows:

Sample `Cu50Zr50-VD_015` Compositional analysis detects a composition of $(55.0 : 45.0) \pm 0.2\,\%_{\text{atom}}$ (Cu : Zr). Besides, no further impurities are detected.

Sample `Cu50Zr50-FQ_001` Compositional analysis detects a composition of $(50.8 : 49.2) \pm 0.2\,\%_{\mathrm{atom}}$ (Cu : Zr). Besides, no further impurities are detected.

Sample `PdCuSi-VD_003` Compositional analysis detects a composition of $(79.1(2) : 5.8(3) : 15.0(2))\,\%_{\mathrm{atom}}$ (Pd : Cu : Si). Both sides of the sample reveal impurities which form dendrites and are identified as NaCl throughout EDX.

Sample `PdCuSi-VD_006` Compositional analysis detects a composition of $(78.7(3) : 6.2(3) : 15.3(3))\,\%_{\mathrm{atom}}$ (Pd : Cu : Si). On the vacuum-facing side during sputtering process, no further impurities are detected, while the substrate-facing side shows impurities of Na and Cl in form of round shaped erected objects.

2.6 Discussion

Static XRD measurements confirm that all prepared samples are amorphous without the existence of long range ordering as expected.

EDX measurements reveal deviations from the nominal composition which was aimed for during preparation. In particular, sample `Cu50Zr50-VD_015` shows a discrepancy of 5 percentage points to the nominal composition as well as a deviation of 4 percentage points to the FQ composition which it is compared to in following chapters. This may explain different calorimetric behaviour. Especially, absolute values of calorimetric properties such as T_{g} or T_{x} may not be well suited for comparing VD and FQ samples. In order to eliminate the influence of the differing composition, an FQ sample of the same composition as the EDX determined composition of the VD sample might be useful. $Pd_{77.5}Cu_6Si_{16.5}$ compositions show small deviations in the order of 1.5 percentage points or less from their nominal compositions. However, both sample types – FQ and VD – are found with the same composition within the uncertainties of the analyses.

EDX measurements of `PdCuSi-VD_003` and `PdCuSi-VD_006` show impurities of the chemical elements Na and Cl. These elements most likely are resid-

uals of the NaCl substrate which was used during the fabrication process. Although the samples were ultrasonically cleaned with acetone and isopropyl alcohol, NaCl is a polar substance and does only dissolve in highly polar solvents. Hence, rinsing it with water probably would have cleaned away the NaCl. However, the risk of corrosion should be considered when doing so.

Chapter 3

Structural dynamics analysis by XPCS

Contents

3.1 Introduction

Understanding the structure and dynamics of disordered systems is crucial to understand the nature of out-of-equilibrium systems. Glasses represent one branch of such systems, as it is fundamental to them to be out of equilibrium. This unlocks quite new physics to deal with when glasses, especially metallic glasses are studied. However, quantifying the structural dynamics of MGs on a atomic length scale was impossible for long time. Commonly used techniques for dynamics studies, such as dynamical light scattering (DLS)[1] can only reach up to a momentum transfer of $q \leq 4 \times 10^{-2}\,\mathrm{nm}^{-1}$ [Kwa12], while the range of $\mathcal{O}(10\,\mathrm{nm}^{-1})$ and larger is the relevant scale for dynamics of MGs as they do not exhibit long range order [Ell90]. Hence, such high momentum transfers are not accessible with visible or near-visible light sources.

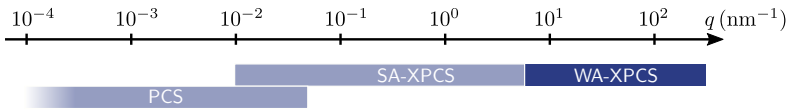

Figure 3.1: Coverage of momentum transfer by visible light and X-ray photon correlation techniques.

A young technique which is able to excess the desired q-range is called XPCS. Because of the high brilliance of 3$^{\mathrm{rd}}$ generation synchrotron facilities, PCS – for which laser light with its high degree coherence is used – could be adopted to using X-ray light sources [Sut+91; Die+95; Rut+12; Lei+12]. With that, the accessible q-range widely expands towards larger values as depicted in figure 3.1 and can roughly be split into the regimes of *small angle* and *wide angle* XPCS. At synchrotrons, accelerated electrons emit X-ray radiation in a spontaneous and independent manner. Hence, such an X-ray beam can only be considered partially coherent. The challenge in the X-ray regime is to retain high enough intensity of X-ray radiation after preparing a coherent beam. That coherent beam is critical to the performance of X-ray photon correlation spectroscopy. A quantitative description of the coherence characteristics of synchrotron radiation may be attributed to the *longitudinal* and *transversal* coherence length.

[1] Also known as photon correlation spectroscopy (PCS).

3.2 Coherence of synchrotron radiation

Synchrotron radiation, provided by electron (or positron) storage rings, is a result of a chaotic emission process. Charged, relativistic particles produce photons spontaneously and independent. The coherence properties of such created photons can be quantitatively described by their bandwidth[2] $\lambda/\Delta\lambda$ and the phase space volume (or *emittance*) $(\sigma\sigma')^2$, while λ is the wave length and $\Delta\lambda$ its variance, σ is the source size and σ' the divergence of the photon beam. The requirement for a spatially coherent beam,

$$\sigma_x \sigma'_x \sigma_y \sigma'_y < \left(\frac{\lambda}{4\pi}\right)^2 \quad , \tag{3.1}$$

is usually *not* satisfied in the X-ray regime [AHK85]. Hence, when talking about synchrotron radiation one may refer to *partially coherent* light. An improvement of the coherence can be achieved by limiting the phase space volume. Introducing collimating apertures into the beam path shrinks the phase space volume and allows a wider range of (shorter) wavelengths to satisfy equation (3.1). This technique however has a huge drawback: it dramatically reduces the photon flux. Besides, shifting towards smaller wavelengths additionally leads to a reduction of the coherent flux as can be understood from the quantitative description of the coherent fraction of the photon flux, given by [GZ04]:

$$F_{\mathrm{coh}} = \left(\frac{\lambda}{2}\right)^2 \mathcal{B} \tag{3.2}$$

$$\text{with} \quad [\mathcal{B}] = \frac{\text{photons/second}}{\text{mrad}^2\,\text{mm}^2\,0.1\,\%\text{BW}} \quad .$$

Here, $\mathcal{B}$ is the brilliance of the source, given in photons per second, normalized by opening angle in mrad^2, source size in mm^2 and bandwidth cut-

[2] While a bandwidth is typically defined as $\Delta w/w$, here the relation $\lambda \propto 1/w$ is used to express the bandwidth in therms of the wavelength λ.

off.

3rd generation undulator sources[3] provide a brilliance up to the order of $10^{21}\,\mathrm{ph\,s^{-1}\,mrad^{-2}\,mm^{-2}(0.1\%BW)^{-1}}$ [And+15]. As already mentioned, there are two aspects of coherence – longitudinal and transversal – according to the propagation direction of the beam. Undulator radiation has the advantage of a relatively high longitudinal coherence, compared to X-ray radiation produced through different devices in a storage ring, such as Wigglers or Bending Magnets [AHK85]. Besides, its transversal coherence needs to be improved, as will be addressed later.

The longitudinal coherence length, ξ_l, takes into account the monochromaticity (energy distribution) of the light. Figure 3.2 schematically presents propagating plane wave fronts with (A) wavelength λ and (B) slightly detuned $(\lambda - \Delta\lambda)$, accordingly. Both plane waves are in phase at point O. $2\xi_\mathrm{l}$ defines the segment $\overline{OP}$ within which both plane waves are in phase again:

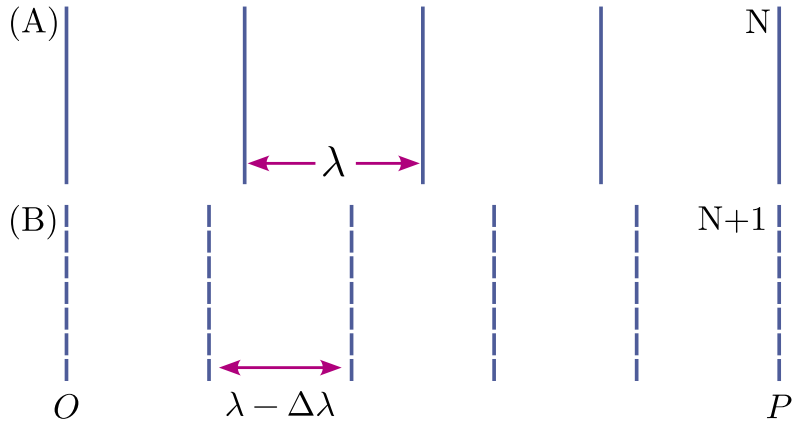

Figure 3.2: Sketch of the derivation of the longitudinal coherence length.

[3] At synchrotrons, X-ray light is usually produced by one out of two devices: *Bending Magnets* or *Insertion Devices*. The latter apparati split again into so called wigglers and undulators. Without commenting on the underlying principles – an excellent textbook would be reference [AM11] — up-to-date undulators provide the highest flux of coherent X-ray light.

$$2\xi_\mathrm{l} \doteq N\lambda = (N+1)\cdot(\lambda - \Delta\lambda)$$
$$\Leftrightarrow \lambda = \Delta\lambda(N+1) \ .$$

This leads to an expression $\xi_\mathrm{l} = {}^{\lambda^2}/_{(2\Delta\lambda)} - {}^{\lambda}/_{2}$. The term ${}^{\lambda}/_{2}$ is usually neglected as it scales with ${}^{\Delta\lambda}/_{\lambda}$ compared to the first term and the monochromaticity of undulator radiation typically is in the order of ${}^{\Delta\lambda}/_{\lambda} \approx 10^{-4}$ or less [GZ04]. With that we can conclude

$$\xi_\mathrm{l} \approx \frac{\lambda^2}{2\Delta\lambda} \ . \tag{3.3}$$

The longitudinal coherence length, ξ_l, arises from the finite size of the light source σ. As a result, the X-ray beam diverges. Figure 3.3 depicts the geometry of that situation. Given two wave fronts (A) and (B), which are in phase at point P, the transverse coherence length ξ_l may be defined as twice the distance it takes to count a phase shift of one wavelength λ. This can be expressed through

$$\Delta\Theta = \arctan\left(\frac{\lambda}{2\xi_\mathrm{t}}\right) \ .$$

With a source-to-sample distance R, a second relation ${}^{\Delta\Theta}/_{2} = \arctan\left({}^{\sigma}/_{2R}\right)$ for the aperture angle $\Delta\Theta$ can be found as both triangles, which enclose $\Delta\Theta$, are similar triangles. Under the assumption of ${}^{\sigma}/_{R} \ll 1$ we can linearly approximate the arctan function and combine both equations getting an expression for the transversal coherence length

$$\xi_\mathrm{t} = \frac{\lambda R}{2\sigma} \ . \tag{3.4}$$

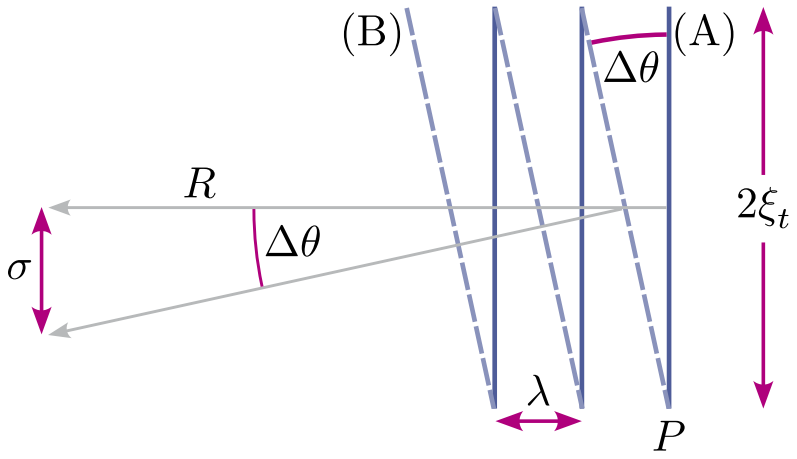

Figure 3.3: Sketch of the derivation of the transversal coherence length.

The path length difference (PLD), δs, is a parameter, based to the thickness of the sample l and the beam diameter w, which needs to be taken into account. Figure 3.4 shows the PLD's impact on the beam's pathway. Both effects will be considered separately. The two components sum up to the total PLD $\delta s = \delta s_1 + \delta s_2$. Panel (a) of figure 3.4 displays the effect of the finite beam size regarding half the beam waist. This results in a PLD of $\delta s_1 = {}^{w}/_{2}\sin(\theta)$. Panel (b) of figure shows the influence of the sample thickness. As a scattering event may occur somewhere between the front and the backside of the sample (neglecting multiple scattering events[4]), a maximum PLD of $\delta s_2 = l[1-\cos(\theta)] = 2l\sin^2({}^{\theta}/_{2})$ may built up. With that, a total PLD can be expressed by

$$\delta s = \frac{w}{2}\sin(\theta) + 2l\sin^2\left(\frac{\theta}{2}\right) \quad . \tag{3.5}$$

As δs emerges along with the propagation direction, it mainly affects the longitudinal coherence ξ_l. With that, one can conclude that, to preserve longitudinal coherence, the following requirement needs to be fulfilled:

[4] Born-Approximation, [PT85, sec. 4.4]

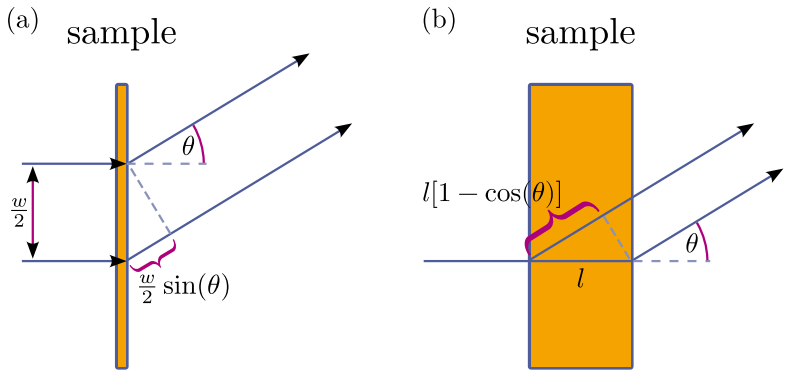

Figure 3.4: (a) Beam path length difference due to beam width w. (b) Path length difference due to sample thickness l.

$$\delta s < \frac{\lambda^2}{2\Delta\lambda} \quad . \tag{3.6}$$

A quantitative view on these constrains will be given in section 3.6, where the setup of an XPCS beamline is discussed exemplarily.

3.3 Overview on scattering

A useful picture to describe an electro-magnetic wave is the *plane wave* description. It is defined by its amplitude E_0, frequency ν and wavelength λ and propagates along the $\hat{z}$-axis:

$$E(z,t) = E_0 \cos\left[2\pi(z/\lambda - \nu t)\right] \quad .$$

A more convenient formulation for further calculus uses the complex notation, with angular frequency $\omega = 2\pi\nu$ and wave number $k = 2\pi n/\lambda$. As the index of refraction almost equals unity for the X-ray regime, it will be neglected in the following equation[5]:

[5]The index of refraction for X-rays $n = 1 - \delta + \imath\varepsilon$ can easily be assumed to be unity as for many solids $\delta \approx 10^{-5}$, in air even $\delta \approx 10^{-8}$ [De 16].

$$E(z,t) = E_0 \exp\left[i(kz - \omega t)\right] \ . \tag{3.7}$$

Considering the electro-magnetic wave as an oscillatory electro-magnetic field, MAXWELL's equations well describe the interaction of such a field with charged particles (i.e. electrons). In this section, the geometrical implications of elastic scattering processes ($k \doteq |\boldsymbol{k}_{\text{in}}| = |\boldsymbol{k}_{\text{out}}|$) are described.

3.3.1 Single particle scattering

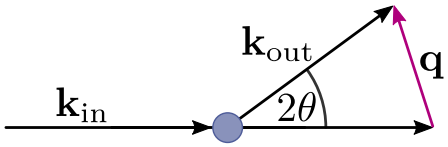

Figure 3.5: Definition of the momentum transfer $\boldsymbol{q}$ (inspired by [De 16]).

The simplest scattering scenario is the scattering of an electro-magnetic wave by a single scatterer (electron) as outlined in figure 3.5. The typical notation makes use of the incoming and outgoing wave vectors $\boldsymbol{k}_{\text{in}}$ and $\boldsymbol{k}_{\text{out}}$ which define the *scattering angle* 2θ. The nomenclature uses the factor 2 following the usual notation in diffraction and being used here for consistency reasons. All information on that simple scattering process can be summed up within one single variable, the so called *momentum transfer* $\boldsymbol{q}$, which is defined as the wave vector change throughout the scattering process $\boldsymbol{q} = \boldsymbol{k}_{\text{out}} - \boldsymbol{k}_{\text{in}}$. Besides, the geometrical relation

$$q \doteq |\boldsymbol{q}| = \frac{4\pi}{\lambda} \sin\theta \ , \tag{3.8}$$

describing the absolute value of the momentum transfer, will be useful in the following.

3.3.2 Multiple particle scattering

Coming to a more general picture including the implications of coherence, hence, *interference*, the scenario of the prior section is extended by including

a second scatterer. Figure 3.6 sketches two scatterers A and B, which are separated by vector $\boldsymbol{r}$. From geometrical considerations, the incoming plane wave, which is scattered under the same scattering angle 2θ, hence wave vector $\boldsymbol{q}$ by each scatterer, undergoes different path lengths according to the relative position of both scatterers.

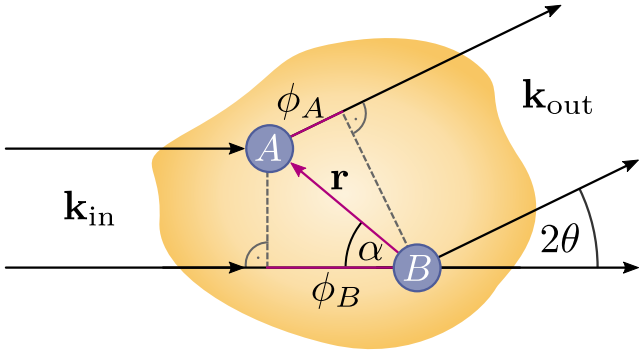

Figure 3.6: Sketch of a sample with two scattering centres. The different path lengths of result in phases shifts ϕ_j built up by relative locations of different scatterers (inspired by [De 16]).

Each part of the plane wave collects an extra phase shift $\phi_j = kr\cos\alpha_j = \boldsymbol{k}\cdot\boldsymbol{r}_j$, according to the relative location $\boldsymbol{r}$ compared to the other scatterer. The total path length difference can be expressed by the phase shift

$$\Delta\phi(\boldsymbol{r}) = -\boldsymbol{k}_{\text{in}}\cdot\boldsymbol{r} + \boldsymbol{k}_{\text{out}}\cdot\boldsymbol{r} = \boldsymbol{q}\cdot\boldsymbol{r} \ . \tag{3.9}$$

With expression (3.9) can be seen, how the simplicity of expressing a phase shift in terms of $\boldsymbol{q}$ manifests the usefulness of the scattering vector notation.

Considering the captured quantity being an intensity I, rather than a field term, the relation $I = |E|^2 = EE^*$ – while E^* stands for the complex conjugate of E – implies that the constant terms $\exp[\pm\imath\omega t]$ aggregate to unity and leave only the phase term, hence, equation (3.9), being non-unity. Expanding to continuum we make use of the scatterer number density $n(\boldsymbol{r})$. With the knowledge, that each scatterer yields a phase factor, the integral for the

scattering amplitude of a continuum of the equal scatterers (electrons)[6] can be expressed by [De 16, Chpt 2]:

$$F^{\text{atom}}(\boldsymbol{q}) \propto \int_V n(\boldsymbol{r}) \exp\left[\imath \boldsymbol{q} \cdot \boldsymbol{r}\right] \mathrm{d}\boldsymbol{r} \ . \tag{3.10}$$

It is noteworthy that this expression is identical to the Fourier transformation (FT) of the electron density. Hence, from $F^{\text{atom}}(\boldsymbol{q})$ the pair correlation function[7] $g(\boldsymbol{r})$ can be calculated.

To attain a more realistic situation, equation (3.10) can be further extended by taking into account multiple atoms. The summation over N variously arranged atoms can be understood as the scattering amplitude generated by a liquid or a disordered solid and leads to the expression

$$F^{\text{liq}}(\boldsymbol{q}) = \sum_{\boldsymbol{r}_j}^{N} F_j^{\text{atom}}(\boldsymbol{q}) \exp\left[\imath \boldsymbol{q} \cdot \boldsymbol{r}_j\right] \ . \tag{3.11}$$

For a high number of atoms N, the summation over all atoms allows to simplify the equation, which is especially reasonable in disordered systems: Regarding the average of the phase factor, one can make use of the relation $\langle \exp\left[\imath \boldsymbol{q} \cdot \boldsymbol{r}_j\right] \rangle = \operatorname{sinc}(q r_j)$ [De 16, Chpt 2]. It should be pointed out, that the arguments of the sinc-function, q and r_j are no longer vectors, but instead their absolute values. Finally, the overall intensity of an illuminated sample can be calculated, as it is the averaged mean square of the scattering amplitude:

[6] Also called the *atomic scattering factor*.
[7] Also known as the radial distribution function.

$$
\begin{aligned}
I(q) &= \langle |F^{\mathrm{liq}}(\boldsymbol{q})|^2 \rangle \\
&= \sum_j \sum_k F_j(\boldsymbol{q}) F_k(\boldsymbol{q}) \operatorname{sinc}(q r_{jk}) \\
&= N F^2(\boldsymbol{q}) + F^2(\boldsymbol{q}) \sum_{j \neq k} \sum_k \operatorname{sinc}(q r_{jk})) \\
&\overset{(\#1)}{\approx} N F^2(\boldsymbol{q}) \underbrace{\left[1 + N \sum_k \operatorname{sinc}(q r_k) \right]}_{\doteq\ S(q)} \\
&\qquad \text{with} \quad r_{jk} = r_k - r_j \ .
\end{aligned}
$$

For large particle numbers N, simplification (#1) $N(N-1) \approx N^2$ is applied. As a result, on the right hand side the factor $S(q)$ is derived. This factor describes the *inter*-particle interactions and is called the *(static) structure factor* [De 16, Chpt 2].

3.4 Coherent illumination of disordered systems

In a simple scattering case, with only one single symmetric scatterer, the scattering amplitude $F(\boldsymbol{q})$ can be calculated following equation (3.10) – being identical to the FT of the scatterer number density $n(\boldsymbol{r})$. In order to visualize the effect of the FT, a simple symmetric scatterer with radius r is used while the numerical framework of the discrete FT is applied.

The FT can easily be calculated by means of open-source libraries of various programming languages. Here the `python` language is used, while the numerical calculation of the *discrete Fourier transformation* (implemented by the algorithm of the Fast Fourier Transformation (FFT)) is performed within the framework of the `numpy.fft.fft2` function [Har+20]. In the following `python`-like pseudo-code the modelling of the diffraction process is schematically lined out. After generating three images of $N \times N$ pixels of value 0 (`img0, img1, img2`), in the centre of `img0`, a circle with value 1 is drawn. While seven further circles (scatterers), arranged randomly, non-overlapping, are identically

located in `img1` and `img2`, a ninth circle is put at different locations in the two images `img1` and `img2`. An FFT of all images is calculated and the resulting matrices are rescaled by their minimal and maximal value. In order to point out the implication of the relocation of one scatterer, the difference $\texttt{FFT[img}_1\texttt{]-FFT[img}_2\texttt{]}$ is calculated and plotted.

python-like pseudo-code

```
import numpy as np
img0 = np.zeros((4000,4000))
scatterer = np.ones(shape='circle', diameter=19)
img0 += scatterer(loc='center')
img1 = img0 + 8*scatterer(loc='around center')
img2 = img1 - scatterer(loc='location9') + scatterer(loc='location10')
imgs = [img0, img1, img2]

# calculate ffts
fts = []
for img in imgs:
  ft = np.fft.fft2(img)
  ft = normalize_by_min_max(ft)
  fts.append(ft)

# calculate difference between ffts with one relocated scatterer
diff_scatterer_loc = fts[1] - fts[2]
plot(diff_scatterer_loc)
```

Figure 3.7 (a) shows a single symmetric scatterer in the central 1000 px × 1000 px section of a 4000 px × 4000 px volume. The scatterer has a diameter of 19 px. As a result of the FFT, figure 3.7 (b) shows the formation of centro-symmetric rings, while only the two most central ones are displayed in the cropped section of the entire (4000 px × 4000 px) image. These rings are called *diffraction rings* and are characteristic for X-ray scattering.

The discretisation of the scatterers ("pixelation") results in a slight deformation of the rings, which can be noted by having a closed look to the rings. This distortion as well as box effects from the numerical calculus are not further considered here[8]. In between two *diffraction rings*, the intensity varies

[8] Drawing a round pattern in a pixelated matrix technically leads to a discrete, pixel by

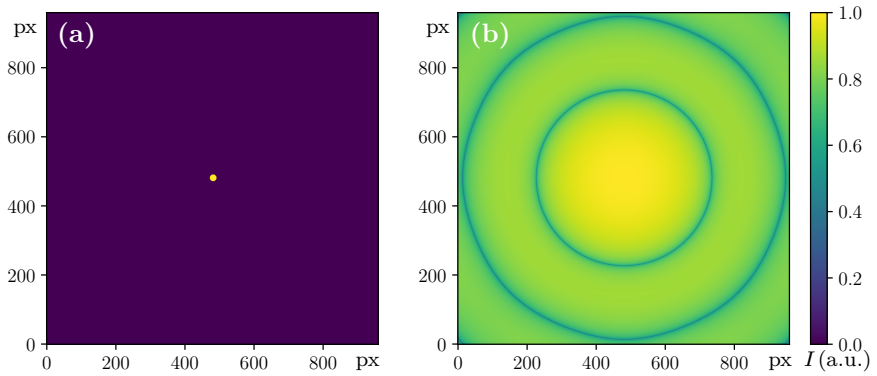

Figure 3.7: (a) Central section of a 4000 px×4000 px area with a central single symmetric scatterer. (b) Central section of the discrete Fourier transformation of panel (a). Logarithmic colour scale. Recalculated after [Kwa12].

homogeneously and the distance between the rings is characteristic for the length scales present in the scattering volume. In this simple scenario, the diameter of the single point-symmetric scatterer is the only relevant length scale present, whereas the influence of pixelation and box builds a significant influence at higher orders, further away from the centre. These higher orders are not shown here.

As seen in section 3.2, X-ray radiation also has – even if only partial – coherent properties. Coherence plays a crucial role when more than one scatterer is present in the illuminated volume. That case is depicted in figure 3.8 (a) where nine scatterers are packed relatively dense but arranged randomly. Because the FFT formalism is capable of using complex numbers, the so called *coherent scattering part* is taken into account as well as the incoherent scattering part. While the incoherent part forms the same pattern of diffractions rings, the coherent part forms a randomly appearing and homogeneously spread pattern of small intense spots on top of the diffraction rings – the *speckle pattern*. This pattern depicts a signal which alternates on a relatively small lateral scale between high signal, corresponding to constructive interference, and low signal (destructive interference). The speckle pattern is a direct consequence of the coherence of the beam, being an interference pattern ex-

pixel, stepped "curvature". This results in the discretisation of two (normal) surface orientations which distort the expected round shaped diffraction pattern by predominant directions of the pixelated circle.

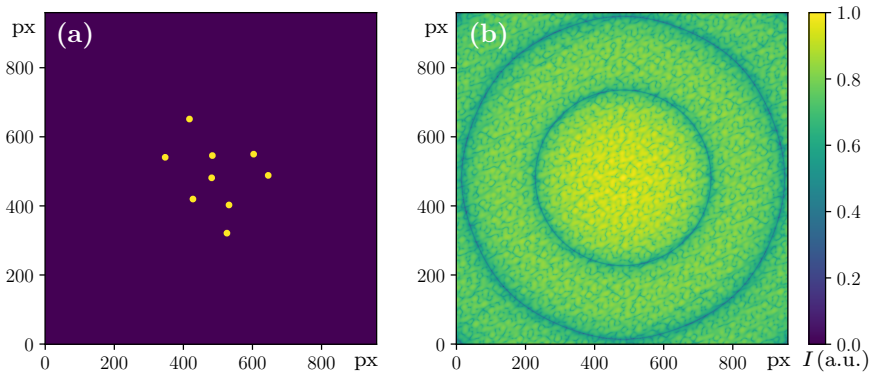

Figure 3.8: (a) Central section of a 4000 px × 4000 px 2-dimensional volume with nine randomly arranged symmetric scatterers. (b) Central section of the discrete FT of panel (a), showing diffraction rings with a speckle pattern on top. Logarithmic colour scale. Recalculated after [Kwa12].

actly determined by the arrangement of the scatterers [GZ04]. With that, it becomes a powerful tool to detect small changes of the scatterer's arrangement.

A minor change of the scatterer's arrangement is modelled as shown in figure 3.9 (a) where the upper left "particle" is moved towards the right (compare fig. 3.8 (a)). Its FFT is *not* shown as there is no difference visible easily by eye. However, calculating the difference Δ of both Fourier transformed density distributions (FFT of fig. 3.9 (a) and of fig. 3.8 (a))

$$\Delta = \mathrm{FFT}[\rho_{\text{particle moved}}(\boldsymbol{r})] - \mathrm{FFT}[\rho_0(\boldsymbol{r})] \ ,$$

reveals a repetitively alternating signal with strong contrast (values from -0.5 to 0.5, see fig. 3.9 (b)). It is homogeneously spread over the entire image area. Moreover, the diffraction rings are not visible anymore as they cancel out each other, which means that they are identical and the deviation is only in the speckle pattern. Given that conclusion as well as the fact that the model data is normalised, the strong signal of Δ emphasises the scientific relevance of speckle analysis techniques in order to study arrangement changes

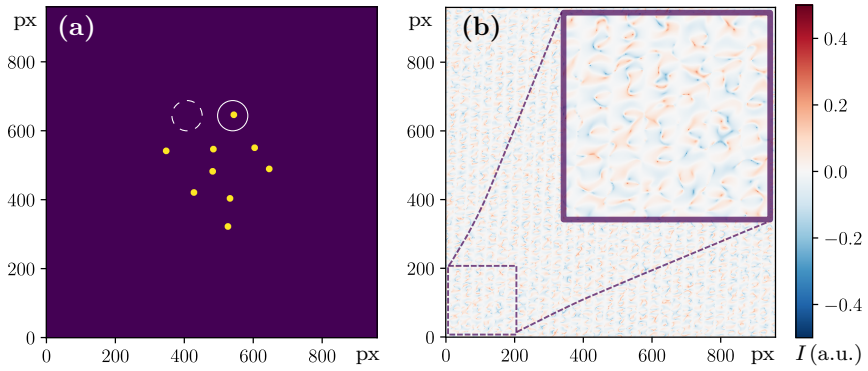

Figure 3.9: (a) Almost the same arrangement as in fig. 3.8 (a), but the upper left "particle" was moved towards the right. (b) Difference between the FFT in fig. 3.8 (b) and the FFT of the 3.9 (a). Its upper right inset depicts a magnification of the first 200 by 200 px.

of disordered systems: a small change in the arrangement leads to a vast change in the speckle pattern.

3.5 Time correlation functions and structural dynamics

In the previous section it is pointed out how the arrangement of disordered scatterers can be represented by means of a coherent light throughout its speckle pattern. So far, only light is shed on the static arrangement – a snapshot, while the atomic arrangement of metallic glasses in real systems is subjected to spontaneous rearrangements. This spontaneous structural dynamics is accessible to be studied with the tools and concept introduced so far. Within this section, the mathematical tools in order to describe structural dynamics in metallic glasses are illustrated.

The correlation of a coherent X-ray beam can be quantified by first- and second-order correlation functions of the $\boldsymbol{E}$ field. In experimental studies a relatively long acquisition time T of currently used X-ray detectors compared to the coherence time τ_0 of the X-ray photons, given through $\tau_0 = \xi_l/c$, i.e. $T \gg \tau_0$, allows to assume Poisson statistics [Gla63; Lou00]. From that, the

correlation functions can be written

$$g^{(1)}(\boldsymbol{q},t) = \frac{\langle \boldsymbol{E}^*(\boldsymbol{q},t_0)\boldsymbol{E}(\boldsymbol{q},t_0+t)\rangle_T}{\langle |\boldsymbol{E}(\boldsymbol{q},t_0)|^2\rangle_T}$$
$$g^{(2)}(\boldsymbol{q},t) = \frac{\langle I(\boldsymbol{q},t_0)I(\boldsymbol{q},t_0+t)\rangle_T}{\langle I(\boldsymbol{q},t_0)\rangle_T^2} \quad , \tag{3.12}$$

while * denotes the complex conjugate, $\langle\cdots\rangle_T$ the temporal averaging over the acquisition time and $\boldsymbol{q}$ the momentum transfer. For a chaotic X-ray source the Siegert relation holds, completely determining $g^{(2)}(t)$ throughout $g^{(2)}(t) = 1 + |g^{(1)}(t)|^2$ [Sie43; Kir+96; Len01].

As introduced in the previous sections, temporal changes of the spatial arrangement of scatterers in disordered systems can be studied by means of coherent scattering. A measurement of the intensity fluctuations of the X-ray speckle pattern can reveal the underlying dynamics of the scatterers (atoms) of the sample [Sut+91]. Experimentally accessed fluctuations can be quantified using the normalised intensity correlation function $g^{(2)}(\boldsymbol{q},t)$ from equation (3.12) and related to the normalised intermediate scattering function $f(\boldsymbol{q},t)$ [GMR08; Leh12; MFR15]:

$$g^{(2)}(\boldsymbol{q},t) = 1 + c(\boldsymbol{q})|f(\boldsymbol{q},t)|^2 \quad . \tag{3.13}$$

Therein $c(\boldsymbol{q})$ denotes the q-dependent contrast and $f(\boldsymbol{q},t) = {}^{F(\boldsymbol{q},t)}/_{S(\boldsymbol{q},0)}$. The ISF represents the temporal and spacial evolution of the density correlations of the sample and is the representation of the dynamic structure factor $S(\boldsymbol{q},\omega)$ in reciprocal-space and real-time variables as introduced in section 3.3.

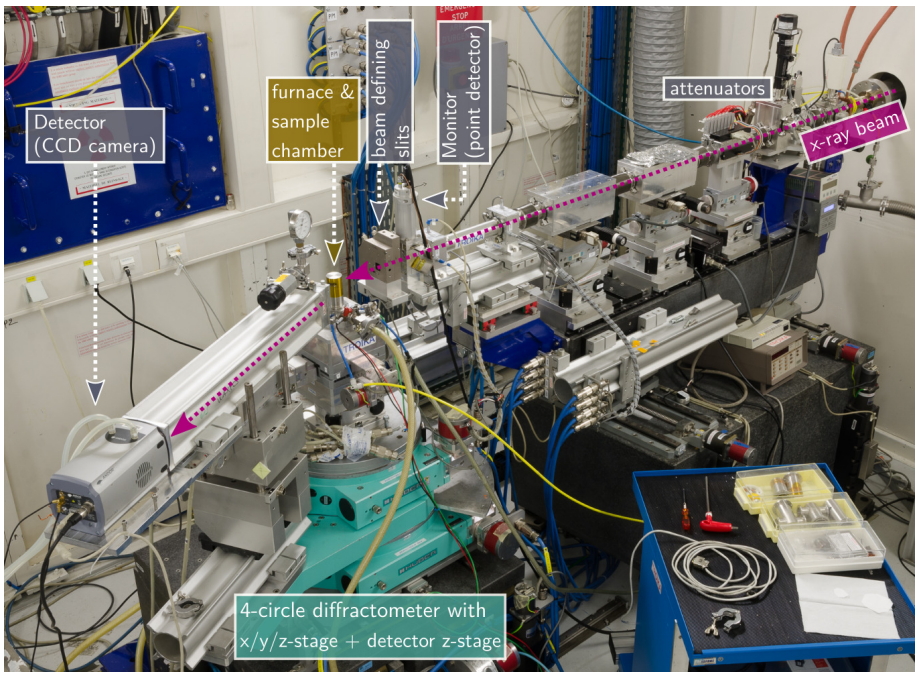

Figure 3.10: Wide-angle XPCS setup at ID10 EH2, ESRF

3.6 Experimental realisation of XPCS

First XPCS studies have been conducted by Dierker et al. and by Thurn-Albrecht et al. on suspensions of colloidal gold and platinum in viscous liquid glycerol, respectively, to study diffusion upon Brownian motion [Die+95; Thu+96], while first XPCS experiments on metals have been carried out by Leitner et al. [Lei+09]. Alike the two latter, the data of this thesis, determined by XPCS, are collected at beamline ID10 EH2 of the ESRF, Grenoble. A line up of the experimental environment is addressed in this section.

3.6.1 XPCS setup at ID10 (ESRF)

Figure 3.10 shows the front area of experimental hutch (EH) 2 of beamline ID10 at the ESRF, Grenoble, prepared for a typical XPCS experiment. XPCS experiments are usually performed at a photon energy of 8.1 keV

($\widehat{=}$ 0.153 067 nm wavelength) being the energy at which the highest coherent X-ray flux can be provided at the given geographical section of the beamline with respect to the storage ring. After the beam is prepared by optical instruments in the corresponding optics hutches (OHs), the beam arrives through a front-end into EH2, marked by the label "x-ray beam" in figure 3.10. From there, the beam passes through a box of attenuators, where its intensity can be reduced if necessary, and further local optical instruments. Before the final beam defining slits, a point detector is installed to continuously monitor the beam intensity. Right after the slits, the sample is positioned on a four-circle diffractometer located approximately 61 m downstream from the X-ray undulator source. The sample is mounted in transmission geometry in a home-made furnace, which also acts as the sample chamber and is specifically customised regarding the needs of the beamline and the XPCS experiment. The furnace is capable of providing a particular gas atmosphere (or high vacuum) and the temperature can be regulated between ambient temperature and 1000 °C. In particular, it furnace can provide very high temperature stability $\Delta T < \pm 0.05\,\mathrm{K}$. At a distance of 0.5 m to 2.0 m downstream of the sample, a charge-coupled device (CCD) X-ray detector is positioned. It is chosen in order to match the detector's pixel size with the speckle size. A flight tube between the sample and the detector suppresses scattering of the deflected beam and air. Within this thesis at ID10 EH2 of the ESRF, Ikon-M cameras by Andor with a resolution of 1024 px × 1024 px and a pixel size of 13 µm, employing a back-illuminated deep-depleted deep-cooled CCD sensor, are used. Further technical details on the beamline and XPCS realisation are given by Grübel and Zontone [GZ04].

3.6.2 Atomic dynamics through wide-angle XPCS

By positioning the detector at the maximum of the FSDP, rearrangements in the special regime of neighbouring scatterers (atoms) yield the main contribution to the scattering signal, hence, *local* atomic dynamics is what this geometry is sensitive to. Therefore, the detector (CCD) is put into wide-angle geometry given by the spatial location of the FSDP and the photon energy of the X-ray beam (respectively wavelength). With that, equation (3.8) gives a

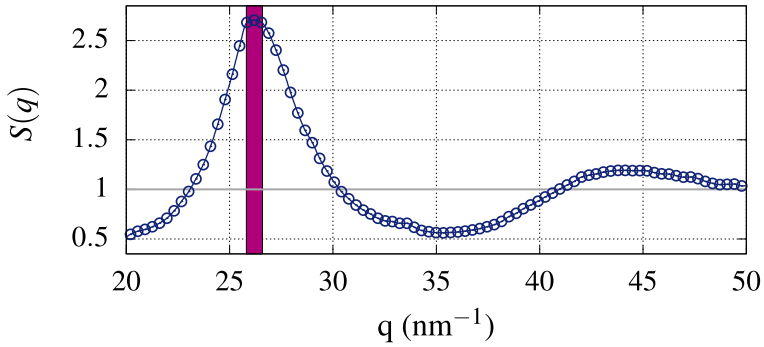

Figure 3.11: Exemplary static structure factor of a Cu-Zr VD MG measured at ID15 (ESRF), showing the coverage of momentum transfer of a typical XPCS measurement at ID10 (ESRF). The purple box indicates the size of the CCD detector's sensitive area in reciprocal space. The blue line is just a guide to the eye.

scattering angle in the proximity of 35° to 45° for MGs. Figure 3.11 exemplarily depicts $S(q)$ for a Cu-Zr based MG. The purple coloured box indicates the location and geometrical width of a CCD located at the centre of the FSDP. From this graph, it is plausible that the captured signal from the CCD is mostly flat across the entire chip of the camera.

3.6.3 Sample thickness

In order to preserve the coherent properties of the beam, it is important to keep the inequality (3.6) fulfilled. For the given longitudinal coherence length $\xi_l \approx 1\,\mu m$, a simple estimation of the coherence condition is depicted in figure 3.12. The horizontal, coloured line at $\xi_l = 1\,\mu m$ illustrates the estimated value for ξ_l as published by the research facility[9]. The scattering angle dependent PLD $\delta s(\theta)$ is calculated for two sample thicknesses of $l_1 = 5\,\mu m$ and $l_2 = 20\,\mu m$. While for both sample thicknesses the PLD lies close to the estimated ξ_l, for l_2 the resulting PLD exceeds the ξ_l at typical scattering angles of $\theta \approx 40°$, and hence, the limit of the coherence condition in equation (3.6).

[9]The coherence length ξ_l is given in the description of the beamline at section "Polarization and Coherence Properties" at the following link https://www.esrf.fr/home/UsersAndScience/Experiments/CBS/ID10/ID10EH2/BeamlineDescription.html#troikaIII (retrieved at 2023-03-30T19:21:21+02:00).

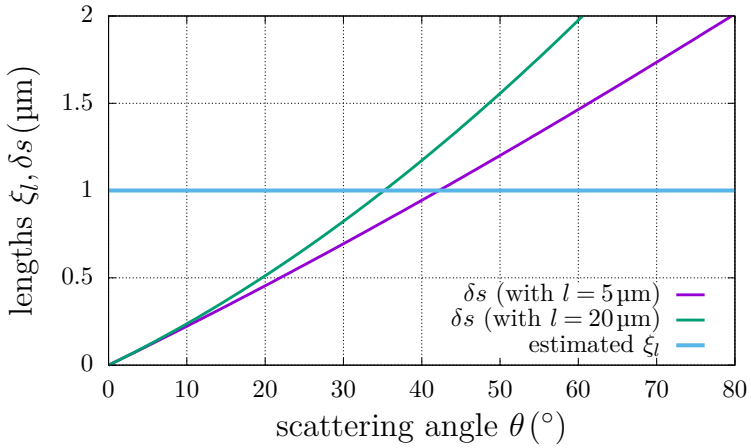

Figure 3.12: Longitudinal coherence length and path length difference for different sample thicknesses vs. scattering angle. Estimated longitudinal coherence length $\xi_l \approx 1\,\mu\text{m}$.

This certainly is a reason for the low signal-to-noise ratio (SNR) of the speckle patterns in XPCS experiments. The acceptable δs hence, limits the maximum possible sample thickness. In contrast, thicker samples have a higher scattering cross-section and thus, result in a larger scattering signal. From that arises a trade-off which sets the range for an optimum sample thickness, depending on the position θ at which the detector should be positioned, or in other words, it depends on the position of the FSDP in the here described XPCS setup.

3.7 Analysis of XPCS data

3.7.1 Preparation of raw data

XPCS data are captured under the aforementioned conditions. Single frames of detector data are captured and a dark image, that is an averaged series of 100 images with no X-ray beam, is subtracted pixel-by-pixel from each frame to account for dead pixels or broken areas of the detector. The resulting $N \times N$ pixel images are considered raw data. Typical photon densities are in the order of $0.0001\,\text{photons}\,\text{px}^{-1}\,\text{s}^{-1}$ and make commonly used pixel-by-

pixel intensity correlation calculations over the entire detector for all frames (usually one thousand or more) very inefficient. Chushkin et al. developed a droplet algorithm which maps registered analogue-to-digital units (ADUs) to numbers of impinging photons per pixel within the acquisition time [CCM12]. From that map of "photon events", a one-dimensional list is generated registering the pixel number. In case of multiple photon events per pixel, such an event entry is registered multiple times in that list. As the number density of photons per pixel is very low, it is much faster to calculate the correlation function from that list of photon events as from the entire pixel matrix with mostly ADU values corresponding to zero photons.

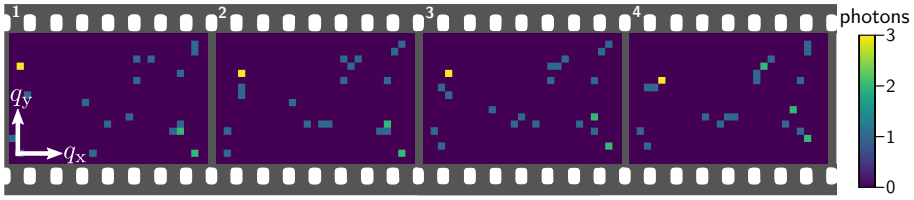

Figure 3.13: Scheme of sequentially captured data frames with typical photon density after applying droplet algorithm by Chushkin et al. [CCM12].

Figure 3.13 schematically illustrates four subsections of subsequent frames of captured speckle intensities after applying the droplet algorithm. Most pixels are coloured in dark blue, showing that no photon impinged within the acquisition time. A few pixels show one registered photon, rarely two, and once per frame three photons impinge at the same pixel within one frame (indicated by the yellow colour). These speckle patterns relate directly to the arrangement of the scatterers (atoms) according to the underlying physics as described in sections 3.3 and 3.4.

3.7.2 Two-time correlation function

Calculating the correlation function, either pixel-by-pixel or using the event correlator technique, reveals the temporal dynamics of the scatterers which can be illustrated by an $N \times N$ matrix of colour-coded correlation function $g^{(2)}(\boldsymbol{q}, t)$ – the TTCF. An exemplary TTCF for a distinct value of q is shown in figure 3.14, whereby this illustration shows an asymmetric subsection of

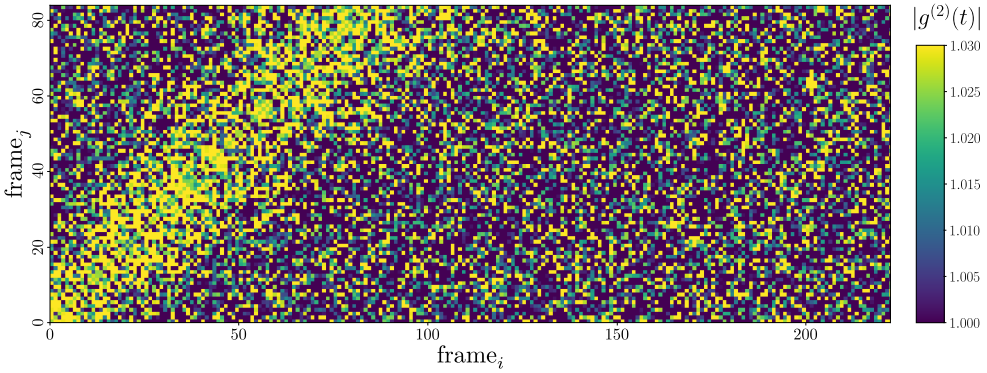

Figure 3.14: Section of a TTCF calculated from XPCS data subjected to the droplet algorithm and event correlation as introduced by Chushkin et al., while no Gaussian to blur the data is applied [CCM12].

the entire TTCF. Often, when TTCFs are shown, they are convoluted with a Gaussian function in order to mitigate the noise. Within this chapter, this function is not applied if not indicated differently.

All these analysis steps are conducted with software which is usually provided by the beamlines, as for instance the framework of `waxpcs.py`, a `python` framework used at the ESRF, or alike for beamlines from other synchrotron facilities.

As this time-resolved correlation function is subjected to a high value of noise, it is usually time-averaged over one entire TTCF or over portions of it. The resulting normalised intensity auto-correlation function (3.12) is usually analysed through best fits of the empirical Kohlrausch-Williams-Watts (KWW) function to quantify the dynamics [Koh54; WW70; Moy+76]

$$f(t) = A + c(q) \exp\left[-2\left(\frac{t}{\tau}\right)^{\beta}\right] \quad . \tag{3.14}$$

The baseline parameter A should be unity according to equation (3.13) and is often varied to satisfy systematic deviations. $c(q)$ can be directly related to the q-dependent contrast of the aforementioned equation, and additionally depends on machine parameters such as the degree of partial coherence. τ

denotes the relaxation time, and β is the KWW shape parameter, which shapes the exponential decay either stretched or compressed. The physical interpretation of β is highly under debate [Mad+10; Rut+13a; GBS15; CB17; Bou+17; Liu+17; Wu+18; Hec+18; Rut+20].

3.7.3 Two interpretations of the TTCF

According to its calculation, the two-dimensional TTCF can be evaluated in different directions. First of all, it is important to recapitulate how it is calculated. It can be read like an $N \times N$ matrix, wherein each element $\mathrm{TTCF}_{i,j}$ $(i, j \in N)$ equals the value of an intensity-intensity correlation function $g^{(2)}(i, j)$ of the captured frames i and j. From that arises, that the evolution of the observation time, also called experimental time t_{exp}, evolves along with the main diagonal, because later captured frames are correlated with themselves towards the upper right corner along the white arrow titled "observation time" in panel 3.15a. Because of this symmetry of that operation, a TTCF is symmetric with the main diagonal being the symmetry axis.

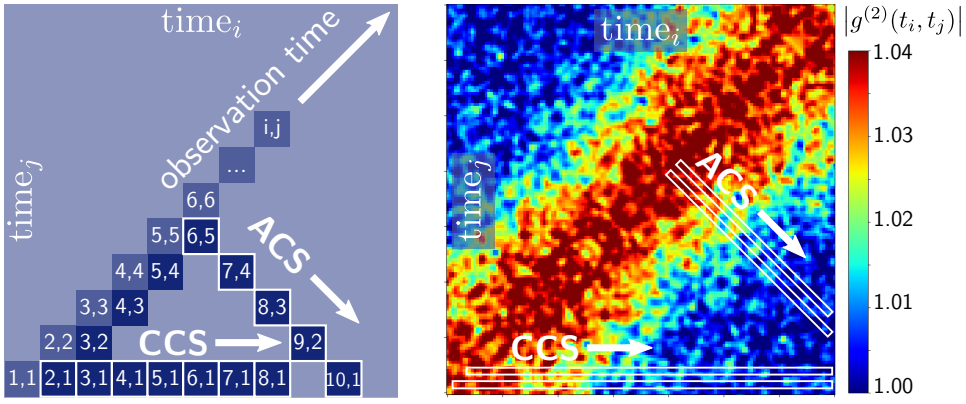

(a) TTCF calculation scheme **(b)** Gaussian filtered TTCF of 140 frames

Figure 3.15: (a) Calculation scheme of a TTCF. Lighter blue squares (frames of $i = j$) indicate auto-correlations. White-framed squares show two possible interpretations of a TTCF – along the CCS-axis and along the ACS-axis, respectively. (b) Gaussian filtered ($\sigma = 1.0$) TTCF of 140 frames. White boxes indicate cuts along the two different coordinate systems.

The following interpretations refer to the lower right triangular half of the

TTCF. At the first glance, it may be evident to evaluate the TTCF along with horizontal lines. The conventional coordinate system (CCS) represents the dynamics with respect to the initial arrangement of that line $(i, j = i)$. For later (upper) horizontals, i is iterated, and the dynamics is calculated with respect to its own initial configuration, e.g. $(i + 1, j = i + 1)$ for the second horizontal. So far, this coordinate system behaves as expected and probably as intended. However, as glasses are subjected to history dependence, a sample's age needs to be considered. This consideration only works well in the CCS if a single horizontal line is regarded. When multiple horizontal lines of the TTCF are averaged, the dynamics of the sample at different ages (sample times) are mixed. This complicates an analysis of possible transitions a glass may undergo during aging and could hide imprints of new findings. Because TTCFs are very noisy (see fig. 3.14), rigorous averaging is generally necessary for a quantitative analysis of the dynamics captured by XPCS.

An alternative coordinate system (ACS) is proposed to overcome that deficiency [Bik17]. Therein, the one-time correlation function is calculated orthogonally to the main diagonal as sketched in panel 3.15a. In this direction, $g^{(2)}(t)$, even when averaged over multiple lines, evolves with respect to the constant sample age. The advantages of the interpretation within the ACS are applied within an extended TTCF data processing framework introduced and discussed in chapter 5. However, ACS breaks causality by mixing terms before and after an individually calculated $g^{(2)}(t)$. If that is indeed an issue needs to be investigated, as it averages out when averaging comprehensively. Panel 3.15b shows both coordinate systems on exemplary Gaussian-filtered TTCF data of a metallic glass.

3.8 Discussion

XPCS clearly became an important technique to study glasses. In particular, the spatial regime of neighbouring atoms, which is probed when the value of q is set to the FSDP, enables to investigate a regime that is hardly accessible throughout different techniques. However, the drawback of XPCS

is the necessity of a coherent flux that can only be provided by the most powerful X-ray source in the world. Such facilities are heavily sought after because they have limited capacity and only allow a limited number of experiments at the same time. Furthermore, the experimental setup is rather complex and prone to technical failure which can be rarely compensated for. Moreover, new features like intermittent dynamics have to be evaluated very carefully. They can have manifold origins, and many must be considered artefacts. In particular, abruptly appearing (and spontaneously vanishing) incidents, such as temperature instabilities of the sample environment, beam instabilities, environmental influences such as vibrations or shaking, and slipping of the sample due to insufficient clamping, may cause peculiar patterns in the TTCF that may be interpreted as "events" of intermittent dynamics. However, if all those influences can be excluded, which is claimed by several publications, such abrupt changes can be founded on underlying physics and contribute to a better understanding of the studied systems [Eve+15; RPE17; Das+19]. Confirmative findings have been made within this thesis and are described and discussed in chapter 5.

As previously mentioned, the physical interpretation of the shape parameter β is under high debate. Different techniques, which apply the KWW fit function as well, do not see $\beta > 1$ and give explanations for varying results within $0 < \beta < 1$ based on averaging homogeneous and heterogeneous dynamics [Ric93]. Since for a long time $\beta > 1$ has only been reported on from XPCS or DLS experiments, it seemed to be characteristic for these methods [Mad+10; Rut+12; GR16; Liu+17; Lüt+18; Hec+18; Ami+21]. However, compressed exponential relaxation dynamics could also be reproduced by experimental investigations on colloids [Gok+16] and in simulations [BP01; CB17; Bou+17; Wu+18]. The direction of analysis, CCS or ACS, has only little effect on the absolute value of β [Bik17]. Furthermore, $\beta > 1$ is often suggested with the presence of dynamics heterogeneities or intermittent dynamics [Bou+17; Hec+18].

3.9 Outlook

XPCS is a very demanding technique in terms of beam stability and coherent flux. With continuously progressing upgrade programs of existing X-ray sources, synchrotrons and X-ray free electron lasers (X-FELs), accessible temporal scales extend towards faster time scales, reaching sub-second to sub-microsecond for fourth generation synchrotrons, and even far below nano-seconds for X-FEL sources. These temporal regimes allow to study glasses and supercooled liquids (SCLs) not only at higher temperatures but also to investigate processes which manifest on those timescales and are not accessible at the moment while keeping the atomic length scale within the ensemble.

Moreover, the investigation of intermediate-range order could not just become accessible thanks to new generation X-ray sources. Indeed, they may enlighten new perspectives in the study of cooperative phenomenons by accessing higher-order correlation functions.

Chapter 4

Anti-Aging in $Cu_{55}Zr_{45}$ ultrastable metallic glasses

Contents

4.1 Introduction

USGs show extraordinary thermodynamic and kinetic stability, so that they form a new and promising family of glasses. Their stability is a direct consequence of the fabrication process. Initially discovered in 2007 by Swallen et al. [Swa+07], USGs have constantly gained interest in the scientific community. In particular, USGs usually exhibit a significant increase of glass

transition temperature (T_g), a decrease of fictive temperature (T_f) by several tens of Kelvin, as well as an increase of density with respect to standard quenched glasses [Swa+07; Kea+07; Swa+08; SEP13]. Besides, organic USGs show a decreased enthalpy, which seems not to be the case for their metallic counterpart [YLS13; Xue+16]. With respect to conventional glasses, USGs are considered to be in a lower state within the framework of the PEL[1] [Sti95; DS01; RAA15]. That low-energetic state is reached due to enhanced atomic mobility during the fabrication process [SP11; PS13] and is in general not accessible on practical timescales via classical methods such as long time annealing [Kea+08; Swa+08; SP11; Ber+17]. Microscopic studies on ultrastable organic glasses indicate the absence of physical aging [Leo+10], but no direct information on the underlying microscopic processes has been reported so far. With all those properties, USGs are an important building block for many applications such as pharmaceuticals or technical purposes – profiting from longer preservation of the amorphous state and its mechanical and chemical stability [HP00; Wan12].

Ultrastable metallic glasses are the representative of USGs incorporating *metallic* components, while the earlier introduced properties apply to UMGs as well, directing spotlight on them [YLS13; Wan+16; Luo+18].

In this chapter, the study of microscopic mechanisms governing structural relaxations in free-standing films of ultrastable metallic CuZr glasses is addressed by investigating their collective atomic motion. For this purpose XPCS is used to explore the evolution of density fluctuations at the length scale of inter-atomic distances on time scales up to 10^4 s, initially used on metallic glasses by Ruta et al. [Rut+12].

A subset of the results within this chapter is published in publication [Lüt+18].

[1] For more details see section 2.2.2.

4.2 Sample fabrication and preparation

The studied samples are composed of CuZr. They are vapour deposited by magnetron sputtering onto a temperature controlled polished NaCl crystal. In that way, a thin film which easily separates from the substrate can be fabricated, forming a free standing film of ca. 20 mm × 30 mm. Typically a film thickness of approximately 5 µm is chosen, as with that thickness the highest contrast throughout XPCS can be achieved, being a compromise between absorption and scattering contrast[2]. Compositional analysis by EDX reveals a homogeneous composition of approximately $55 : 45\,\%_{\mathrm{atom}}$ (Cu : Zr); details are reported in section 2.5.3).

In order to produce a so called "ultrastable" metallic glass, two deposition parameters turn out to be crucial [Lüt+18; YLS13; DLS20].

- The substrate temperature T_{sub} while depositing needs to be kept slightly below the glass transition temperature T_{g}.
- The deposition rate needs to be around or below $1.8\,\mathrm{nm\,s^{-1}}$.

To identify the ideal substrate temperature (T_{sub}), several samples are produced within a range of $T_{\mathrm{sub}} = 0.8 - 0.9\,T_{\mathrm{g}}$ at a deposition rate of $1.76(1)\,\mathrm{nm\,s^{-1}}$. Then the structural relaxation time τ – a characteristic parameter of kinetic stability – is determined for each sample throughout XPCS experiments.

In total, a set of four samples is chosen to be compared: Three samples with T_{sub} in the former given temperature range where ultrastable characteristics are expected and one sample with the substrate indirectly cooled to low temperature ($T_{\mathrm{sub}} \approx 120\,\mathrm{K}$) by a constant flow of liquid nitrogen.

XPCS is carried out at a sample temperature of 476 K, which corresponds to $0.71\,T_{\mathrm{g}}$. During this XPCS measurement the sample is kept under medium vacuum ($\mathcal{O}(p) = 1\,\mathrm{mbar}$). The resulting relaxation times are determined as described in section 3.7 and plotted versus substrate temperature in figure 4.1 for all samples. It is visible, that the highest stability is achieved by the sample produced at $T_{\mathrm{sub}} = 0.80\,T_{\mathrm{g}}$ ($\widehat{=} 533\,\mathrm{K}$) while the sample deposited at $0.89\,T_{\mathrm{g}}$

[2]Further details on XPCS contrast may be found in section 3.3.

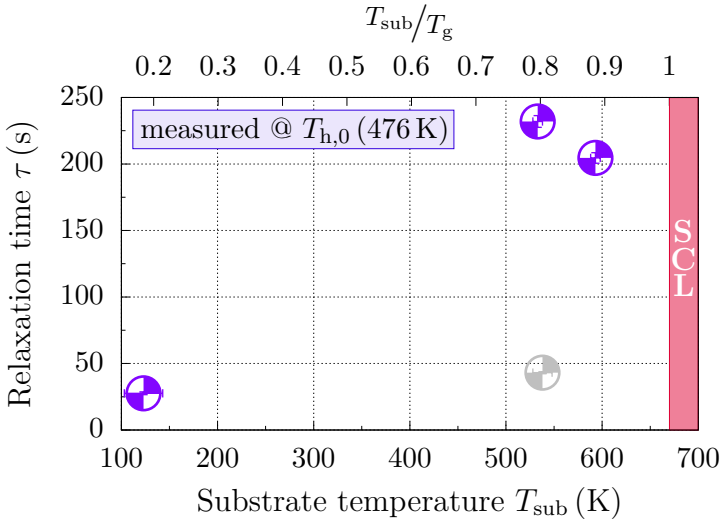

Figure 4.1: Relaxation times τ of vapour deposited CuZr samples, depending on the substrate temperature T_{sub} during deposition. Each sample is an *as produced* sample, hence, it has no thermal history prior the measurement of the relaxation dynamics through XPCS. The red area at temperatures higher than $T_{sub}/T_g = 1$ determines the supercooled liquid regime.

($\widehat{=}$ 593 K) also shows a relatively high relaxation time in comparison to the sample deposited at low substrate temperature (all purple symbols). Similar results have been published for $Zr_{65}Cu_{27.5}Al_{7.5}$ [YLS13]. In the following, this chapter mainly concentrates on sample `Cu50Zr50-VD_015`, which names the one fabricated at $T_{sub} = 0.89\,T_g$. Knowing that the stability of sample `Cu50Zr50-VD_014` (fabricated at $T_{sub} = 0.80\,T_g$) is even higher, all effects described in this chapter should be at least as pronounced as for sample `VD_015`[3].

Notice the grey symbol in figure 4.1, which reveals an underwhelming low relaxation time. This sample represents our very first vapour deposited CuZr MG, when the substrate temperature was not yet sufficiently stable during the deposition process but instead consequently drifted up to around +10 K with regards to the initial T_{sub} during the entire sputtering process. As a result, this sample shows a relaxation time almost within in the same order of magnitude

[3]Note that the given sample names denote their nominal composition. The composition determined is given in sec. 2.5.3. To prevent confusion, from here on, the compositional prefix of the sample name will be omitted in case the sample can be uniquely identified.

as the sample deposited at low T_{sub}. This outcome points out the importance of temperature stability during the deposition process when fabricating an ultrastable metallic glass. However, under all conditions and for all named samples, no signature of crystallisation was found.

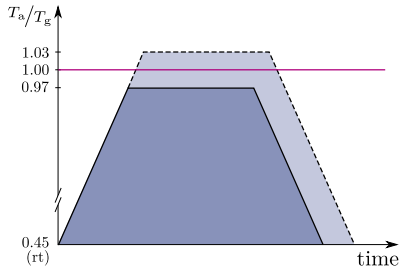

Figure 4.2: Scheme of the annealing procedure.

As shown in figure 2.3, ultrastable glasses are supposed to be located low in the potential energy landscape (PEL). In order to study the effect of that low energetic state and the corresponding characteristics of thermodynamic and kinetic stability, various vapour deposited samples are treated with different annealing protocols after deposition.

A simple annealing procedure is applied prior to the XPCS measurement in order to study its effect on structural dynamics. Therefore samples are annealed under high vacuum (turbo pumped after flushing the chamber with N5 Ar gas, equipped with an "Alphagaz – purifier O_2-free" to remove residual oxygen). After heating up the samples with a ramp rate of $7\,\mathrm{K\,min^{-1}}$ ($\widehat{=}\ 0.11\overline{7}\,\mathrm{K\,s^{-1}}$) from room temperature (rt; approx. $0.45\,T_{\mathrm{g}}$) up to the designated annealing temperature T_a, samples are kept there constantly for 1 min and finally cooled down to room temperature at the same temperature rate. Figure 4.2 depicts a sketch of such an annealing protocol with T_{a} just below or above T_{g}, respectively, while the identifiers of the resulting samples are show in table 4.1, as they will be used as follows.

4.3 Experimental environment

Objective of this section is the environment of the sample during XPCS experiments as well as the samples' preparation.

4.3.1 XPCS at ESRF beamline ID10

XPCS experiments have been performed at the ESRF in Grenoble, France, at beamline ID10 EH2 in the years 2015 to 2017. At that time, the beamline was designed in particular to achieve a (partially) coherent high flux beam of up to 4×10^{10} photons/(s 100 mA) at a photon energy of 8.1 keV, while the beam is collimated to 10 µm × 7 µm (horizontal × vertical). All samples are measured in transmission in wide angle geometry at a wave vector $|\boldsymbol{q}| \approx 27\,\mathrm{nm}^{-1}$. This particular value of q corresponds to the maximum of the static structure profile $I_{\max}(\boldsymbol{q})$, the FSDP, which itself manifests the average interparticle ordering and may be interpreted as an average inter-particle distance within an amorphous sample. The geometry at which the XPCS experiment is performed, determines that the structural dynamics captured represents *local dynamics* – hence, the dynamics of neighbouring configurations.

4.3.2 Sample environment: a versatile homemade furnace

As a versatile sample environment a homemade furnace is used, suitable for multiple requirements. The furnace is built by the "Sample Environment" division[4] and allows to precisely heat and cool the sample under high vacuum as well as under controlled gas atmosphere. Especially the temperature stability lower than $\pm 0.05\,\mathrm{K}$ is critical for XPCS studies on metallic glasses when

[4] A workshop of the ESRF which is specialised on construction and maintenance of individually tailored sample environment solutions, fulfilling the special needs of X-ray research at the ESRF.

identifier	sample type	annealing temperature
$\mathrm{FQ}_{\mathrm{ap}}$	fast quenched	none
$\mathrm{FQ}_{\mathrm{T_g^-}}$	fast quenched	$0.97\,T_{\mathrm{g}}$
$\mathrm{UMG}_{\mathrm{ap}}$	vapour deposited	none
$\mathrm{UMG}_{\mathrm{T_g^-}}$	vapour deposited	$0.97\,T_{\mathrm{g}}$
$\mathrm{UMG}_{\mathrm{T_g^+}}$	vapour deposited	$1.03\,T_{\mathrm{g}}$

Table 4.1: Overview of the studied types of samples, their sample name and their treatment before the XPCS measurement. "ap" referrs to an unprocessed sample, *as-prepared*.

performing measurements at isothermal conditions. Therefore, the heating element is continuously controlled by a PID control loop. The furnace is controllable in a temperature range from ambient temperature up to 1000 °C[5]. Besides providing the samples environment, the furnace itself serves as the sample holder as well. It can be used up to a scattering angle of 50° in transmission geometry and provides clamping for samples with dimensions between several hundred micrometers and 5 mm while a sample thickness down to 5 µm is manageable to be securely fixated.

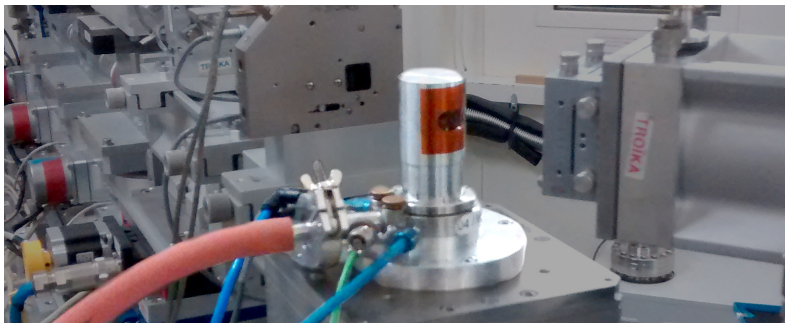

Figure 4.3: Photograph of the used furnace in beamline ID10 EH2 of ESRF, placed on the goniometer. The furnace and its accessories are highlighted. The X-ray beam inclines from the back of the photograph.

Figure 4.3 shows the furnace used at XPCS experiments at beamline ID10 EH2 of the ESRF. It is placed on a x-y-z-stage on the goniometer. The furnace in the center of the photograph is highlighted, whereas the X-ray beam inclines from the background of the image through the small black rectangle in the upper center of the photograph. The diffracted part of the beam is deflected and enters a beam tube on the right hand side of the photograph with the detector at its other end. The sample inside the furnace is connected to a diaphragm vacuum pump, yielding a pressure down to 2 mbar, whereas the X-ray beam enters and exits through films of Kapton (polyimide) windows. The actual elements of the furnace itself and its clamping mechanism is not shown in the photograph, however, technical drawing of the two used furnaces are attached in appendix A.2.

[5]Below approximately 80 °C, temperature control responsiveness and stability reduces and may not perform as required.

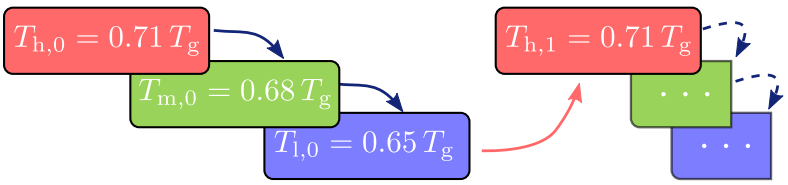

Figure 4.4: Schematic temperature protocol applied along the XPCS measurement. The schemed temperature cycle is applied several cycles.

4.3.3 Measurement protocol: temperature cycling

Data are collected by performing temperature cycles in the glassy state as depicted in figure 4.4. All samples are heated up to the initial high temperature $T_{\mathrm{h},0} = 476\,\mathrm{K}$ ($\widehat{=}\ 0.71\,T_{\mathrm{g}}$). After an initial isothermal XPCS measurement, the temperature is decreased by 20 K to an intermediate (midpoint) value $T_{\mathrm{m},0} = 456\,\mathrm{K}$ ($\widehat{=}\ 0.68\,T_{\mathrm{g}}$) and after that lowered to $T_{\mathrm{l},0} = 436\,\mathrm{K}$ ($\widehat{=}\ 0.65\,T_{\mathrm{g}}$) before being increased to $T_{\mathrm{h},1} \equiv T_{\mathrm{h},0}$. This cycle is repeated several times while the index number i in $T_{\mathrm{h},i}$ corresponds to the iteration of the cycling. Temperature changes are performed with a heating/cooling rate of $0.11\overline{7}\,\mathrm{K\,s^{-1}}$ ($\widehat{=}\ 7\,\mathrm{K\,min^{-1}}$) while each isotherm is kept for ca. 3×10^3 s. Apart from the XPCS measurement itself, some alignment check procedure and a rough structural analysis check ($I(\boldsymbol{q})$) is performed at the beginning of each isotherm in order to confirm steady and consistent conditions at all isotherms.

That scheme of temperature cycling is applied to all samples mentioned earlier, the unannealed ones as well as the annealed ones.

4.4 Full local order decorrelation

Throughout XPCS measurements ultrastable $Cu_{55}Zr_{45}$ shows full decorrelation at temperatures deep in the glassy state, within a range of 0.65 to $0.71\,T_{\mathrm{g}}$, surveyed at a scatting angle corresponding to the first maximum of the static structure factor ($S(\boldsymbol{q})$), the FSDP.

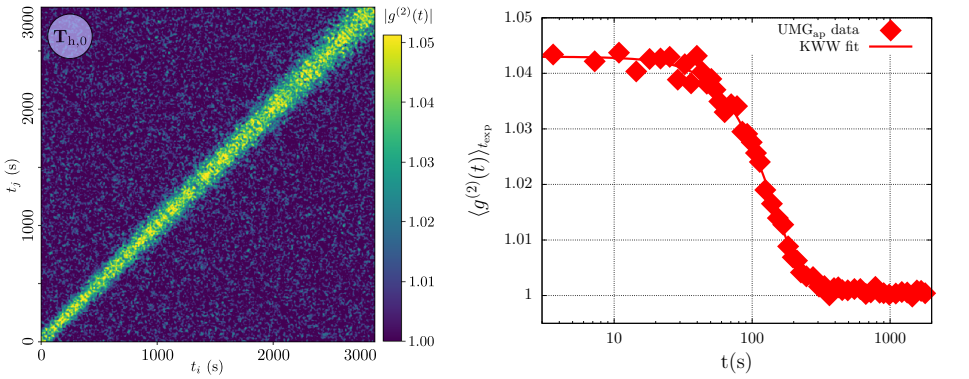

(a) TTCF

(b) t_{exp}-averaged intensity auto-correlation data and KWW fit function.

Figure 4.5: TTCF and time averaged intensity correlation function $\langle g^{(2)}(t)\rangle_{t_{\text{exp}}}$ of as-prepared UMG sample `VD_015a09`, measured at 476 K. The TTCF is plotted using a Gaussian filter applied as stated in this paragraph.

Figure 4.5a shows the Gaussian filtered[6] TTCF of UMG_{ap} measured at $T = 476\,\text{K}$. This representation depicts the evolution of the local structural dynamics of an as-prepared UMG sample made of $Cu_{55}Zr_{45}$ over a time span of $3 \times 10^3\,\text{s}$. While the experimental time t_{exp} evolves along the main diagonal, the width of the bright (yellowish) area along the main diagonal is directly proportional to the local structural relaxation time[7].

To gain quantitative information on the relaxation process, the TTCF is time averaged along the t_{exp}-axis. The resulting second order correlation function $\langle g^{(2)}(t)\rangle_{t_{\text{exp}}}$ is depicted in figure 4.5b. Starting from a plateau, the correlation function decays with a characteristic time τ, which is called the *relaxation time*, and determined by fitting a KWW function to the correlation data. Note the semi-logarithmic scaling.

Both representations of the structural dynamics clearly show a decay of the correlation function to almost unity, hence, a full decorrelation of the intensity correlation within the time span of the shown isothermal measurement can be attributed. By fitting the exponential KWW function [Koh63; WW70]

[6] Using `scipy.ndimage.gaussian_filter` with $\sigma = 1.5$ [Vir+20]. All TTCF in this chapter are plotted with this Gaussian filter settings if not explicitely stated differently.

[7] Please find a detailed introduction to XPCS data processing in chpt. 3.7.

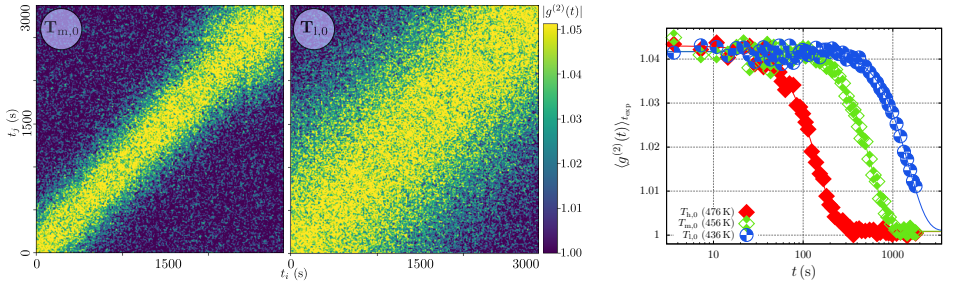

(a) TTCFs at 456 K and 436 K.

(b) Time-averaged correlation functions and KWW fit.

Figure 4.6: TTCF and $g^{(2)}(t)$ of `VD_015a09` as prepared UMG sample, measured at 476 K, 456 K and 436 K. Both TTCFs are scaled equally.

to the t_{exp}-averaged data, an average relaxation time $\bar{\tau} = 205(4)$ s is found at temperature step $T_{h,0}$ (the iteration index $i = 0$ means that the sample has no thermal history, in particular it is heated up the very first time after its preparation). This value of $\bar{\tau}$ is a striking low value (very fast relaxation) as the glass transition temperature is commonly defined at a viscosity of $\eta = 10^{12}$ Pa s, corresponding to a relaxation time of 100 s [Ang95]. Although the relaxation times gathered here through XPCS are close to that value of 100 s, they are – temperature-wise – measured deep in the glassy state. That surprisingly fast collective motion is likely to be a direct consequence of the probed atomic length scale; hence, it may not be representative for the macroscopic picture [Rut+13b; Rut+14; Eve+15; Wan+15; Hec+18]. The observed decorrelation here is associated with rearrangements on a spatial scale of sub-nanometres, precisely $2\pi/q$, while common viewpoints of relaxation dynamics usually regard the entire macroscopic sample. By explicitly picking the value of $\boldsymbol{q}$ such that it corresponds to the maximum of the $S(\boldsymbol{q})$, only *local dynamics* contribute to the above discussed finding.

The shown full decorrelation of the relaxation dynamics can also be observed at lower temperatures; figure 4.6a shows the TTCFs of as-prepared $\mathrm{UMG_{ap}}$, isothermally measured at temperatures T_{exp} equal to 456 K and 436 K (corresponding to 0.68 T_g and 0.65 T_g, respectively), while figure 4.6b shows the intensity auto-correlation function $\langle g^{(2)}(t)\rangle_{t_{exp}}$, averaged over the entire isothermal measurement of each of the three experimental temperatures. At decreased experimental temperatures, the structural dynamics is shifted to-

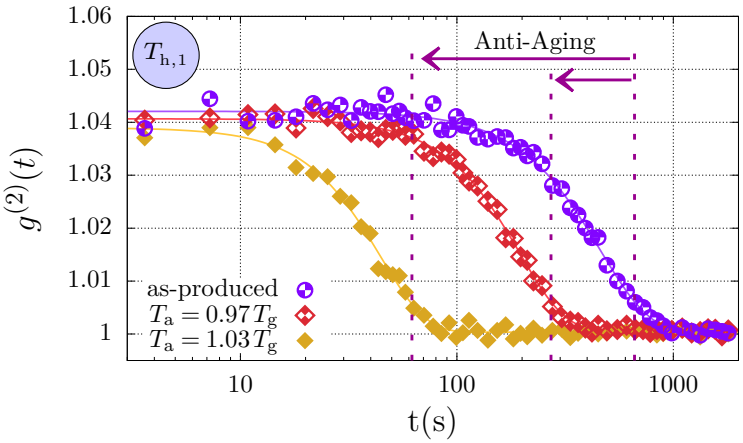

Figure 4.7: Intensity autocorrelation function of UMG_{ap} (open circles), $UMG_{T_g^-}$, and $UMG_{T_g^+}$ (open and closed diamonds, respectively) showing anti-aging behaviour upon annealing. The depicted $g^{(2)}(t)$ functions represent iteration step $T_{h,1}$, hence, they are measured at high temperature ($\widehat{=}\,476\,K$) after the first re-heating to T_h within the temperature protocol outlined in fig. 4.4. The solid lines represent best fits of the KWW expression while the vertical dashed lines indicate the structural relaxation time of the best fit.

wards higher relaxation times, hence, slower relaxation, as can be understood intuitively. A quantitative analysis reveals a slowing down of the relaxation time by more than one order of magnitude upon cooling from $T_{h,0}$ to $T_{l,0}$ which incorporates a temperature shift of 40 K only.

4.5 Anti-Aging in ultrastable $Cu_{55}Zr_{45}$

In order to investigate the extend of ultrastability of the here studied UMGs, two different relaxation conditions are applied. As outlined in section 4.2, fresh samples with no thermal history are annealed just below or above the glass transition temperature (1 min at $(1 \pm 0.03)\,T_g$, respectively). Afterwards, the previously described XPCS measurement protocol is used in order to study the relaxation behaviour (see fig. 4.4).

Figure 4.7 depicts the resulting intensity auto-correlation functions of three samples; UMG_{ap}, $UMG_{T_g^-}$ and $UMG_{T_g^+}$. For an enhanced visibility of the

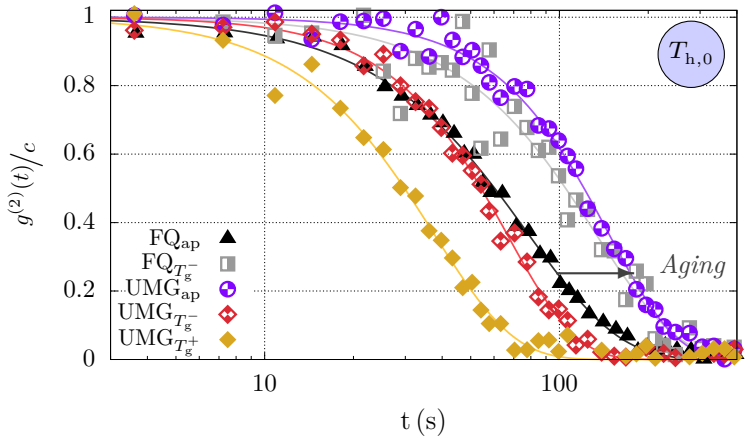

Figure 4.8: Intensity autocorrelation function of UMG and FQ after initial heating $T_{\mathrm{h},0}$, revealing anti-aging behaviour for the UMG sample and usual aging behaviour for the FQ sample respectively. The dark gray colored arrow points out the usual aging behaviour of FQ. For visual guidance, each $g^{(2)}(t)$ is normalised by its contrast c, extracted throughout best fits of the KWW expression. Solid lines represent best fits of the KWW expression.

herein described behaviour, the XPCS measurement at $T_{\mathrm{exp}} = T_{\mathrm{h},1}$, hence, the isothermal at highest temperature, is shown at the second temperature cycle $T_{\bullet,1}$. However, this behaviour sustains all other isotherms during the applied temperature protocol as well[8]. Within these results it is clearly visible that annealing the UMG sample at 0.97 $\mathrm{T_g}$ leads to lower relaxation times (faster dynamics) in comparison to an as-prepared sample, which is remarkable for two reasons:

On one hand, this behaviour is a clear signature of ultrastability at the probed length scale. As usually annealing leads to a more relaxed state of the glass [Kov64; Xue+16; Kea+07; RDD03; Wan+15], that does not apply to UMG, confirming its enhanced stability characteristics due to the preparation method, which is obviously destroyed upon annealing.

Furthermore, the decreased relaxation time of UMGs upon annealing manifests the opposite behaviour as usually observed in (metallic) glasses: An-

[8] See also figure 4.8 showing measurements at $T_{\mathrm{exp}} = T_{\mathrm{h},0}$ or a summary of all relaxation times in figure 4.16, extracted from the captured intensity correlation functions at all high temperatures $T_{\mathrm{h},i}$. The effect also sustains lower experimental temperatures $T_{\mathrm{m},i}$ and $T_{\mathrm{l},i}$.

nealing does *not* lead to a more relaxed state with higher relaxation times but contrarily leads to faster relaxations. This is why the name "*anti-aging*" is attributed to this behaviour [Lüt+18]. The statement can be made clearer by directing the attention on figure 4.8. The figure shows similar $g^{(2)}(t)$ data as figure 4.7 (in this case at the initial isotherm $T_{\mathrm{h},0}$ of the applied temperature protocol). Additionally to the UMG data, data of FQ samples are included in the figure; full triangles depict the as-produced FQ sample ($\mathrm{FQ_{ap}}$) whereas open squares depict the FQ sample annealed at $T_{\mathrm{a}} = 0.97\,\mathrm{T_g}$ ($\mathrm{FQ}_{T_{\mathrm{g}}^-}$). While UMG shows its peculiar anti-aging behaviour, the FQ sample shows its usual and well known aging behaviour [Lun+05; Wan12; LGB15; Ma+18; Gal+18], resulting in decelerated relaxation dynamics, hence, higher relaxation times. The usual aging behaviour is illustrated throughout a dark gray arrow in figure 4.8, emphasising a shift of the relaxation dynamics towards longer time scales. To be able to compare the data, they are normalised by their contrast c.

The absolute values of the determined relaxation times τ are also remarkable. The below-T_{g} annealed FQ glass ($\mathrm{FQ_{ap}}$) shows similar, yet slightly faster averaged relaxation dynamics than $\mathrm{UMG_{ap}}$. However, this could be understood as follows. While, in complement to the here presented findings, macroscopic studies of UMGs show well decelerated relaxation dynamics compared to their fast quenched counterparts [LGB15; Rie+19], this deviation from the outcomes of macroscopic studies can be understood in terms of the unique capability of XPCS to probe *local* relaxation dynamics and with that underlines the importance and the prospect of that XPCS method to augment the understanding of glass dynamics.

The unique anti-aging behaviour of UMGs can be better understood within the framework of the potential energy landscape. Figure 4.9 reports the relaxation times τ measured at $T_{\mathrm{h},0}$ for the differently annealed UMG samples (open diamonds), together with the FQ samples (filled triangles). For conventionally produced FQ MGs, the known effect of *aging* can be confirmed [Kea+07; SEP13; PS13; Kea+08; Daw+09]: annealing leads to an increase of the relaxation time. Within the PEL framework, that trend can be understood such that FQ MGs are known to be located in a high energy basin. Thus, they

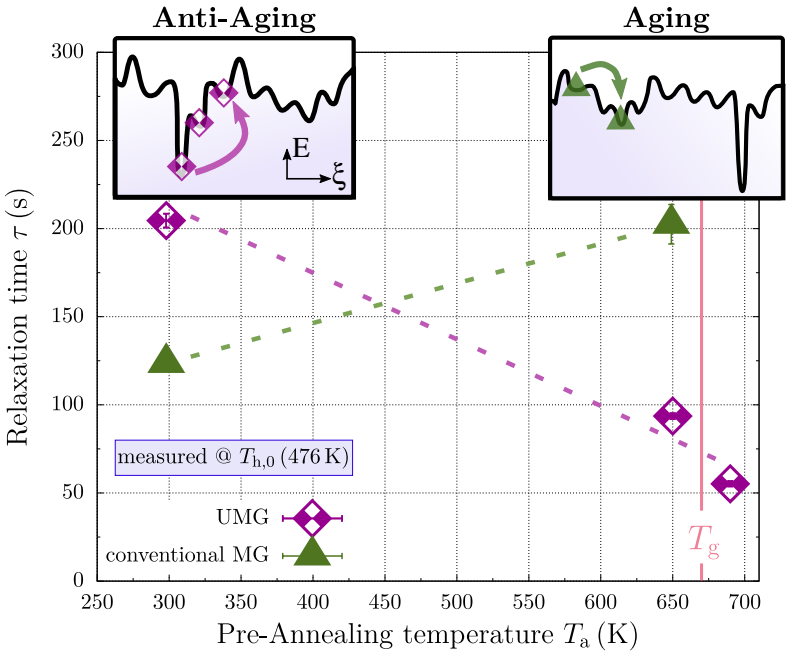

Figure 4.9: Effect of the pre-annealing T_a on τ for conventional CuZr MG (filled triangles) and UMG (open diamonds), measured at $T_{h,0}$ ($\widehat{=}$476 K). The data at 298 K correspond to as-prepared samples. The vertical line depicts T_g of the conventional MG. The effect of anti-aging of the UMG sample is indicated by the dependence on T_a, which evolves inverse to conventional aging. Dashed lines are a guide to the eye. The two insets depict a scheme in which the data are interpreted in terms of the potential energy landscape. Error bars are within the symbol size.

have a large capacity to relax down to a lower basin, for instance by annealing. Throughout the thermal energy introduced they overcome the barrier of their basin and change configuration to a different one, corresponding to a different basin located lower in the PEL. This thermally induced aging process is depicted in the sketch on the top right of figure 4.9 entitled "Aging". As stated earlier in this section, the behaviour of UMG is rather the opposite. UMGs are supposed to be trapped in a very low basin within the PEL already by their fabrication process [Yu+13; PS13; Ber+17], hence, they should show high relaxation times already upon fabrication, accordingly. Here can be demonstrated that upon annealing close to T_g[9], the relaxation times *de-*

[9]The reference T_g is the glass transition temperature of the as-produced fast quenched sample FQ_{ap} and with that it is in especially not the glass transition temperature of

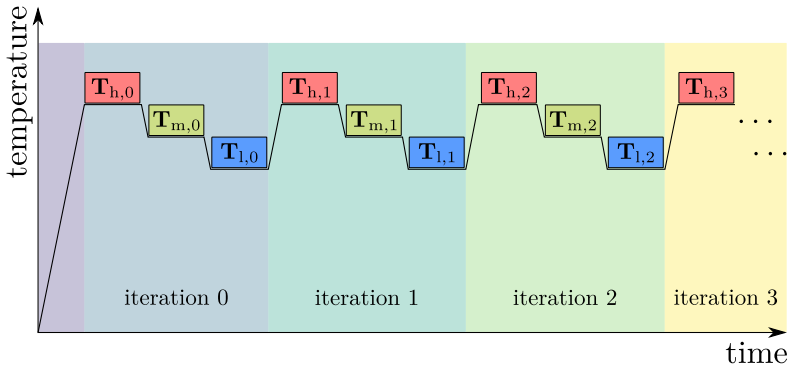

Figure 4.10: Schematic temperature protocol for the study of isothermal aging throughout XPCS analysis. The relaxation dynamics is captured at three different temperatures – *high*, *midpoint* and *low* – while the XPCS measurements are performed along with each isotherm. Several iterations i of the outlined three temperature steps $T_{\bullet,i}$ are performed consecutively as highlighted by the colored background.

crease, and with anomaly, they behave contrarily to conventionally produced MGs. From that inverted behaviour we conclude that the thermal energy introduced into the system boosts it to a basin located higher in the PEL, leading to the unique anti-aging effect as illustrated in the sketch at the top left of figure 4.9 entitled "Anti-Aging". "Anti-Aging" is not equal to "rejuvenation" since the UMG never saw a "juvenile" high energy state due to the preparation conditions. Hence, it might be convincing to claim microscopic proof that the initial configuration of UMG corresponds to a state deep in the PEL.

As will be shown in the following sections, this behaviour sustains throughout the applied measurement protocol of various temperatures and multiple temperature cycles (see fig. 4.4), which means that the enhanced stability and therewith the anti-aging properties are somehow preserved throughout the thermal treatment by the temperature protocol.

the UMG sample. The later one has a higher T_g. However, for simplicity reasons, the reference T_g is the one of the FQ sample.

4.6 Indication of isothermal aging in ultrastable $Cu_{55}Zr_{45}$

While the previous section sheds light on ultrastability and on the influence of thermal treatment on UMG, this section puts its focus on spontaneous relaxation processes of UMG during isothermal conditions.

A measurement protocol as depicted in figure 4.10 is used for an XPCS study of isothermal relaxation behaviour of UMG and FQ CuZr samples. In a recurring manner XPCS measurements in a T-window of 476 K to 456 K ($\widehat{=}$ 0.71 T_g to 0.65 T_g) are conducted, starting from high temperature. Each isotherm is held for ca. 50 min while T-stability of ± 0.04 K maximum deviation from set point (and ± 0.01 K average deviation) is maintained. After each isotherm, T is lowered towards the next isotherm with a cooling rate of 7 K min^{-1} ($\widehat{\approx}$0.12 K s^{-1}), while after the third isotherm T is raised to the value of the initial $T_{h,}$ applying the same T-rate as for cooling. With that the T-cycle starts over again. The entire T-cycle is applied two to five times, depending on the studied sample.

The resulting TTCFs for UMG_{ap} are depicted in figure 4.12 where the evolution of the intensity correlation is plotted over 3×10^3 s for each high-temperature isotherm $T_{h,i}$ only. During the first two temperature cycles, a broadening of the brighter (yellowish) area along with the main diagonal can be identified, presenting a spontaneous increase of the average relaxation time at constant temperature – this behaviour may be classified *isothermal aging* as it occurs under isothermal conditions. With further T-cycling that kind of spontaneous aging vanishes, transitioning to stationary dynamics (no further broadening). At lower temperatures, $T_{m,i}$ and $T_{l,i}$, no isothermal aging can be identified. However, at the first isotherm at mid temperature $T_{m,0}$ a slight onset of intermittent aging can be seen towards the end of the

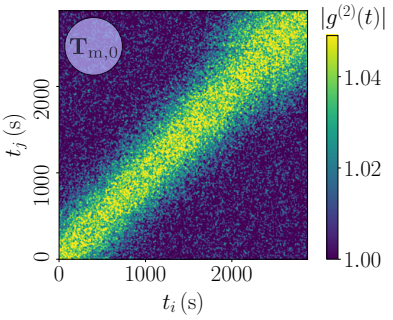

Figure 4.11: TTCF of UMG_{ap} at initial midpoint temperature $T_{m,0}$.

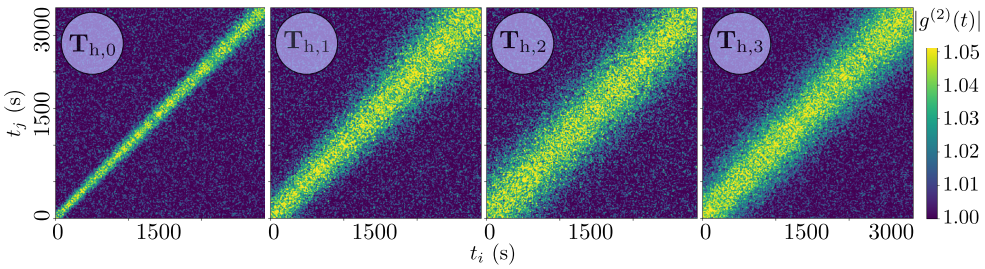

Figure 4.12: TTCF of $\mathrm{UMG}_{\mathrm{ap}}$ sample `VD_015a09` at high temperature isotherms throughout the first four iterations of T-cycling. Scaling is identical for all figures.

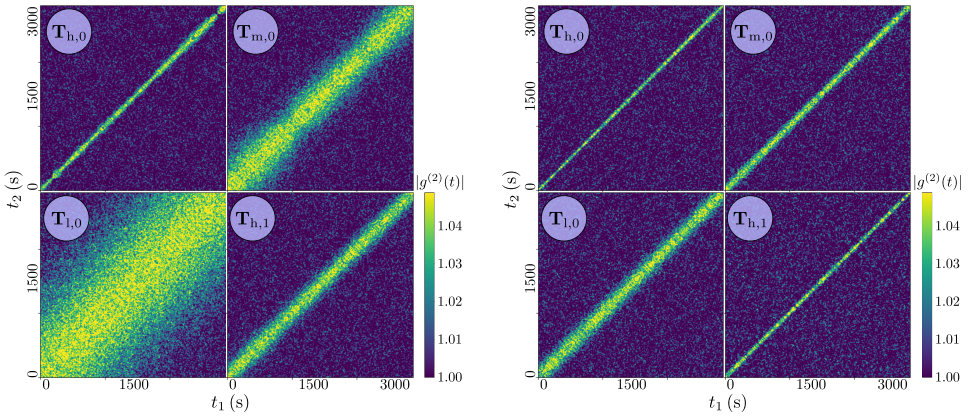

(a) $\mathrm{UMG}_{T_{\mathrm{g}}^-}$ **(b)** $\mathrm{UMG}_{T_{\mathrm{g}}^+}$

Figure 4.13: TTCF of $\mathrm{UMG}_{T_{\mathrm{g}}^-}$ and $\mathrm{UMG}_{T_{\mathrm{g}}^+}$ samples `VD_015a10` and `VD_015a11` within each first T-cycle and the following high temperature measurement of the second iteration, respectively. Scaling is identical for all figures.

measurement at around 2300 s (see fig. 4.11). In chapter 5, XPCS measurements with much more pronounced intermittent aging events are shown, displaying peculiar "butterfly" behaviour.

The situation is different for $\mathrm{UMG}_{T_{\mathrm{g}}^-}$ and $\mathrm{UMG}_{T_{\mathrm{g}}^+}$ which are annealed below or above T_{g}, respectively. Both panels of figure 4.13 show the evolution of relaxation dynamics during the initial T-cycle $T_{\bullet,0}$ and the consecutive high T isotherm $T_{\mathrm{h},1}$, respectively. During all measurements, exclusively stationary dynamics is observed; it is, in particular, the absence of isothermal aging right from the beginning of T-cycling, that is found. The slight in-

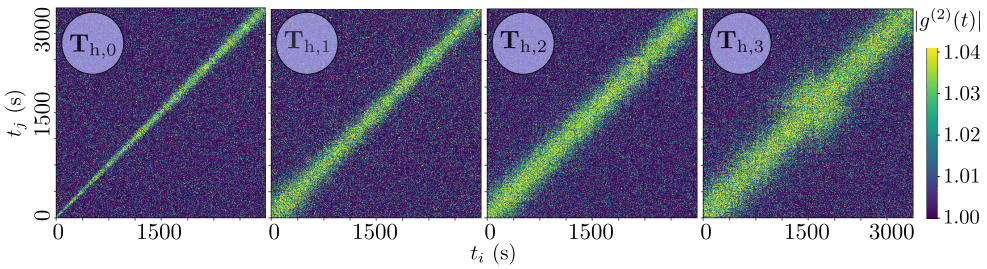

Figure 4.14: TTCF of $\mathrm{FQ}_{\mathrm{ap}}$ sample `FQ_001t` at high temperature isotherms throughout the first four iterations of T-cycling. Scaling is identical for all figures.

crease of the relaxation time under isothermal conditions, present in $\mathrm{UMG}_{\mathrm{ap}}$, can likely be understood as the presence of some residual stresses in the as-prepared material. That is why it is not observed in annealed UMG samples.

Similar to $\mathrm{UMG}_{\mathrm{ap}}$, $\mathrm{FQ}_{\mathrm{ap}}$ shows spontaneous aging throughout a broadening of the area of high correlation along with the main diagonal at the initial temperature step $T_{\mathrm{h},0}$ under isothermal conditions, depicted in figure 4.14. However, that behaviour already vanishes with iteration $i = 1$ of the T-cycling, although the sample shows an onset of accelerated dynamics just from the beginning of the measurement at $T_{\mathrm{h},1}$ as the main diagonals width shrinks within the first 750 s and becomes stationary afterwards. During the fourth high-T isotherms the as-prepared FQ sample shows an event of intermittent aging at $T_{\mathrm{h},3}$. This kind of "event" is also described in different materials and likely to appear in later iterations of T-cycling or other manners of temperature treatment [Eve+15; RPE17].

4.7 History dependent dynamics and augmented aging

The term "history dependent dynamics" can be understood such that the structural relaxation time τ changes after applying a certain temperature protocol just as sketched in figure 4.4, where the sample is reheated to an initial temperature value after being exposed to different temperatures. In

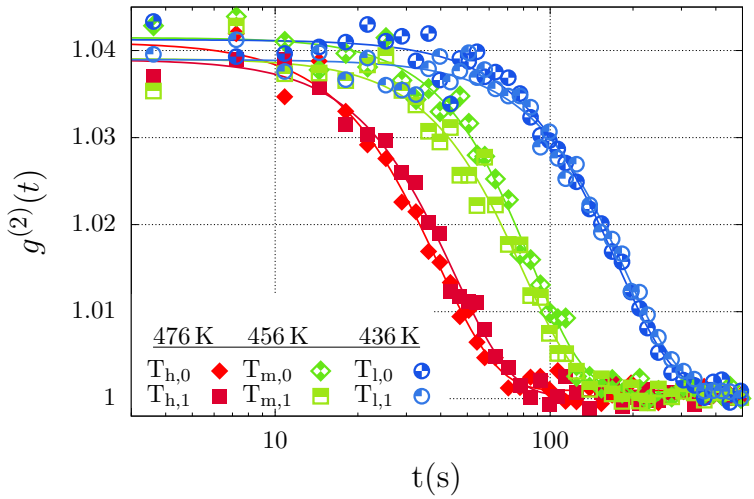

Figure 4.15: Intensity autocorrelation function $g^{(2)}(t)$ of $\mathrm{UMG}_{T_g^+}$ (sample `VD_015a11`) at all temperatures of the first two T-cycles displaying no history dependence or augmented aging at all.

the described protocol, history dependent dynamics reveal upon reheating from $T_{\mathrm{l},0}$ to $T_{\mathrm{h},1}$ (while $T_{\mathrm{h},1} \equiv T_{\mathrm{h},0}$). If in such a situation the relaxation time $\tau(T_{\mathrm{h},1})$ is higher than $\tau(T_{\mathrm{h},0})$, aging based on the samples' thermal history has occurred.

In the herewith presented data, thanks to XPCS, it is possible to distinguish between different types of history dependent dynamics. As stated in the previous section 4.6, aging can occur under constant temperature conditions called *isothermal aging*. However, if the rate of isothermal aging of $T_{\mathrm{h},i}$ is not sufficient to extrapolate to an (increased) value of τ after reheating to a temperature $T_{\mathrm{h},i+1}$, the record of the temperature protocol itself is likely to have influenced the relaxation dynamics. For this extrapolation the duration of an entire T-cycle ($T_{\mathrm{h},0} \rightarrow \ldots \rightarrow \ldots \rightarrow T_{\mathrm{h},1}$) is regarded. In other words, if the amount of an isothermal aging rate is insufficient to extrapolate from a $\tau(T_{\mathrm{h,i}})$ to an subsequent $\tau(T_{\mathrm{h,i+1}})$ along with the time between both XPCS measurements, the history of the temperature protocol itself affects the relaxation dynamics. This behaviour will from here on be called *augmented aging*, and denotes a memory effect [YL03; BCL00; BCL02; SB19].

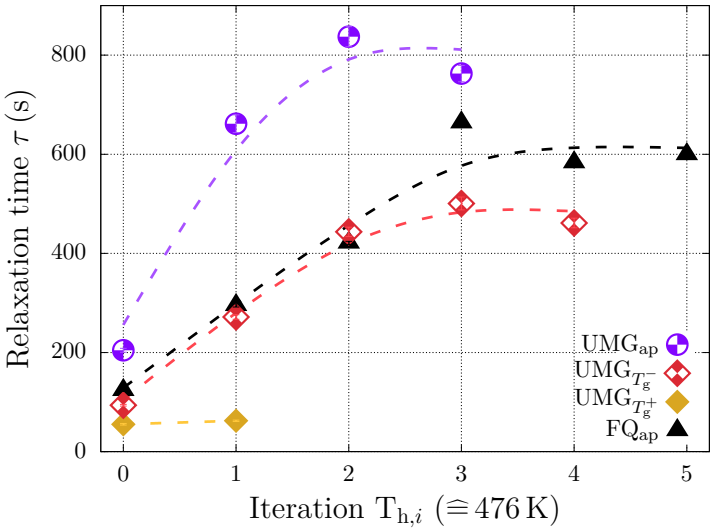

Figure 4.16: Evolution of the structural relaxation time τ of UMG$_{ap}$ (open circles), pre-annealed UMGs (open and closed diamonds, respectively), and conventionally produced MG (triangles) as a function of high-temperature iterations $T_{h,i}$ applying the temperature protocol as outlined in fig. 4.4. Dashed lines are a guide to the eye. Error bars are within the symbol size.

Both samples, UMG$_{ap}$ as well as UMG$_{T_g^-}$, show augmented aging as an extrapolation of the isothermal aging rate along with the time between the first two T-cycles is not sufficient to match τ at the beginning of isotherm $T_{h,1}$. However, this effect does not occur in UMG$_{T_g^+}$ as can be seen in the representation of $g^{(2)}(t)$ in figure 4.15. The figure shows the intensity correlation function over time in semi-logarithmic scaling of two full iterations throughout the T protocol at all applied temperatures. Under all conditions we find full decorrelation of $g^{(2)}(t)$ just as in the other UMG samples. Interestingly at all temperatures, the correlation functions superpose each other. Hence, within six XPCS measurements over more than six hours of time, no history dependent aging at all can be seen – neither isothermal nor augmented aging. From that it may be concluded that all relaxation dynamics is fully reversible in UMG$_{T_g^+}$. With that, no further iterations of T-cycling are captured.

The evolution of a structural relaxation time over all iterations for all UMG and the as-prepared FQ samples are merged in figure 4.16, regarded at one

temperature value ($T_{\mathrm{h},i}$). The evolution of τ is similar at lower temperatures $T_{\mathrm{m},i}$ and $T_{\mathrm{l},i}$, however not shown here. One finds that the relaxation time of $\mathrm{UMG_{ap}}$ is the highest at all iterations (violet open circles, slowest process), hence, $\mathrm{UMG_{ap}}$ is the utmost stable sample studied at all iterations. After two or three iterations a metastable state seems to be reached for $\mathrm{UMG_{ap}}$ from which the relaxation time at T_{h} does not evolve any further. The annealed UMG and the FQ samples behave in the same manner, just the number of iterations to reach that metastable state varies. In particular, history dependent or temperature assisted driven aging seems not to let any sample reach the relatively high relaxation times of $\mathrm{UMG_{ap}}$ at any iteration as all samples seem to converge towards their own metastable plateau. This highlights the outstanding stability of as-prepared ultrastable metallic glass at the probed length scale of local dynamics and is a clear signature of an improved stability obtained by the preparation throughout physical vapour deposition with low deposition rate and T_{sub} near to T_{g}. The effect of anti-aging becomes apparent when comparing the relaxation times of all UMG samples at a certain iteration i: the decrease of the relaxation time from $\mathrm{UMG_{ap}}$ to $\mathrm{UMG}_{T_{\mathrm{g}}^{-}}$ and $\mathrm{UMG}_{T_{\mathrm{g}}^{+}}$ consecutively signals the effect of anti-aging.

4.8 KWW shape parameter

In section 3.7 the temporal intensity correlation function $g^{(2)}(\boldsymbol{q}, t)$ and the KWW function are introduced. In this section attention is drawn on the so called KWW exponent or *shape parameter* β, one of the fit parameters of the KWW function, which may provide information on the nature of the collective particle motion in the glass.

Figure 4.17 superposes all $g^{(2)}(t)$ functions of the XPCS measurements of the previously described $\mathrm{UMG_{ap}}$, $\mathrm{UMG}_{T_{\mathrm{g}}^{-}}$, $\mathrm{UMG}_{T_{\mathrm{g}}^{+}}$ and $\mathrm{FQ_{ap}}$ samples at all captured isotherms. In order to compare the shape of the decays, the data are normalised on the time axis by the relaxation time τ which is obtained by fitting a KWW function to each dataset. The inset (b) shows the evolution of the shape parameter β, a parameter of the KWW fit function extracted

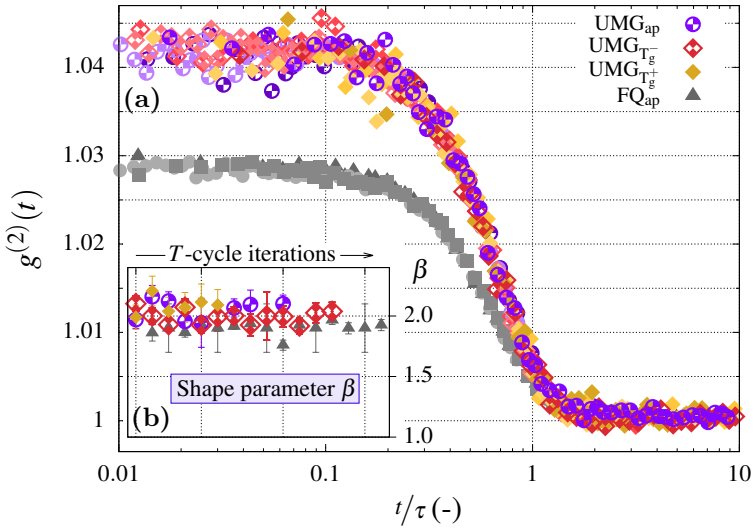

Figure 4.17: (a) Superposition of all $g^{(2)}(t)$ functions of UMG and FQ samples, with the time axis normalised by the relaxation time τ. (b) Inset of the extracted shape parameter throughout fitting a KWW function to $g^{(2)}(t)$ over all iterations of T-cycling. Error bars are visible when larger that the symbol size.

from full averaging over each entire TTCF. Despite the observed ultrastability of UMG$_{ap}$, β remains constant at all probed temperatures and for all samples. Furthermore, in all cases the curves decay in a highly compressed manner $\beta = 2.0(2)$, similarly to what is reported for other metallic and non-metallic glassy systems [Eve+15; Rut+13a; Bou+17; Gok+16; Hec+18]. This is astonishing as compressed correlation functions are often associated with internal stresses [BP01; CB17] and ultrastability is usually related to low values of residual stress. In the here described data, β is not only very large but completely unaffected by annealing, sample preparation and sample treatment. This means that elastic frustrations – responsible for stress dominated dynamics – are not involved in the process leading to ultrastability, and the stresses related to a high shape parameter are likely intrinsic to the out-of-equilibrium nature of a glassy state in metallic systems, also supported by recent findings of Hechler et al. [Hec+18].

4.9 Discussion and Outlook

By comparing the relaxation times of UMGs and FQs investigated by macroscopic studies with studies by XPCS, it can be concluded that the qualitative results support each other [DLS20], even though compositions are slightly different (UMG: $Cu_{55}Zr_{45}$, FQ: $Cu_{51}Zr_{49}$; details in sec. 2.5.3). However, the quantitative results from the here shown XPCS data are remarkable in a way, such this UMGs samples show lower absolute relaxation times as expected, although the ultrastable character can be confirmed by this technique. Apparently relaxation dynamics of MGs quantitatively differs between the macroscopic and local level, due to the highly different length scales probed. From that finding, one may conclude that the insight which XPCS gives into the relaxation dynamics of metallic glasses has an enormous value and hence, importance in order to gain understanding of underlying phenomena. To date, the findings XPCS can unveil are not covered by any other technique. Higher coherent flux resulting from recently planed or performed upgrade programs of some of the currently most powerful synchrotrons, together with the deployment of the state-of-the-art detectors will enable an extension of the probed time scale towards shorter times already in the 2020s [And+15; Aga+19]. These will permit to investigate relaxation dynamics at higher temperatures in the glassy regime, closer to T_g, whereas experiments of the here presented studies are limited to approximately $0.75\,T_g$ ($\approxeq 500\,\mathrm{K}$; in the herein studied material class). Also new methods like a "four-point" correlation function $\chi^{(4)}$ (or $G^{(4)}$) analysis unveiling the cross correlation function of local dynamics, already established in studies of colloids and granular material [DMB05; Key+07; Dur+09], should become applicable to metallic systems with the new generation of X-ray sources.

From the determined values of τ for a freshly prepared UMG sample (UMG_{ap}) it can be concluded that the low energy state upon the particular fabrication process of a UMG may not be undercut by usual paths of relaxation processes such as annealing or aging on practical time scales. Experimental studies by Wang et al. indeed show that it takes decades to reach such a low energy state by means of conventional aging [Zha+22].

Besides, the findings in this chapter demonstrate the presence of two different regimes of dynamics: an aging regime and a stationary regime (see fig. 4.16). The dependence of the relaxation time τ on the iterations of an applied temperature protocol may be associated with the implications of temperature cycling on aging, and is well known as the Debye-Grüneisen effect [LSS07; Kah+09; SB19]. After a few iterations through the T-cycling $\mathrm{UMG_{ap}}$, $\mathrm{UMG}_{T_\mathrm{g}^-}$ and $\mathrm{FQ_{ap}}$ are trapped in a metastable state where the dynamics is rather localised before eventually, the dynamics becomes stationary [FIE15]. Earlier XPCS studies on conventional MGs such as [RPE17; Rut+13a] already reported the existence of such two regimes, while recent studies by Gallino et al. report on stationary dynamics interconnected by abrupt aging processes. Therein the aging regime is linked to density changes whereas the stationary regime is associated with an increase of the correlation length of the medium range ordering [Gal+18].

Lowest relaxation times and the absence of any indications of memory effects of the UMG sample annealed above T_g ($\mathrm{UMG}_{T_\mathrm{g}^+}$) suggest a metastable state. Upon entering equilibrium (during annealing) a glass' history is erased and the sample now shows memory effects. The captured dynamics denotes a state of a high energy meta-basin in the PEL as no relaxation towards a lower energy state is observed. Kahl et al. draw similar conclusions from their study on changes of the shear modulus in bulk $\mathrm{Pd_{40.5}Ni_{40.6}P_{18.9}}$ MG upon multiple temperature cycling below and slightly above T_g [Kah+09; SB19]. Yet, it is important to emphasise that the stationary regime, where τ is independent on further T cycling, does not correspond to an equilibrium state.

The occurrence of augmented aging in $\mathrm{UMG}_{T_\mathrm{g}^-}$ might be based on events of intermittent aging. As events of intermittent aging are also observed to happen within short periods of time, they are likely to be missed. Especially during temperature change or within the first minutes of an isotherm (typically around 5 min to 10 min), when beamline and sample alignment are routinely checked, no XPCS measurement can be performed. Further manifestations of intermittent aging are reported and discussed in chapter 5.

Chapter 5

Statistical analysis of structural dynamics

Contents

5.1 Introduction

Avalanche-like dynamics is receiving growing attention in the glass and disordered systems community. It has demonstrated to be an important concept to describe the behaviour of plasticity in solid materials [SDM01; DBU09; KLP10; SJ21]. Moreover, avalanche dynamics is known to occur in many different systems, including Barkhausen noise in magnetic materials [CM91; Zap+98], martensitic phase transitions [Viv+94; San+11],

sand [SJ21], snow [FLG04], solar flares[LH91], stock market [Gab+03] or in earthquakes [GR54; Bar+13]. Despite their complexity of effects and the differences between those systems, they commonly share a power-law distribution of avalanche size $P(s) \propto s^{-\kappa}$, with κ being the critical exponent. The emergence of a power-law distribution expresses the lack of a characteristic length scale and indicates the system to exhibit self-organised criticality [BTW87].

In this chapter, indications of avalanche-like dynamics are studied in relaxation dynamics data of non-directionally excited MGs. Therefore, XPCS experiments are conducted, from which data of the temporal evolution of the structural relaxation time τ is analysed by statistical means. In this way, an investigation of the occurrence of length, respectively time, scale invariant characteristics can be achieved.

5.2 New analysis approach

Goal The identification of avalanche-like dynamics is tricky as the fingerprint of avalanche-like dynamics is embedded within the zoo of all differently behaving rearrangement dynamics. For this reason, statistical methods are used in order to identify the presence of avalanche-like dynamics which manifests through power-law distributed statistics.

The following sections outline the computational workflow developed within this thesis, in order to mine time-resolved relaxation time data $\tau(t_{\mathrm{exp}})$, which builds the data basis for the aforementioned statistical analysis of the relaxation time τ.

5.2.1 Capture XPCS data

According to the procedure described in section 3.6, a series of speckle patterns is recorded. The individual images carry information on the microscopical particle arrangement, while the whole speckle pattern "movie" holds information on the dynamics of the studied sample. Consecutively, the series of speckle patterns is subject of intense numerical analysis.

5.2.2 Calculate TTCF

Secondly, the well established numerical calculation of a two-time correlation function is performed with the previously captured XPCS data. Details of the entire process are described in section 3.7. The well established and automated numerical analysis ends here. For deeper numerical analysis it is necessary to inspect the TTCF image visually, identify regions of interest (ROIs) and subsequently calculate $g^{(2)}(t)$ for each explicit ROI or compare different ROIs within one TTCF.

5.2.3 Apply rolling-window KWW fit

For quantitative analysis of a TTCF, a *rolling-window* sequential analysis method is developed within this thesis. This method aims to quantify the evolution of the relaxation time along with the experimental time with high resolution. Figure 5.1 shows the result as a white contour, drawn over the original TTCF, where the KWW-fit function decays by $1/e^2$. A rolling window along the ACS direction allows fine tuning of the required extend of arithmetical averaging, which is necessary to deal with noisy data. In most cases, when TTCFs are shown, a Gaussian filter is applied to smooth that noise. Figure 5.2 shows a section of a raw TTCF (a) and one with a Gaussian filter applied (b) for comparison. While applying the KWW-fit function (see eq. 3.14), some parameters such as baseline parameter A, contrast c, KWW-exponent β or relaxation time τ may be fixed to deal with a low signal-to-noise ratio. As a result, the evolution of the four parameters along with the experimental time t_{exp}, in the following simply t, is obtained. In particular $\tau(t)$ is of great interest as it depicts quantitative information on temporal changes of the relaxation dynamics, allowing to quantify relaxation or aging processes.

5.2.4 Identify events of interest

Avalanches events may be indicated through an abrupt drop of the relaxation time τ, originated through stick-slip behaviour of microscopical rearrange-

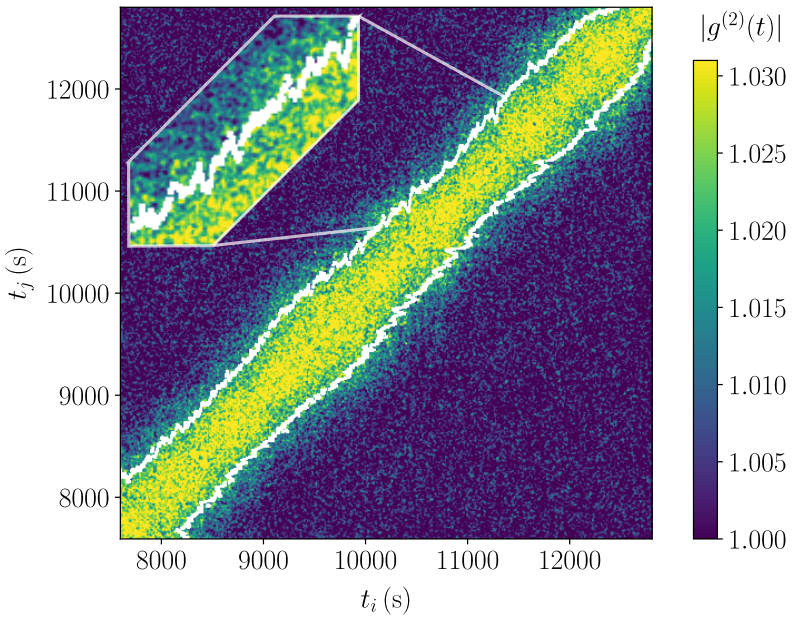

Figure 5.1: Exemplary section of a TTCF of a VD MG measured at 576 K. White contour (discontinuous) represents the results for relaxation time τ from sequential best fit of the KWW function. The inset on the upper left shows a magnification of the marked area in order to improve visibility of the fine structure of the white contour.

ments. Figure 5.4 schematically shows the identification of relaxation time drops $\Delta\tau$ in fictional data. Blue crosses indicate the t-evolution of relaxation times τ, determined by means of sequential best fits of the KWW function to a rolling window in ACS direction along a TTCF. Black horizontal lines mark local minima and maxima of τ and green vertical arrows show the amount of relaxation time change $\Delta\tau$ due to a drop of relaxation time.

5.2.5 Calculate probability statistics of relaxation time drops $P(|\Delta\tau|)$

Finally a statistical analysis of the drops of relaxation time $\Delta\tau$ is performed. A certain representation of the histogram gives insight to the underlying statistics. Therefore the histogram is plotted in a $\log-\log$-graph while the binning is logarithmic as well to keep the bins equidistant on the abscissae.

To prevent overrepresentation of data at small t (large bins), the probability $P(|\Delta\tau|)$ is rescaled by the bin width w_{BIN_i}. To identify power-law behaviour, finally, a linear regression is performed on the histogram data or on sections of it [CSN09].

5.3 Method implementation

In order to understand the implementation of the workflow outlined in section 5.2, it is essential to identify the current standard of data processing. Time resolved XPCS data are usually analysed by means of a multi-tau software correlator, implemented within `waxpcs.py`, which is provided by ESRF's beamline ID10[1,2]. That code makes use of a multi-tau droplet algorithm [CCM12] and creates a visual as well as a machine readable TTCF file as its output, comprising all correlations of all captured speckle patterns with each other. Quantitative analysis can be either made by averaging over the entire TTCF, which voids the advantage of the TTCF itself, or by calculating smaller TTCFs based on sub-ranges of the entire set of captured speckle patterns. Although it adds quantitative temporal resolution along the experimental time axis t of the TTCF, the second method carries disadvantages based on averaging along the CCS direction. These disadvantages are discussed in detail in section 3.7.

Why averaging is necessary in the first place can be understood from figure 5.2. The figure shows two panels of the same TTCFs section of the same data. The upper panel a) shows the illustration of the actual data of the TTCF. Each pixel carries the value of the intensity correlation function $g^{(2)}(t)$ encoded through its colour, while bright (yellowish) colour represents a high and dark (blueish) colour a low value of $g^{(2)}(t)$. Obviously, the distribution looks very noisy as no continuous gradient orthogonal to the main diagonal

[1] Details according to the scientific environment of beamline ID10 at the ESRF can be found under the following address https://www.esrf.fr/UsersAndScience/Experiments/CBS/ID10 (retrieved at 2023-03-15T12:11:05+01:00).

[2] A description of beamline ID10 at the ESRF, in especially on data acquisition and data processing can be found under the following address https://www.esrf.fr/home/UsersAndScience/Experiments/CBS/ID10/ID10EH2/BeamlineDescription.html (retrieved at 2023-03-15T12:12:33+01:00).

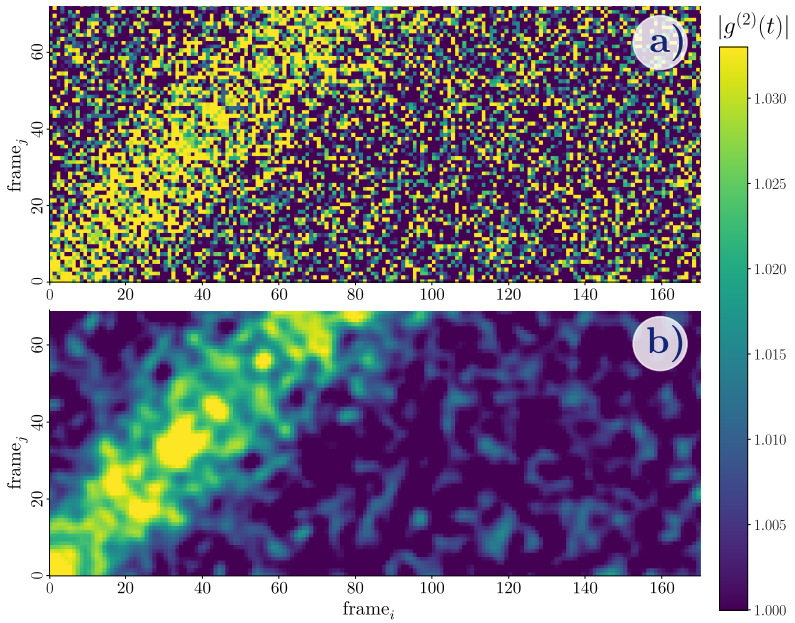

Figure 5.2: Two panels of the same section of the first 170×72 frames, taken from the same dataset as depicted in fig. 5.1. Top panel (a) shows the actually calculated correlation function (as a 2-dim matrix) while the bottom panel (b) shows the typical illustration with a Gaussian filter ($\sigma = 1.5$) applied to the actual correlation function from panel (a).

can be found. For that reason, an analysis of the evolution of the highly correlated area along the main diagonal can not be performed readily – the areas contour line cannot be sketched easily. To facilitate the understanding of the predominant relaxation behaviour, all illustrated TTCFs are usually shown Gaussian filtered, typically with $\sigma \in [1, 1.5]$. This is done by applying the `gaussian_filter` function to the TTCF data, provided by the `python` library `scipy` [Vir+20], before displaying them. Hence, averaging over multiple frames along the experimental time axis is necessary. However, the default software for data processing were not capable of averaging the TTCF data in a way that an evolution of the structural relaxation along the experimental time axis was possible at the time of data acquisition.

To overcome that limitation, a new data processing method was developed, called `trcfit.py`[3]. This software allows to define how many frames (of the

[3]The term "trc" stands for "time resolved correlation" and is used equivalent to the term TTCF.

TTCF) should be arithmetically averaged, the according averaging parameter is referred to as `TTCF-avg`. That averaging is applied along with the ACS axis in order to keep the corresponding reference time, to which the averaging should be performed. Slices of parallels to the main diagonal of the TTCF are selected and sequentially gathered orthogonally to the main diagonal. As a result, the average correlation function of each consecutive slice represents the evolution of $\langle g^{(2)}(t)\rangle_t$ with respect to one distinct reference frame frame_n at time t_i. In the next step, the rolling-window method increments n, so that the average correlation functions $\langle g^{(2)}(t)\rangle_t$ are calculated with respect to frame_{n+1}. With that, the window itself shifts by an increment of one pixel (or frame) along the main diagonal.

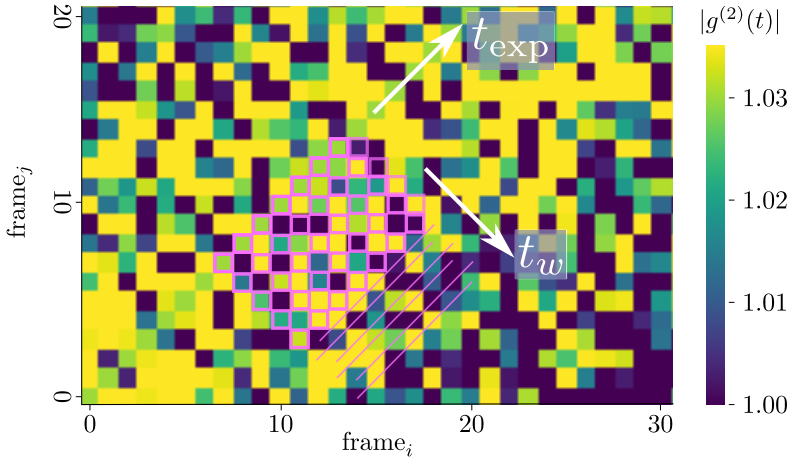

Figure 5.3: Sub-region of the TTCF shown in fig. 5.2 a) of the first 30 × 20 frames. Magenta coloured squares indicate a set of values of $g^{(2)}(t)$, taken into account for averaging, according to analyse the data along the ACS-axis. Magenta coloured lines indicate, just as the squares, the relevant set of $g^{(2)}(t)$ values and are used to ease up the illustration. White arrows show the directions in with experimental t_{exp} and waiting t_w time evolve.

Figure 5.3 exemplary illustrates the described method, averaging over seven frames (`TTCF-avg` $= 7$) around the frame with $n = 10$. Magenta coloured squares along one diagonal surround all pixels (or frames) taken into account for each increment of waiting time t_w. One set of squares along the main diagonal (or parallels) illustrates the values of $g^{(2)}(t_i)$ used for mean calculation of frame $n = 10$, corresponding to a certain time t_i along the experimental time axis t_{exp}. Sets of squares, parallel to the main diagonal, mark the val-

ues of $g^{(2)}(t)$ belonging to later waiting times t_w, accountable for averaging for $n = 10$. Magenta coloured lines symbolise the continuation of averaging until the last frame available, which belongs to the averaging window, is reached. These lines are only used to ease up the illustration. The union of pixels, marked either by magenta coloured squares or lines, build the data set of the rolling window, which was introduced earlier. That window moves along the t_{exp}-axis by increments of one pixel throughout the entire data set of the TTCF and builds the data basis for extended time resolved relaxation dynamics analysis.

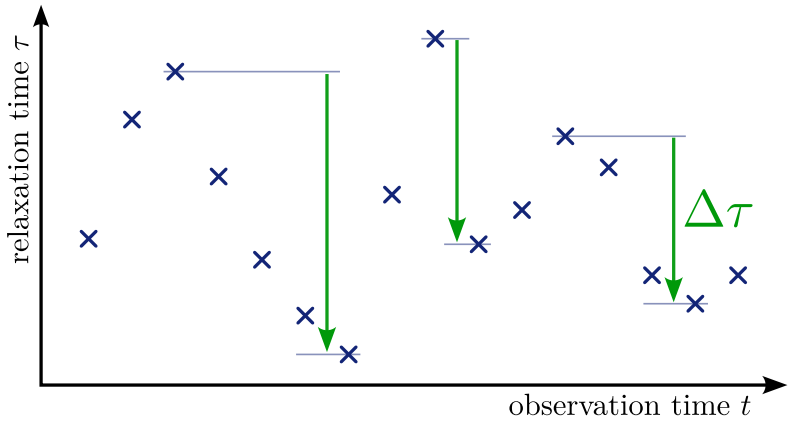

Figure 5.4: Scheme of the evolution of relaxation time τ with observation time on fictional data. Blue crosses symbolise τ data points. Pale blue horizontal lines mark local extrema. Green arrows symbolise the events of interest: here, relaxation time drops $\Delta\tau$ from a local maximum to the consecutive local minimum.

This data set of $\langle g^{(2)}(t)\rangle_t$ can be seen as its own *averaged* TTCF and is used for the following quantitative analysis. Therefore the KWW function 3.14 is fitted, *sequentially*, to each pixel row orthogonal to the main diagonal, hence along the ACS-axis. While doing that, depending on the earlier defined `TTCF-avg` value, it may be necessary to keep fit parameters of the KWW function fixed – in particular for small `TTCF-avg` values. This is possible by including the `python` library `lmfit`, which allows to keep parameters of the defined fit function fixed or limit them to a given range of values [New+22]. In many cases, changes of the base line parameter A or the contrast c of equation 3.14 are not expected within one TTCF. Hence, these parameters can be kept

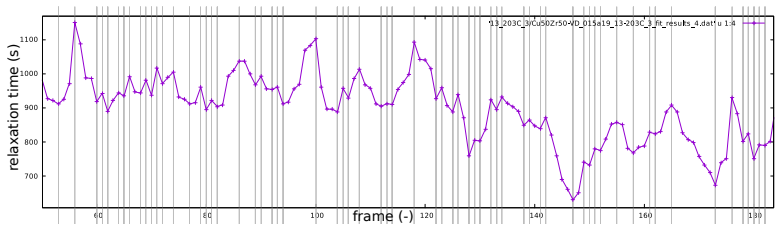

Figure 5.5: Evolution of τ along with frames of a small section of a TTCF. Gray vertical lines indicate the positions $\text{frame}_{\text{extremal}}$, corresponding to times t_{extremal}, between which the algorithm of `trcfit.py` identifies a drop $\Delta\tau$ in the sequential KWW fitted TTCF data.

fixed while their values can be obtained from conventional KWW-fitting of $\langle g^{(2)}(t)\rangle$ data, based on the average of the entire TTCF. These parameters are taken as input parameters for sequential KWW-fitting using the routine of `trcfit.py`. As an outcome, a data set of the evolution of the structural relaxation time vs experimental time $\tau(t)$ is obtained.

In order to perform a statistical analysis of that *relaxation time evolution*, it is necessary to define the parameters of interest. In the case of avalanche-like dynamics, the change of relaxation time $\Delta\tau$ during dynamics acceleration, given by a local maximum and its consecutive local minimum within the $\tau(t)$ data, is analysed. Figure 5.4 illustrates the definition of "relaxation time drops" $\Delta\tau$ in a schematic plot of fictional data. Blue crosses symbolise values of the relaxation time τ, obtained from sequential KWW fitting. Black horizontal lines identify all local minima and maxima, and green down facing arrows mark the quantity of interest for statistical analysis – here only drops of relaxation time $\Delta\tau$ are analysed. For cross-checking purposes and to give the reader an idea of how that assembles with real data, figure 5.5 shows the evolution of $\tau(t)$ (here as a function of frames) with vertical grey lines indicating all points in time (frames) at which a local extremal point is detected. Between a maximum and its consecutive minimum, $\Delta\tau$ is calculated and the data are stored for statistical analysis.

The data on drops of relaxation times $\Delta\tau$ are analysed by means of the `python` library `numpy` [Har+20]. A power-law easily uncovers in a double-logarithmic representation of the data. It is important to additionally apply logarithmic binning for equidistant arrangement of the histogram data along the abscissae.

However, this type of binning stronger assesses values of lower $\Delta\tau$, unequally enforcing the impact of small drops. To establish equal weight of the data and to effectively omit overrepresentation of data for small $\Delta\tau$, probability values are rescaled by the width of their actual bin w_{bin_i}, accomplishing a histogram of $\frac{1}{w_{\mathrm{bin}_i}} P(|\Delta\tau|)$. Linear regression then allows to fit a power-law exponent κ to the probability distribution of the analysed parameter. To identify possible changes of the slope, indicating a cross-over in the underlying physics, or pointing out a cutoff at a certain size limit of the studied parameter, linear regression helps to characterise the avalanche dynamics.

5.4 Results

The analysis of avalanche dynamics, based on XPCS data, is developed within this thesis. The numerical approach and its methodical implementation are described in the previous sections of this chapter. This chapter demonstrates its feasibility and therewith results on the statistical analysis of avalanche dynamics in an ultrastable metallic glass (UMG) with an effective composition of $Cu_{55}Zr_{45}$. Details on the compositional analysis can be found in chapter 2.5.3. After preparation and storage for 296 d at ambient temperature the sample was annealed at $T_\mathrm{a} = 536\,\mathrm{K}$, which corresponds to approximately $0.80\,\mathrm{T_g}$. A heating and cooling rate of $0.11\overline{6}\,\mathrm{K\,s^{-1}}$ was applied during annealing, and the sample was held at constant temperature for 1 min at T_a. In the following, this sample will simply be referred to as $\mathrm{UMG_a}$.

XPCS experiments have been carried out at in Grenoble, France, at the ESRF's beamline ID10 EH2. That beamline is designed in particular to achieve a (partially) coherent high flux beam of up to 4×10^{10} photons/(s 100 mA) at a photon energy of 8.1 keV ($\widehat{=}$ 0.153 067 nm), while the beam is collimated to 10 µm × 7 µm (horizontal × vertical). Samples are measured in transmission in wide angle geometry at a wave vector $|\boldsymbol{q}| \approx 27\,\mathrm{nm^{-1}}$. This particular value of q corresponds to the maximum of the static structure profile $I_{\mathrm{max}}(\boldsymbol{q})$, which itself manifests the average inter-particle ordering and may be interpreted as an average inter-particle distance within an amorphous sample. The geometry, at which the XPCS ex-

periment is performed, determines that the structural dynamics captured represents *local dynamics* – hence the dynamics of neighbouring configurations.

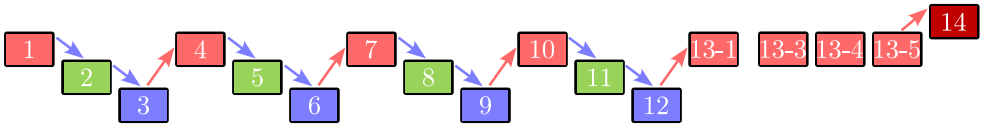

Figure 5.6: Schematic temperature protocol. Each coloured box refers to a measurement at constant temperature. Upper boxes indicate higher temperatures while lower boxes indicate lower temperatures, respectively.

A temperature protocol as schematically depicted in figure 5.6 was applied, where the temperature of the sample was cycled four times through a temperature loop of 476 K (light red boxes) – 456 K (green boxes) – 436 K (blue boxes). Each temperature step until step 13-1 was held for 2900 s before the next temperature was set, while each step from 13-1 onwards was held for 14 700 s. The last step 14 was held for 7300 s. Temperature rates of 0.05 K s^{-1} have been applied during temperature changes. After the fourth cycle completed, temperature was increased to the initial value of 476 K. Multiple sets of XPCS data were captured at that temperature. All different temperature steps are named with an increasing index, while multiple sets at one temperature are indicated by an appended digit (e.g. 13-1, for the first data set at the thirteenth temperature step, being $T_{\mathrm{exp}} = 476\,\mathrm{K}$). A fourteenth temperature set was collected at higher temperature as before with $T_{\mathrm{exp}} = 496\,\mathrm{K}$ (dark red box).

5.4.1 Statistics of typical relaxation dynamics

Figure 5.7 shows the TTCF of sample $Cu_{55}Zr_{45}$ at protocol step 13-3. The white contour line is the result of sequential KWW-fitting with the `trcfit.py` code, and confines the highly correlated area along the main diagonal. The noisy character of TTCF data pointed out earlier is handled with rolling-window averaging over 200 frames (`TTCF-avg`). The quantitative analysis of this contour is subject of this chapter.

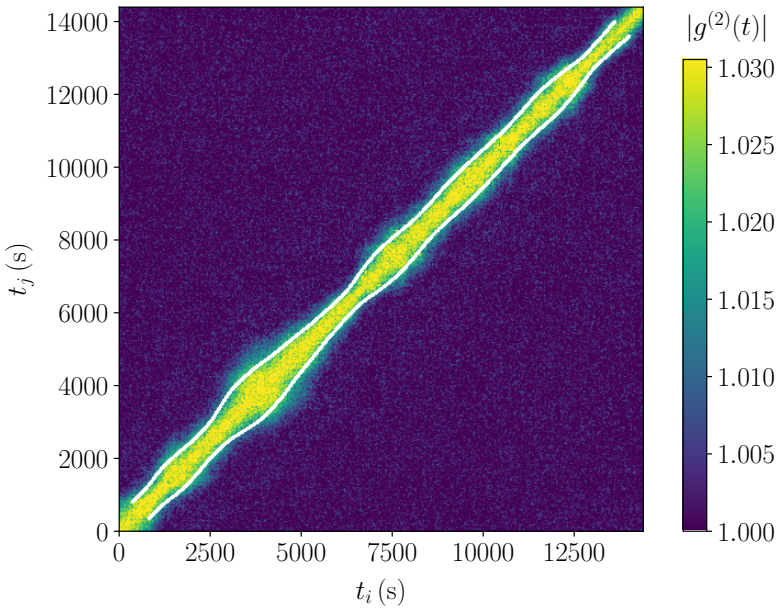

Figure 5.7: TTCF of UMG_a, captured by XPCS. The white contour displays the determined relaxation time τ from sequential KWW-fitting using the `trcfit.py` code with `TTCF-avg` = 200. A Gaussian filter ($\sigma = 1.5$) is applied to the actual correlation function.

Figure 5.8 shows the extracted evolution of the relaxation time versus experimental time $\tau(t)$. Vertically stacked panels depict the results of sequential KWW-fitting of the same data with different values for `TTCF-avg`. While the general evolution of the curves is identical, the uppermost panel clearly shows a high amount of noise, which decreases with higher `TTCF-avg` on lower panels. Although one may expect that also small changes and jumps of $\Delta\tau$ may disappear due to the averaging, this is not the case, as the inset (e) in figure 5.8 proves. The magnification of the boxed area in the region around $t = 7000\,\mathrm{s}$ shows, that in this flat-appearing area still lots of changes and jumps of $\tau(t)$ can be identified and quantitatively analysed. In order to provide adequate fitting, especially to fit to noisy data coming from smaller values of `TTCF-avg`, baseline parameter A and contrast c of the fit function 3.14 are kept constant and determined from a dataset averaged over the entire TTCF. These parameters are then used as fixed input parameters for the fitting model during sequential KWW-fitting with `trcfit.py`. Here, $A = 1.0005$ and $c = 0.03$ were used. Strong variations with high values of $\tau(t)$ towards the end of each

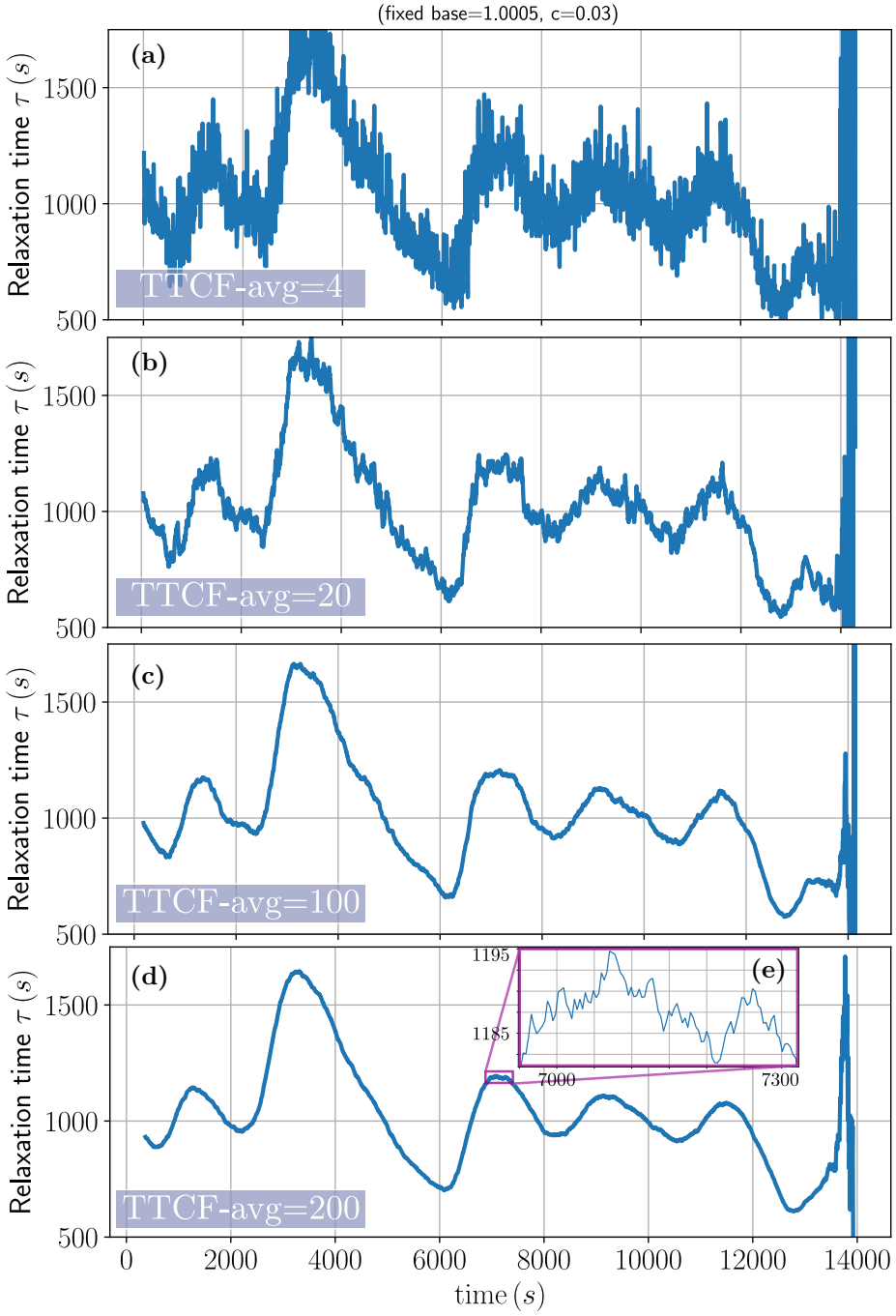

Figure 5.8: Results of sequential KWW-fitting by `trcfit.py` with different parameters for `TTCF-avg`: 4, 20, 100, and 200 frames. The inset in panel (e) shows a magnification of the boxed area. For adequate fitting, baseline and contrast parameters are kept fixed.

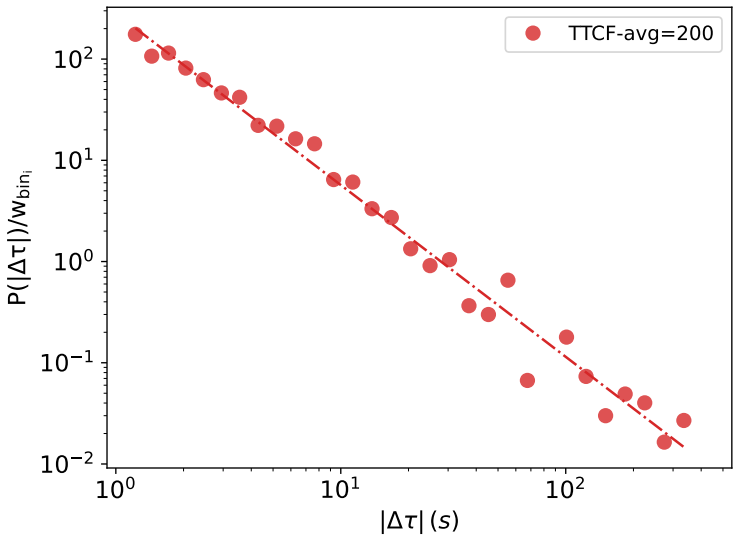

Figure 5.9: Distribution of rescaled relaxation time drops for UMG_a with `TTCF-avg` = 200. The dashed-dotted line displays a linear regression of the data with a slope of $\kappa = -1.70(4)$.

panel's curve are cut off after 3800 frames (approximately 13 680 s). They form because of the geometry of a TTCF, which limits the available data range towards the end of the time axis.

As the inset (e) in figure 5.8 already indicates, large and small drops of the relaxation time $\Delta\tau$ are still comprised in the relaxation time evolution data, even when a rather strong averaging over 200 frames is performed. Occurrence and distribution of $|\Delta\tau|$ are evaluated by means of the `python` library `numpy`, making use of the `numpy.histogram` function. Figure 5.9 shows the resulting histogram. Depicted on logarithmic scale with logarithmic binning, a power-law manifests as a linear correlation in the distribution. An index for the slope of $\kappa = -1.70(4)$ is identified, spanning more than two decades. However, the question arises, how does the choice of `TTCF-avg` alter the statistical distribution and hence the histogram.

Figures 5.10 (a) and (b) show the identical distribution $P(|\Delta\tau|)$ according to the data depicted in figure 5.8, applying smaller values of `TTCF-avg` as compared to figure 5.9, comparing different linear fitting regimes. Two regimes

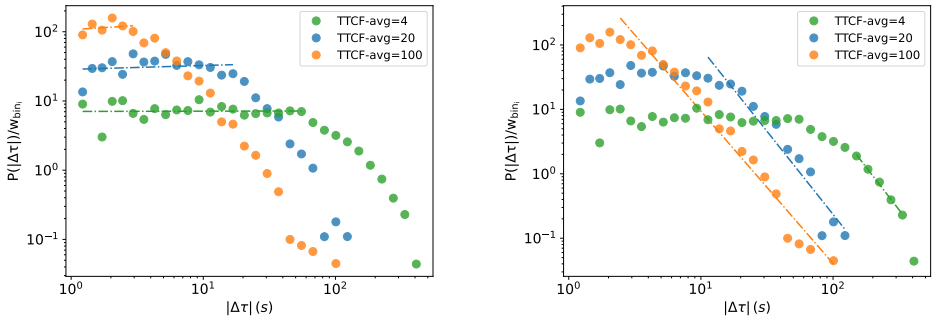

(a) constant regime fits **(b)** decreasing regime fits

Figure 5.10: Distribution of rescaled relaxation time drops for $\mathrm{UMG_a}$. Coloured, dashed-dotted lines display linear regressions of data of the corresponding colour. Only data points directly vertically above or below the line are taken into account.

can be identified: a constant regime towards smaller $|\Delta\tau|$, and a regime towards larger $|\Delta\tau|$ with a decreasing probability $P(|\Delta\tau|)$. Both graphs show that small values of `TTCF-avg` result in a wide spanning regime of constant slope. As a result, no common linear regime of negative slope with statistical relevance can be identified for `TTCF-avg` $= 4$, as there is no linearly correlated data spanning for at least one order of magnitude. Larger values of `TTCF-avg` result in an earlier crossover from constant to decreasing slope regime, enlarging the span of the regime where the distribution shows a linear form in the $\log - \log$ plot. That trend continues until, as seen already in figure 5.9 with `TTCF-avg` $= 200$, the constant regime at low $|\Delta\tau|$ has totally vanished. In table 5.1, the results from linear fits in the constant and the decreasing regime are collected. Noticeably, the constant regime (fig. 5.10a) reveals slopes rather close to zero. That is a strong imprint to the underlying physics and will be discussed later in section 5.5. Values for κ in the decreasing regime (fig. 5.10b) either have a very small data basis, and hence, are not representative for the distribution, or show large uncertainty. Only, the value with `TTCF-avg` $= 200$ stands out of the results for κ.

TTCF-avg	constant regime fit results for κ	decreasing regime fit results for κ
4	0.0(1)	−2.7(1)
20	0.1(1)	−2.6(3)
100	0.1(3)	−2.4(1)
200	–	−1.70(4)

Table 5.1: Numerical fit results of slopes κ from linear fits to distribution data, displayed in figures 5.9 and 5.10, and indicated by the corresponding dashed-dotted lines.

5.4.2 Statistics of heterogeneous dynamics

Heterogeneous dynamics emerges at later points in experimental time for MGs with relatively long thermal history or at later times during experiments on an MG [Eve+15; Das+19]. The previously applied statistical analysis method is used as well to quantify the statistics of the relaxation time evolution on XPCS data with such heterogeneous dynamics or with dynamics which shows the existence of certain "events". The left column of figure 5.11 shows an overview of different types of "events", while the column on the right hand side shows the corresponding distribution of relaxation time drops.

Panel 5.11a shows the first emergence of such a large, distinct deceleration of relaxation dynamics, setting on at around 4000 s in the image of the TTCF; the onset is marked by a white arrow in the TTCF image. After more than an hour of time, at around 8000 s, the dynamics accelerates almost as quickly as it decelerated in the first place. Note that the symmetry along the main diagonal is created artificially by the typical rendering of a TTCF where the upper left and lower right half of the matrix are mirrored along $t_i = t_j$. However, the symmetry along the experimental time axis t_{exp} is non-artificial and may carry information on the physical foundation of such heterogeneous dynamics. The white contour represents best fits from sequential KWW-fitting to the TTCF-avg = 200 averaged data. Note the difference between that white contour and the protuberances of the Gaussian filtered ($\sigma = 1.5$) actual correlation function.

Panel 5.11b depicts the corresponding rescaled distribution $P(|\Delta\tau|)$ with TTCF-avg = 200. It shows a similar linear form as in the typical relaxation

protocol step	decreasing regime fit results for κ
13-1	$-1.48(6)$
13-4	$-1.74(7)$
13-5	$-1.66(5)$

Table 5.2: Numerical fit results of slopes κ from linear fits to distribution data, displayed in figures 5.11, indicated by the corresponding dashed-dotted lines.

dynamics data, spanning over more than two decades.

In contrast, the TTCF of panel 5.11c displays an intrinsically different heterogeneous dynamical "event". It is displayed with the very same parameters as the TTCFs before, but shows the emergence of discontinuous evolution of the relaxation time τ. The onset of the discontinuity is marked by a white arrow in the TTCF image. At $t_i \approx 3500\,\mathrm{s}$, the evolution of the correlation function is interrupted, which is shown throughout an entirely decorrelated signal on the main diagonal at the initiation point of the "event", and by the rectangular artefact emerging from that point. Here the dynamics is faster than the temporal resolution. However, the distribution of the relaxation time drops, displayed on panel 5.11d, is not affected by this discontinuity. It shows a similar linear form as in the typical relaxation dynamics data, spanning over more than two decades.

A similarly appearing "event" is shown in the TTCF of panel 5.11e, though details differ. A close look at the onset of the "event" marked by a white arrow in the TTCF image reveals no discontinuity of the correlation function $\left|g^{(2)}(t)\right|_{t_i=t_j}$. The relaxation dynamics rather accelerates strongly just before it abruptly slows down immediately after. The "event" is also accompanied by bright rectangular wings, just as in the TTCF of panel 5.11a, although those are not rectangular but evolve rather curved. Yet, the distribution of the relaxation time drops displayed on panel 5.11f are not distorted by the appearance heterogeneous dynamics.

Table 5.2 summarises the slopes obtained by statistical analysis of the precedently described TTCF data, along with the according temperature protocol.

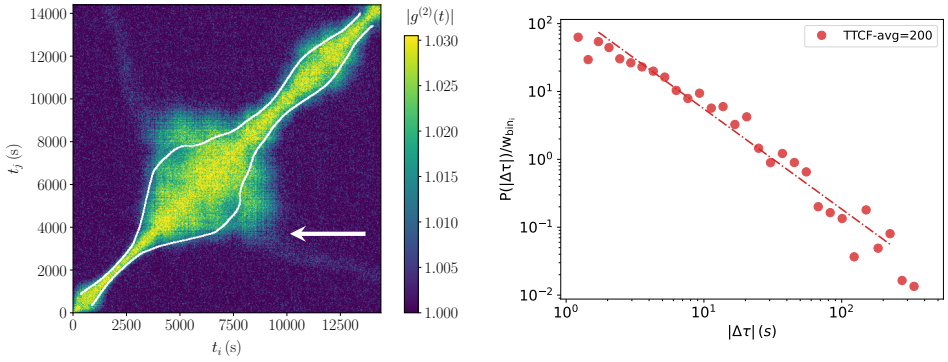

(a) TTCF of 13-1 **(b)** Distribution of 13-1

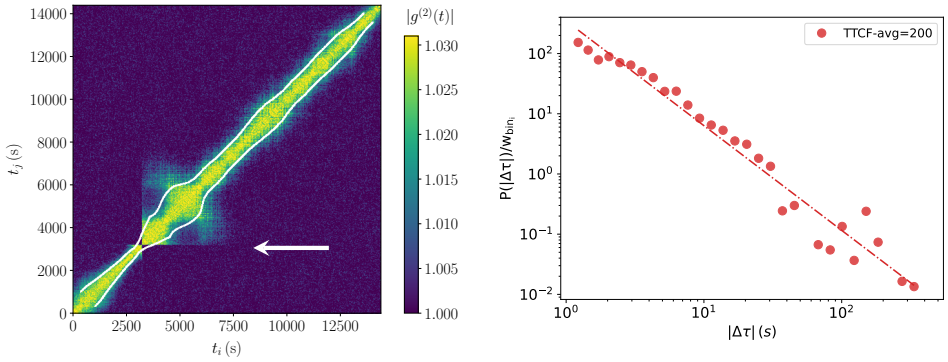

(c) TTCF of 13-4 **(d)** Distribution of 13-4

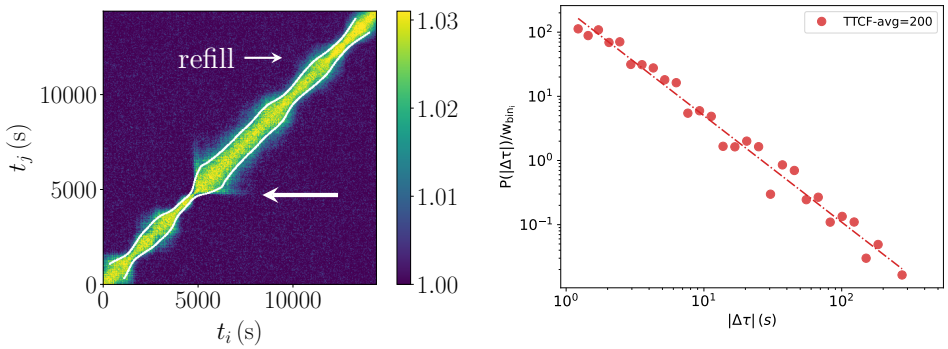

(e) TTCF of 13-5 **(f)** Distribution of 13-5

Figure 5.11: TTCFs and relaxation time drop distribution graphs of UMG_a. Left column: TTCFs with `TTCF-avg` = 200. A Gaussian filter ($\sigma = 1.5$) is applied to the actual correlation function. The white contour displays the determined relaxation time τ from sequential KWW-fitting. White unlabelled arrows mark the onset of certain "events". Right column: Rescaled distribution of relaxation time drops. Coloured, dashed-dotted lines display linear regressions to the distribution data. Only data points directly vertically above or below the line are taken into account for the regression.

5.5 Discussion

Performing a statistical analysis of a fluctuating signal is a challenge of itself and can only be touched in this PhD thesis. The data in the here presented way do carry the observable of interest, but this observable – the imprints of avalanche dynamics – needs to be explored first. As the correlation data, obtained from XPCS experiments, are subjected to an enormously low signal-to-noise ratio, a finely time-resolved evolution of the relaxation time is at least as challengingly to achieve as it is of interest to gain understanding of relaxation dynamics in MGs. Therefore the evaluation here is meant to be a first step forward and may carry the risk of including errors in the data processing. From that, the first question deviates: which physical quantity classifies an avalanche? In the here presented work, avalanches are understood as dynamical events which are characterised through a deceleration of the relaxation dynamics, subsequently followed by an acceleration of the dynamics (stick-slip events on long time scales). The observed time scale results from the technical capabilities of XPCS experiments during the time of data acquisition and is limited to a few seconds on the short time scale. These dynamical events may be attributed to thermally driven, randomly arranged atomic fluctuations, which, at some point happen to appear in neighbouring configurations. This phenomenon can be identified as a change of the relaxation time τ from a local maximum to its following local minimum – here referred to as *relaxation time drop*.

In this work, the parameter studied in order to investigate avalanche statistics is the relaxation time drop $|\Delta\tau|$. It can be understood as the characteristic quantity for the size of an avalanche because the relaxation time is directly correlated to the spacial arrangement of the scatterers (atoms). Before an avalanche is released, stresses build up – the system gets stuck. At a certain point in time, the stress is released, causing the dynamics to accelerate. Hence, a large change of relaxation time is based on spacial rearrangements of a large amount of scatterers. Here, the time scale for these rearrangements is found to range from seconds to minutes. Avalanche statistics characterised through stress drops in numerical stress-strain experiments was recently investigated by Lagogianni et al. as well as in numerical stress time series by earlier

studies [Lag+18; Liu+16].

A critical point is the TTCF-averaging as sketched in figure 5.3. Averaging is necessary as the KWW fit function is a monotonously decaying function, while TTCF data usually fluctuates multiple times towards its initial (maximum) value of the correlation function along with the waiting time t_w. This characteristics does not reflect the underlying physics of a decaying correlation and hence, is based on noise. To be able to associate a certain relaxation time τ to the relaxation behaviour, respecting the monotony of the KWW function, averaging needs to be performed. However, this need to average builds up a conflict with the fundamental motivation of this chapter, seeking for avalanche statistics which manifests itself through fluctuations of the evolution of the relaxation time $\tau(t)$. Yet, it was successfully demonstrated that averaging efficiently suppresses fluctuations based on noise, while at the same time preserving fluctuations based on the relaxation dynamics. There are two arguments for this claim. First of all, figure 5.8, which shows the evolution of relaxation time $\tau(t)$, confirms that with a larger averaging window (`TTCF-avg`), fluctuations on the $\tau(t)$ signal decrease (from top to bottom panel). However, small fluctuations, which are not visible in the depiction of the full curve, but in the inset of the bottom panel (fig. 5.8 (e)), affirms that, even though vast averaging is applied, fluctuations remain present and detectable. Second, even stronger evidence lies in the distributions themselves. Figures 5.9 and 5.10 show an increase of the power-law characteristic regime with increasing `TTCF-avg` parameter, which filters fluctuations based on noise. This argument holds, especially when accurately examining the *constant* regime. Fitting a linear function to the data of this region reveals a slope of zero. In a distribution plot, a slope of zero is also called *uniform distribution* and means that all quantities are distributed evenly. This is exactly what characterises white noise [Chi76]. With larger `TTCF-avg` values, the regime, in which white noise characteristics predominates, shrinks towards smaller $|\Delta\tau|$. This can be intuitively understood by first averaging out large noise based fluctuations, effectively shifting them towards smaller values. Finally, with `TTCF-avg` $= 200$, the uniformly distributed regime vanishes, which denotes the value to be the optimal averaging-window width for the studied system.

The power-law exponents κ, found within the here presented work, are all in a range between $-1.74(7)$ and $-1.48(6)$. With that, they are close to the value found by Krisponeit et al. in their first regime of so called "random three-dimensional avalanches", although they report a time-based quantity which they attribute the avalanche statistics to, what they call "waiting time" [Kri+14]. Besides, studies in MD simulations of Lagogianni et al. report an exponent of -1.25 for the distribution of avalanche size, whereas time-based (as they referred to as "duration") avalanche statistics reports exponents of -1.55. Both cases report slightly lower exponents compared to the ones found in the here presented data. This might be based on the fact that both publications studied avalanche dynamics upon tensile stresses, whereas the here presented work examined non-directional excitations of the dynamics.

Microscopically, the former studies indicate the release of mechanical stresses by the formation of STZs, which cooperatively build a local shear band. Shear bands are identified also by electron microscopy and atomic force microscopy [Maa+15; Maa+14]. On longer time scales as studied here, these STZs get activated randomly in space and time to lower the overall potential energy but without direct interaction as the power-law exponent of $\kappa = -3/2$ is indicating. Such a power-law exponent is well known from the famous Richter-scale in earth quakes and from the basis of independently activated processes [GR54].

Additionally, the interpretation of the earlier described "events" in the TTCFs, particularly shown in the figures 5.11a, 5.11c, and 5.11e is complex. Such patterns in the TTCF image can have several reasons, such as temperature fluctuations, temporal X-ray beam or infrastructural instabilities such as shaking, vibrations of the sample, the detector or the goniometer itself, thermal issues of the detector, just to name some probable causes. For every event occurring, all those external influences need to be excluded explicitly, as has been done for the herein presented data. However, in some situations, the origin remains unclear. The figures 5.11a and 5.11e show plausible events, which have also been reported in studies of on long thermal cycling [Eve+15; RPE17; Das+19], because all aforementioned causes could be excluded as a cause of

the events. Especially figure 5.11e even confirms that a change of the X-ray beam's intensity does not result in such events, as a refill of the electron beam occurs at approximately $t_i = 12\,000\,\mathrm{s}$, not triggering a spurious pattern of the correlation function, but instead simply an increase of the value of $g^{(2)}(t)$. Additionally, the refill also affects the position of the beam and the emittance, which also does not give rise to the occurrence of an "event". Discovering intermittent aging events in the here presented sample of an after preparation annealed UMG ($T_\mathrm{a} = 0.80\,T_\mathrm{g} \mathrel{\widehat{=}} 536\,\mathrm{K}$) agrees with the findings described in chapter 4, where sample $\mathrm{UMG}_{T_\mathrm{g}^-}$ ($T_\mathrm{a} = 0.97\,T_\mathrm{g} \mathrel{\widehat{=}} 650\,\mathrm{K}$) shows similar behaviour. In contrast, figure 5.11c depicts a full decorrelation of $\left|g^{(2)}(t)\right|_{t_i=t_j}$, resulting in a sharply drawn geometric "butterfly" pattern. Together with the fact, that it does not show the emergence of "wings", it should be treated as an experimental artefact.

5.6 Outlook

The here presented statistical analysis of avalanche dynamics has proven evidence to work with XPCS data on VD MG. As this method is easily applicable to other already captured XPCS data, it would be of great interest to apply this method to data of different systems to strengthen the knowledge on avalanche dynamics. On the one hand, these studies could be performed on different material systems in similar conditions, which are known to show disparate behaviour based on the concept of fragility. On the other hand, studies with set-ups in which uni-directional excitation such as the application of tensile stress or in bending studies are performed, would open an entire new class of experiments. Especially in such uni-directionally excited systems, the experimental realisation of studies of plastic events in the so called elastic regime could give new insights into the microscopic behaviour of relaxation processes, as recently published on simulations by Lagogianni et al. and works by Krisponeit et al. suggest [Lag+18; Kri+14].

Chapter 6

General conclusions

The scope of this work is to study structural relaxation phenomena of metallic glasses on microscopic length scales. Therefore two recently opened areas are put together: X-ray photon correlation spectroscopy as a technique which is capable of capturing collective atomic rearrangements on the microscopic scale in disordered matter, and ultrastable metallic glasses establishing a novel class of glasses with outstanding characteristics.

By means of vapour deposition UMG samples are produced proving their enhanced kinetic and thermodynamic stability throughout increased structural relaxation times, compared to their conventionally produced counterparts. The understanding of UMGs within the framework of the potential energy landscape can be reinforced by the findings within this thesis. Although UMGs are proven to be located in a deep state in the PEL, $Cu_{55}Zr_{45}$ UMG shows entire structural rearrangements via full decay of the correlation function $g^{(2)}(\boldsymbol{q}, t)$ investigated by XPCS experiments deep in the glassy state at temperatures of approximately $0.65\,T_\mathrm{g}$ to $0.71\,T_\mathrm{g}$ (436 K to 476 K). However, a comparison with ultrastable MGs annealed at temperatures $T_\mathrm{a} = (1 \pm 0.03)\,T_\mathrm{g}$ after their preparation underlines the ultrastable character of as-prepared UMGs. Annealing a UMG confirms its low energetic state, giving rise to unique *Anti-Aging* behaviour. Annealing at temperatures higher that the substrate temperature at which it was produced ($T_\mathrm{sub} = 0.89\,T_\mathrm{g}$) introduces enough energy into the system to randomise the UMG's stable configuration, destroying its ultrastable character, and boosting the glass out of its low energetic state on a pathway opposite to the one of genuine aging. Moreover, anti-aging is not equal to "rejuvenation" as a UMG sample has never

seen a "juvenile" high energy state to which it could be restored. Certainly it can be concluded that the enhanced surface mobility during preparation of UMGs is a true shortcut to stability, compared to recent studies of Zhao et al., which demonstrate the preparation of an ultrastable MG throughout aging a common MG for almost two decades at ambient temperature [Zha+22].

In macroscopic measurements the glass transition temperature is often defined by the relaxation time being equal to 100 s (equivalent to 10^{12} Pa s) [Ang95]. From that perspective it seems contradictory when relaxation times of $\tau \approx 200\,\mathrm{s}$ ($\mathrm{UMG_{ap}}$), and $\tau \approx 120\,\mathrm{s}$ ($\mathrm{UMG}_{T_\mathrm{g}^-}$, $\mathrm{UMG}_{T_\mathrm{g}^+}$, $\mathrm{FQ_{ap}}$) and below are determined throughout XPCS at temperatures deep in the glassy state at 476 K (approx. $0.71\,T_\mathrm{g}$). However, two aspects invalidate this contradiction: First of all, the aforementioned definition of T_g is based on macroscopic studies where the entire bulk sample contributes to the measurement, whereas XPCS measurements are only sensitive to rearrangements of neighbouring scatterers (atoms). Second, recent studies of Hechler et al. show that XPCS studies on a MG, one in the glassy state and one in the SCL state resulting in relaxation times which differ by a factor of 15, although captured of the same compositions at the very same temperature. Additionally, the KWW shape parameter in the SCL is found at common values below unity, while the glassy regime yields $\beta = 1.6$ [Hec+18], similarly high as determined within the here presented work. Hence, relatively low absolute values for the determined relaxation times in XPCS experiments may be connected to the uncommonly high values of β compared to different techniques, as the both affect the result of the value for τ from KWW modelling. Notwithstanding these absolute values of τ, relaxation times of UMG samples are relatively high (slow relaxations) in comparison to annealed UMGs or any kind of FQ MGs of similar elemental composition, underlining their kinetic stability. In addition, upon T-cycling, all probed samples but $\mathrm{UMG}_{T_\mathrm{g}^+}$ show memory effects throughout history dependent aging. After some iterations, they reach a plateau, a metastable state, while $\mathrm{UMG_{ap}}$ is found to be the utmost stable sample, affirming its ultrastable character. Why the UMG sample annealed above T_g ($\mathrm{UMG}_{T_\mathrm{g}^+}$) does not show any memory effect is based on heating it into the equilibrium regime. With that a glass' history is erased, while

this particular sample shows characteristics of a metastable state within a high energy meta-basin in the PEL. Further investigation, in particular high resolution XRD could give an insight if the sample shows indications of crystallisation, although no onset of a Bragg peak has been noticed in the area of the detector during XPCS measurements.

XPCS data carries an enormous variety of information, the challenge is to tame the strongly fluctuating signal. However, during the second project of this thesis, spotlight is put on the quantitative analysis of fluctuations along with the temporal evolution of the relaxation time. The challenge in particular is to fit the monotonic decreasing KWW function to a very noisy signal, which jumps multiple times form high to low value along with the t_w-axis. The evolution of best fits of KWW parameters are subjected to further analysis, as they give rise to underlying principles of the relaxation dynamics such as avalanche behaviour or to gain understanding of the peculiar role of the shape parameter β. In any case, an averaging algorithm is essential to manage the noise, while the data basis should be preserved as much as possible. A rolling-window averaging method holds these requirements and is successfully applied, giving access to the evolution of the KWW parameters $\tau(t_{\mathrm{exp}})$, $\beta(t_{\mathrm{exp}})$, and $c(t_{\mathrm{exp}})$ from fits to TTCFs. Depending on the SNR, one or more parameters can be fitted while others need to be fixed to a value representative for a full TTCF. With that method, a tool box (`trcfit.py`, `tau-statistics.py`) is made available to perform statistical analyses of relaxation dynamics, if just the TTCF is sufficiently large and carries enough contrast.

XPCS measurements of T-cycles at $T_{\mathrm{a}} = 0.80\,\mathrm{T_g}$ ($\widehat{=}\ 536\,\mathrm{K}$) annealed UMG provides sufficient data basis, contrast, and variation of relaxation dynamics in order to perform a statistical analysis of relaxation time fluctuations. Within a long temperature protocol, this sample is rich in τ-fluctuations, small and large ones, and shows large "events" of stuck dynamics which accelerates after a while, forming peculiar "butterfly patterns". With that, this non-directionally excited dynamics holds as a model system to investigate avalanche-like behaviour. A critical question is the choice of the quantity which describes an avalanche. Here, within the evolution of relaxation time

$\tau(t_{\mathrm{exp}})$, the absolute height of each relaxation time drop $|\Delta\tau|$ is subject of the statistical analysis. However, the SNR of a TTCF is poor, due to the very low scattered coherent signal, although data are collected at one of the beamlines with highest available coherent flux in the world, suited for XPCS experiments. From this arises the challenge to find a method which suppresses the fluctuations based on technical noise while keeping the fluctuations based on relaxation and avalanche dynamics of the studied system. The applied method could identify the optimal averaging parameters for the model system used. With that, avalanche dynamics with a critical power-law exponents in a range from $-1.74(7)$ to $-1.48(6)$ could be identified, spanning a linear relation between the rescaled probability $\frac{1}{w_{\mathrm{bin}_i}} P(|\Delta\tau|)$ and the relaxation time drop height $|\Delta\tau|$ over more that two orders of magnitude. These first results may be related to the cooperative formation STZs, resulting in "random three-dimensional avalanches" as seen in stress-strain experiments and simulations [Kri+14; Lag+18]. However, performing experiments under uni-directional stress would be of great benefit to relate macroscopic experiments and microscopic simulations with microscopic (XPCS) experiments.

The origin of heterogeneous dynamics, intermittent aging "events", or "butterfly" patterns remains unclear. However, it is crucial to eliminate influences coming from the machine, external influences such as vibrations, temperature fluctuations, and other technical issues, as they can all be an origin of geometric patterns and artefacts in the TTCF when analysing them. Thus, such events as depicted in fig 5.11a appear to emerge towards the end of long temperature cycles, which may be related to the total exposure time or the deposited energy.

Chapter 7

Acknowledgements/Danksagung

On a long path one naturally cross many people's paths. With most you walk a few steps, with some you climb steep mountains, but with only a few you undertake entire journeys. This thesis represents a long journey for me. I have grown through most of the acquaintances I have made, and I would like to emphasise a few in particular.

First of all I want to thank Prof. Konrad Samwer. He was constantly confident and concerned to create the conditions for me to do my work. But I am particularly impressed by his unwavering patience, to which I owe the completion of this work.

I also thank Beatrice Ruta for agreeing on being my second supervisor. I still remember my first day, when I arrived to France and she welcomed me with the keys to my temporary flat.

Furthermore, I thank Prof. Matthias Krüger for his spontaneity to also being part of my thesis committee and for accepting to be the second referee on this thesis.

Besides, I thank the further members of my examination board, Prof. Vasily Moshnyaga, Prof. Cynthia Volkert and in particular Prof. Michael Seibt.

I also want to thank my collaborators Eloi Pineda for the fruitful discussions and for proving samples. I want to thank Simon Hecher, Julian, Felix Lehmkühler and Lara Frenzel. I thank Kirsten Martens and Prof. Jean-Louis Barrat for the fruitful discussions and I thank Marco di Michiel and Sarah Goberna for the XRD measurements during their inhouse beamtime.

When I started my thesis' first year in Göttingen, I was warmly welcomed by the glass group. I remember with pleasure the nights with "the Spanish community" to which Alexandra and Carlos introduced me. Thanks to Yuansu for teaching me how to tame the sputtering machine.

Also I want to thank Prof. Markus Münzenberg who was not explicitly connected to this thesis, but he laid the foundations of my scientific work and that is what I am exceptionally grateful for.

Thanks as well to the workshop, Hartmut, whenever something needed to be build of fixed, „Bis wann? Gestern!?" were is first words with a big smile on his face. Carsten, not only the computer guy, but actually someone who laid the foundation of my new sportive hobby by suggesting me the bike which I bought from my first PhD salary and still love to ride.

I also want to thank Stefan Mathias for providing me an office even though I was only a guest during the last years.

All over, I am very grateful that I had the chance to grow in the I. Institute for Physics. The warm and welcoming atmosphere was exceptional. That certainly is also a legacy of Mr. Samwer's culture on how to direct the institute.

Apart from Germany, I found a new home for two years. There could be a worse place than the French Alps.

I found a new multilingual group, the beamline ID10 at the ESRF and I am grateful to have met Oleg, Yuriy, Federico and Karim. Moreover, I also found new friends there which I am happy to have met, as being abroad is not always fun. However, I loved the lunch time rides with the Néron BMX Gang, the tours with Pablo, Tilmann, Thomas, Piere and of course Oonagh. I also remember the winter weekends, at which the alarm clock rang even earlier than during the week – insane – but it was worth it because these weekends were devoted to skiing trips in the Alpes with Andreas, Oonagh, Pablo, Tilman, ...the group grew with every trip! Special thanks also to Michael Wulff for his repetitively warm words and plenty of sportive offers. One person should be risen a little higher than the others and this is Sylvain Prévost. Sylvain supported me from the first day when I arrived (for the second time) offering

me accommodation, and did so again uncountable times. He found uplifting yet down-to-earth words when I was desperate.

A person to whom I am also very grateful, who may not suspect anything of the kind, is Cécil Reboul. She gave me support when I needed it – namaste.

During the last weeks of my thesis, things got hectic. Therefore, I am especially grateful for the support of my closest friends, who continuously believed in me, encouraged me and supported me wherever possible. Many thanks to Ralph, Kira, Hannah, Roland, Judith, Nicki and especially Nina, who helped me to build myself up in my most difficult moments.

Zum Schluss möchte ich noch meiner Familie danken, meinen Brüdern, Großeltern, die nicht müde wurden zu fragen, wann ich denn endlich „mit der Schule fertig sei“ und insbesonders meiner Mutter, die fortwährend an mich geglaubt und mir Mut zugesprochen hat.

Appendix A

Technical details of XPCS measurements at ID10 EH2 (ESRF)

A.1 Temperatur cycle protocol

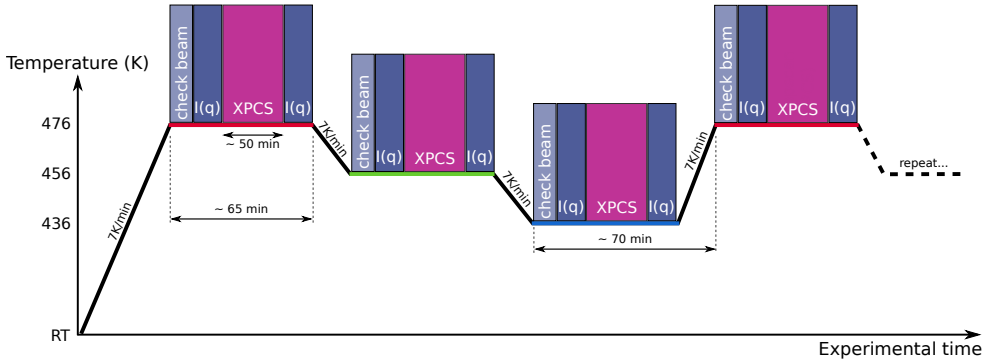

Figure A.1: Temperature protocol graph including experimental steps at each isothermal (check beam, $I(\boldsymbol{q})$, XPCS, $I(\boldsymbol{q})$).

A.2 Furnaces

The following two pages show technical drawings of the two used furnaces in order to perform XPCS experiments at ESRF's beamline ID10 EH2.

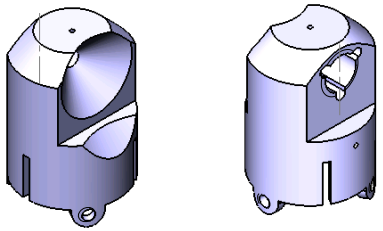

DÉTAIL B
ECHELLE 6 : 1

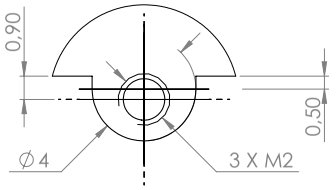

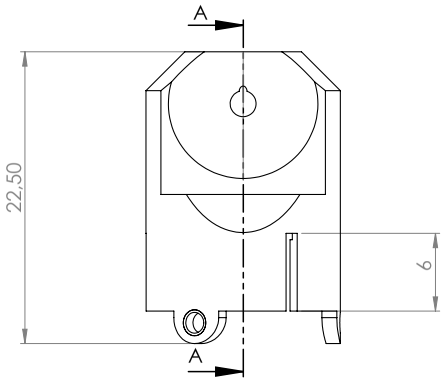

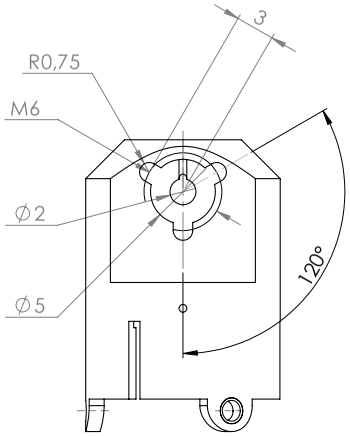

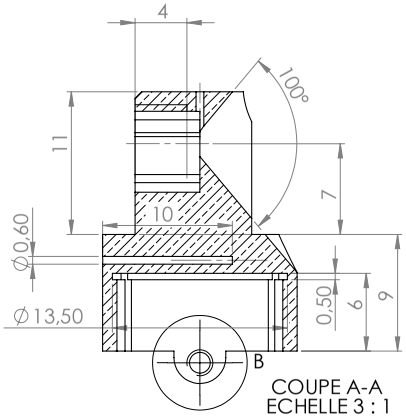

COUPE A-A
ECHELLE 3 : 1

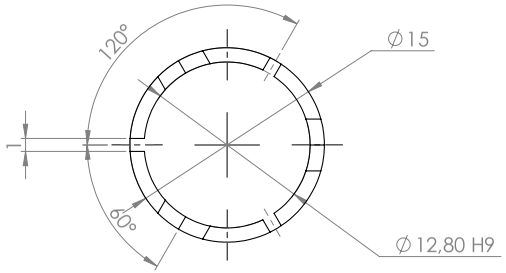

QTY = 1

		NICKEL			0,016
DESCRIPTION / REMARKS		MATERIAL		TREATMENT	W.(Kg)

SCALE: 2/ 1
0mm 50

	NAME	DATE
DRN.	K.LHOSTE	25/11/14
CKD.		
APPD.		

GEN. TOL. :
GEN. SURFACE FINISH : N7

ID 10 MICROTOMO HWL FURNACE SAMPLE HOLDER-SCREWED PLUG BASE

ASSY.

A3

EUROPEAN SYNCHROTRON RADIATION FACILITY
CS 40220 - 38043 Grenoble Cedex 9
TEL. 04-76-88-20-00 WWW.ESRF.FR

MOD	DATE	DRND.	APPD.	DESCRIPTION

ESRF

SolidWorks

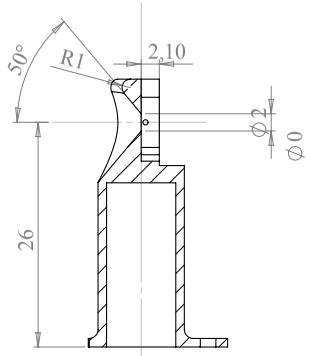

COUPE A-A

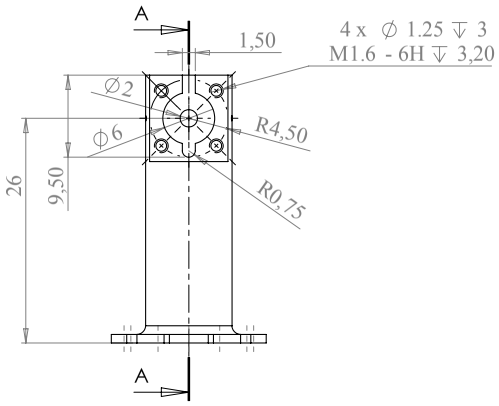

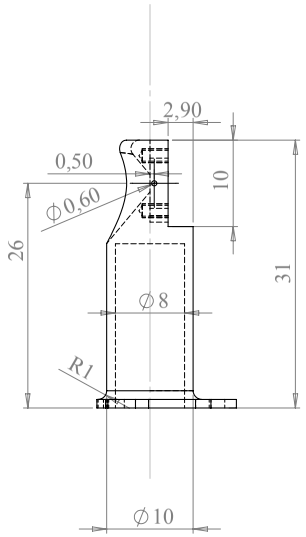

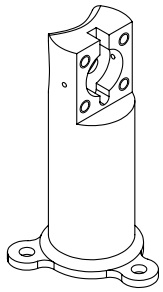

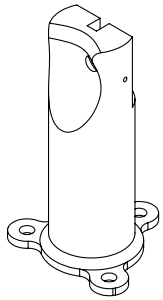

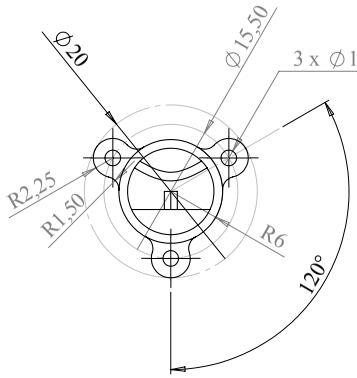

ITEM	DRAWING N.	QTY	DESCRIPTION / REMARKS	MATERIAL	W./Kg
		1		NICKEL	0,0078

0 mm SCALE: 2/ 1 50

	NAME	DATE
DRN.	LHOSTE K.	27/10/11
CKD.		
APPD.		

1000°c MICROTOMO. FURNACE
NICKEL SUPPORT
FOR DISC SAMPLE

ISO STANDARD
GEN. SURFACE FINISH : N7
GEN. LINEAR TOL. : Js12
GEN. ANGULAR TOL. : ±0,5°

EUROPEAN SYNCHROTRON RADIATION FACILITY
BP 220 38043 GRENOBLE CEDEX-FRANCE
TEL. 04-76-88-20-00 FAX 04-76-88-20-20

ASSY. 19.52.1060

19.52.1071

A3

MOD	DATE	DRND.	APPD.	DESCRIPTION

ESRF

SolidWorks

Appendix B

Temperature protocol for DSC measurements

The temperature protocol for analysing the glass transition of a MG is the following:

1. Switch on all devices and equilibrate the machine for 1 h
2. Equilibrate at 40 °C for 5 min
3. Heat up to 550 °C at 10 K min^{-1}
4. Cool down at 50 K min^{-1}
5. Equilibrate at 40 °C for 10 min
6. Heat up to 550 °C at 10 K min^{-1}
7. Cool down to room temperature (no ramp)

Bibliography

[Aga+19] I V Agapov et al. "Status of the PETRA IV project." In: *Proc. 10th International Particle Accelerator Conference (IPAC'19), Melbourne, Australia, 19-24 May 2019*. International Particle Accelerator Conference 10. Geneva, Switzerland: JACoW Publishing, 2019, pp. 1404–1407. ISBN: 978-3-95450-208-0. DOI: 10.18429/JACoW-IPAC2019-TUPGW011 (cit. on p. 81).

[AHK85] David Attwood, Klaus Halbach, and K.-J. Kim. "Tunable Coherent X-rays." In: *Science* 228.4705 (June 1985), pp. 1265–1272. ISSN: 0036-8075. DOI: 10.1126/science.228.4705.1265 (cit. on pp. 33, 34).

[AM11] Jens Als-Nielsen and Des McMorrow. *Elements of Modern X-ray Physics*. 2nd ed. John Wiley & Sons, Ltd, 2011. ISBN: 978-0-470-97395-0 (cit. on p. 34).

[Ami+21] N. Amini et al. "Intrinsic relaxation in a supercooled ZrTiNiCuBe glass forming liquid." In: *Physical Review Materials* 5.5 (2021), pp. 1–8. ISSN: 24759953. DOI: 10.1103/PhysRevMaterials.5.055601 (cit. on p. 55).

[And+15] D. Andrault et al. *Esrf Upgrade Programme Phase II (2015-2022)*. Ed. by Gary Admans et al. Grenoble, 2015, pp. 1–194 (cit. on pp. 34, 81).

[Ang+00] C. Austen Angell et al. "Relaxation in glassforming liquids and amorphous solids." In: *Journal of Applied Physics* 88.6 (Sept. 2000), pp. 3113–3157. ISSN: 0021-8979. DOI: 10.1063/1.1286035 (cit. on pp. 8, 14).

[Ang95] C. Austen Angell. "Formation of Glasses from Liquids and Biopolymers." In: *Science* 267.5206 (Mar. 1995), pp. 1924–1935. ISSN: 0036-8075. DOI: 10.1126/science.267.5206.1924 (cit. on pp. 11, 68, 110).

[Bad+07] Prashanth Badrinarayanan et al. "The glass transition temperature versus the fictive temperature." In: *Journal of Non-Crystalline Solids* 353.26 (Aug. 2007), pp. 2603–2612. ISSN: 00223093. DOI: 10.1016/j.jnoncrysol.2007.04.025 (cit. on p. 9).

[Bap+20] V. Bapst et al. “Unveiling the predictive power of static structure in glassy systems.” In: *Nature Physics* 16.4 (Apr. 2020), pp. 448–454. ISSN: 1745-2473. DOI: 10.1038/s41567-020-0842-8 (cit. on p. 3).

[Bar+13] Jordi Baró et al. “Statistical Similarity between the Compression of a Porous Material and Earthquakes.” In: *Physical Review Letters* 110.8 (Feb. 2013), p. 088702. ISSN: 0031-9007. DOI: 10.1103/PhysRevLett.110.088702 (cit. on p. 86).

[BBH69] J C Bauwens, C Bauwens-Crowet, and G Homès. “Tensile yield-stress behavior of poly(vinyl chloride) and polycarbonate in the glass transition region.” In: *Journal of Polymer Science Part A-2: Polymer Physics* 7.10 (1969), pp. 1745–1754. DOI: https://doi.org/10.1002/pol.1969.160071010 (cit. on p. 1).

[BCL00] L. Bellon, S. Ciliberto, and C. Laroche. “Memory in the aging of a polymer glass.” In: *Europhysics Letters* 51.5 (2000), pp. 551–556. ISSN: 02955075. DOI: 10.1209/epl/i2000-00368-1 (cit. on p. 77).

[BCL02] L. Bellon, S. Ciliberto, and C. Laroche. “Advanced memory effects in the aging of a polymer glass.” In: *European Physical Journal B* 25.2 (2002), pp. 223–231. ISSN: 14346028. DOI: 10.1140/epjb/e20020025 (cit. on p. 77).

[Ber+17] Ludovic Berthier et al. “Origin of Ultrastability in Vapor-Deposited Glasses.” In: *Physical Review Letters* 119.18 (Nov. 2017), p. 188002. ISSN: 0031-9007. DOI: 10.1103/PhysRevLett.119.188002 (cit. on pp. 2, 20, 60, 72).

[Bik17] Oier Bikondoa. “On the use of two-time correlation functions for X-ray photon correlation spectroscopy data analysis.” In: *Journal of Applied Crystallography* 50.2 (Apr. 2017), pp. 357–368. ISSN: 1600-5767. DOI: 10.1107/S1600576717000577 (cit. on pp. 54, 55).

[Bou+17] Mehdi Bouzid et al. “Elastically driven intermittent microscopic dynamics in soft solids.” In: *Nature Communications* 8.May (June 2017), p. 15846. ISSN: 2041-1723. DOI: 10.1038/ncomms15846 (cit. on pp. 53, 55, 80).

[BP01] J.-P. Bouchaud and E. Pitard. “Anomalous dynamical light scattering in soft glassy gels.” In: *The European Physical Journal E - Soft Matter* 6 (Nov. 2001), pp. 231–236. ISSN: 1292-8941. DOI: 10.1140/epje/i2002-10075-3 (cit. on pp. 55, 80).

[BTW87] Per Bak, Chao Tang, and Kurt Wiesenfeld. "Self-organized criticality: An explanation of the 1/ f noise." In: *Physical Review Letters* 59.4 (July 1987), pp. 381–384. ISSN: 0031-9007. DOI: 10.1103/PhysRevLett.59.381 (cit. on p. 86).

[Bur+04] Bruno Bureau et al. "Recent advances in chalcogenide glasses." In: *Journal of Non-Crystalline Solids* 345-346 (Oct. 2004), pp. 276–283. ISSN: 00223093. DOI: 10.1016/j.jnoncrysol.2004.08.096 (cit. on p. 1).

[BY13] Caleb W. Brian and Lian Yu. "Surface Self-Diffusion of Organic Glasses." In: *The Journal of Physical Chemistry A* 117.50 (Dec. 2013), pp. 13303–13309. ISSN: 1089-5639. DOI: 10.1021/jp404944s (cit. on p. 2).

[Cao+14] C. R. Cao et al. "Ultrahigh stability of atomically thin metallic glasses." In: *Applied Physics Letters* 105.1 (July 2014), pp. 1–5. ISSN: 00036951. DOI: 10.1063/1.4890113 (cit. on p. 2).

[Cao+15] C. R. Cao et al. "High surface mobility and fast surface enhanced crystallization of metallic glass." In: *Applied Physics Letters* 107.14 (Oct. 2015), p. 141606. ISSN: 0003-6951. DOI: 10.1063/1.4933036 (cit. on p. 2).

[Cav09] Andrea Cavagna. *Supercooled liquids for pedestrians*. 2009. DOI: 10.1016/j.physrep.2009.03.003 (cit. on p. 11).

[CB17] Pinaki Chaudhuri and Ludovic Berthier. "Ultra-long-range dynamic correlations in a microscopic model for aging gels." In: *Physical Review E* 95.6 (June 2017), p. 060601. ISSN: 2470-0045. DOI: 10.1103/PhysRevE.95.060601 (cit. on pp. 53, 55, 80).

[CCM12] Yuriy Chushkin, C. Caronna, and Anders Madsen. "A novel event correlation scheme for X-ray photon correlation spectroscopy." In: *Journal of Applied Crystallography* 45.4 (2012), pp. 807–813. ISSN: 00218898. DOI: 10.1107/S0021889812023321 (cit. on pp. 51, 52, 89).

[Chi76] Ratnam V. Chitturi. "Distribution of Multivariate White Noise Autocorrelations." In: *Journal of the American Statistical Association* 71.353 (Mar. 1976), pp. 223–226. ISSN: 0162-1459. DOI: 10.1080/01621459.1976.10481519 (cit. on p. 104).

[CM91] P. J. Cote and L. V. Meisel. "Self-organized criticality and the Barkhausen effect." In: *Physical Review Letters* 67.10 (1991), pp. 1334–1337. ISSN: 00319007. DOI: 10.1103/PhysRevLett.67.1334 (cit. on p. 85).

[CSN09] Aaron Clauset, Cosma Rohilla Shalizi, and M. E. J. Newman. "Power-Law Distributions in Empirical Data." In: *SIAM Review* 51.4 (Nov. 2009), pp. 661–703. ISSN: 0036-1445. DOI: 10.1137/070710111 (cit. on p. 89).

[Cui+21] Xiao Cui et al. "Effect of natural aging on relaxation behavior and mechanical property of a La-based bulk metallic glass." In: *Intermetallics* 139 (Dec. 2021), p. 107365. ISSN: 09669795. DOI: 10.1016/j.intermet.2021.107365 (cit. on p. 9).

[Das+19] Amlan Das et al. "Stress breaks universal aging behavior in a metallic glass." In: *Nature Communications* 10.1 (Dec. 2019), p. 5006. ISSN: 2041-1723. DOI: 10.1038/s41467-019-12892-1 (cit. on pp. 55, 100, 105).

[Daw+09] Kevin J Dawson et al. "Highly Stable Indomethacin Glasses Resist Uptake of Water Vapor." In: *The Journal of Physical Chemistry B* 113.8 (Feb. 2009), pp. 2422–2427. ISSN: 1520-6106. DOI: 10.1021/jp808838t (cit. on p. 71).

[DBU09] Karin A. Dahmen, Yehuda Ben-Zion, and Jonathan T. Uhl. "Micromechanical Model for Deformation in Solids with Universal Predictions for Stress-Strain Curves and Slip Avalanches." In: *Physical Review Letters* 102.17 (Apr. 2009), p. 175501. ISSN: 0031-9007. DOI: 10.1103/PhysRevLett.102.175501 (cit. on p. 85).

[De 16] Wim H. De Jeu. *Basic X-ray Scattering For Soft Matter*. 1st ed. Oxford: Oxford University Press, 2016, p. 135. ISBN: 978-0-19-872867-2 (cit. on pp. 37–41).

[Die+95] S. B. Dierker et al. "X-Ray Photon Correlation Spectroscopy Study of Brownian Motion of Gold Colloids in Glycerol." In: *Physical Review Letters* 75.3 (July 1995), pp. 449–452. ISSN: 0031-9007. DOI: 10.1103/PhysRevLett.75.449 (cit. on pp. 32, 47).

[DLS20] Thomas Dziuba, Yuansu Luo, and Konrad Samwer. "Local mechanical properties of an ultrastable metallic glass." In: *Journal of Physics: Condensed Matter* 32.34 (Aug. 2020), p. 345101. ISSN: 0953-8984. DOI: 10.1088/1361-648X/ab8aa2 (cit. on pp. 2, 19, 61, 81).

[DM16] P. M. Derlet and Robert Maaß. "The stress statistics of the first pop-in or discrete plastic event in crystal plasticity." In: *Journal of Applied Physics* 120.22 (Dec. 2016), p. 225101. ISSN: 0021-8979. DOI: 10.1063/1.4971871 (cit. on p. 2).

[DMB05] O. Dauchot, G. Marty, and G. Biroli. "Dynamical Heterogeneity Close to the Jamming Transition in a Sheared Granular Material." In: *Physical Review Letters* 95.26 (Dec. 2005), p. 265701. ISSN: 0031-9007. DOI: 10.1103/PhysRevLett.95.265701 (cit. on p. 81).

[DS01] Pablo G Debenedetti and Frank H Stillinger. "Supercooled liquids and the glass transition." In: *Nature* 410.6825 (2001), pp. 259–267. ISSN: 0028-0836. DOI: 10.1038/35065704 (cit. on pp. 11, 60).

[Dur+09] Agnès Duri et al. "Resolving Long-Range Spatial Correlations in Jammed Colloidal Systems Using Photon Correlation Imaging." In: *Physical Review Letters* 102.8 (Feb. 2009), p. 085702. ISSN: 0031-9007. DOI: 10.1103/PhysRevLett.102.085702 (cit. on p. 81).

[DWB21] Devilal Dahal, Hiroka Warren, and Parthapratim Biswas. "On the Origin and Structure of the First Sharp Diffraction Peak of Amorphous Silicon." In: *physica status solidi (b)* 258.9 (Sept. 2021), p. 2000447. ISSN: 0370-1972. DOI: 10.1002/pssb.202000447 (cit. on pp. 2, 11).

[EB03] Takeshi Egami and S.J.L Billinge. *Underneath the Bragg Peaks: Structural Analysis of Complex Materials*. 2nd Editio. June 2003, p. 422. ISBN: 978-0080971339 (cit. on p. 11).

[Edi17] M. D. Ediger. "Perspective: Highly stable vapor-deposited glasses." In: *The Journal of Chemical Physics* 147.21 (Dec. 2017), p. 210901. ISSN: 0021-9606. DOI: 10.1063/1.5006265 (cit. on p. 2).

[Ell90] S. R. Elliott. *Physics of amorphous materials*. Second edi. Longman Group UK Limited, 1990. ISBN: 058202160X (cit. on pp. 1, 17, 21, 32).

[Ell91] S. R. Elliott. "Origin of the first sharp diffraction peak in the structure factor of covalent glasses." In: *Physical Review Letters* 67.6 (Aug. 1991), pp. 711–714. ISSN: 0031-9007. DOI: 10.1103/PhysRevLett.67.711 (cit. on p. 11).

[Eve+15] Zach Evenson et al. "X-Ray Photon Correlation Spectroscopy Reveals Intermittent Aging Dynamics in a Metallic Glass." In: *Physical Review Letters* 115.17 (Oct. 2015), p. 175701. ISSN: 0031-9007. DOI: 10.1103/PhysRevLett.115.175701 (cit. on pp. 3, 55, 68, 76, 80, 100, 105).

[Fak+11] Zahra Fakhraai et al. “Structural variations of an organic glass-former vapor-deposited onto a temperature gradient stage.” In: *Journal of Physical Chemistry Letters* 2.5 (2011), pp. 423–427. ISSN: 19487185. DOI: 10.1021/jz101723d (cit. on p. 2).

[FF08] Zahra Fakhraai and J. A. Forrest. “Measuring the Surface Dynamics of Glassy Polymers.” In: *Science* 319.5863 (Feb. 2008), pp. 600–604. ISSN: 0036-8075. DOI: 10.1126/science.1151205 (cit. on p. 2).

[FIE15] Yue Fan, Takuya Iwashita, and Takeshi Egami. “Crossover from Localized to Cascade Relaxations in Metallic Glasses.” In: *Physical Review Letters* 115.4 (July 2015), p. 045501. ISSN: 0031-9007. DOI: 10.1103/PhysRevLett.115.045501 (cit. on p. 82).

[Fin16] Stefanie Finkhäuser. “Mechanische Spektroskopie an PMMA-Systemen: Nichtlineares Verhalten und UV-aktive Blockcopolymere.” PhD Thesis. Georg-August-University Göttingen, 2016. DOI: 10.53846/goediss-6163 (cit. on p. 1).

[FLG04] Jerome Faillettaz, Francois Louchet, and Jean-Robert Grasso. “Two-Threshold Model for Scaling Laws of Noninteracting Snow Avalanches.” In: *Physical Review Letters* 93.20 (Nov. 2004), p. 208001. ISSN: 0031-9007. DOI: 10.1103/PhysRevLett.93.208001 (cit. on p. 86).

[Gab+03] Xavier Gabaix et al. “A theory of power-law distributions in financial market fluctuations.” In: *Nature* 423.6937 (May 2003), pp. 267–270. ISSN: 0028-0836. DOI: 10.1038/nature01624 (cit. on p. 86).

[Gal+18] Isabella Gallino et al. “Hierarchical aging pathways and reversible fragile-to-strong transition upon annealing of a metallic glass former.” In: *Acta Materialia* 144 (Feb. 2018), pp. 400–410. ISSN: 13596454. DOI: 10.1016/j.actamat.2017.10.060 (cit. on pp. 3, 71, 82).

[GBS15] Jan Gabriel, Thomas Blochowicz, and Bernd Stühn. “Compressed exponential decays in correlation experiments: The influence of temperature gradients and convection.” In: *The Journal of Chemical Physics* 142.10 (Mar. 2015), p. 104902. ISSN: 0021-9606. DOI: 10.1063/1.4914092 (cit. on p. 53).

[Gla63] Roy J. Glauber. “Coherent and Incoherent States of the Radiation Field.” In: *Physical Review* 131.6 (Sept. 1963), pp. 2766–2788. ISSN: 0031-899X. DOI: 10.1103/PhysRev.131.2766 (cit. on p. 45).

[GMR08] Gerhard Grübel, Anders Madsen, and A Robert. "X-Ray Photon Correlation Spectroscopy (XPCS)." In: *Soft Matter Characterization*. Berlin Heidelberg: Springer Netherlands, 2008, pp. 723–782. ISBN: 978-1-4020-4465-6 (cit. on pp. 2, 15, 46).

[Gok+16] Shreyas Gokhale et al. "Localized Excitations and the Morphology of Cooperatively Rearranging Regions in a Colloidal Glass-Forming Liquid." In: *Physical Review Letters* 116.6 (Feb. 2016), p. 068305. ISSN: 0031-9007. DOI: 10.1103/PhysRevLett.116.068305 (cit. on pp. 55, 80).

[Gol69] Martin Goldstein. "Viscous Liquids and the Glass Transition: A Potential Energy Barrier Picture." In: *The Journal of Chemical Physics* 51.9 (Nov. 1969), pp. 3728–3739. ISSN: 0021-9606. DOI: 10.1063/1.1672587 (cit. on p. 11).

[GR16] Valentina M. Giordano and Beatrice Ruta. "Unveiling the structural arrangements responsible for the atomic dynamics in metallic glasses during physical aging." In: *Nature Communications* 7 (Jan. 2016), p. 10344. ISSN: 2041-1723. DOI: 10.1038/ncomms10344 (cit. on p. 55).

[GR54] Beno Gutenberg and Charles Richter. *Seismicity Of The Earth And Associated Phenomena*. Second edi. Princeton, N.J: Princeton University Press, 1954, p. 310 (cit. on pp. 86, 105).

[Gre95] A. Lindsay Greer. "Metallic Glasses." In: *Science* 267.5206 (Mar. 1995), pp. 1947–1953. ISSN: 0036-8075. DOI: 10.1126/science.267.5206.1947 (cit. on pp. 8, 9, 17).

[Guo+11] Xiaoju Guo et al. "Unified approach for determining the enthalpic fictive temperature of glasses with arbitrary thermal history." In: *Journal of Non-Crystalline Solids* 357.16-17 (Aug. 2011), pp. 3230–3236. ISSN: 00223093. DOI: 10.1016/j.jnoncrysol.2011.05.014 (cit. on p. 9).

[GZ04] Gerhard Grübel and Federico Zontone. "Correlation spectroscopy with coherent X-rays." In: *Journal of Alloys and Compounds* 362.1-2 (Jan. 2004), pp. 3–11. ISSN: 09258388. DOI: 10.1016/S0925-8388(03)00555-3 (cit. on pp. 33, 35, 44, 48).

[Har+20] Charles R. Harris et al. "Array programming with NumPy." In: *Nature* 585.7825 (Sept. 2020), pp. 357–362. ISSN: 0028-0836. DOI: 10.1038/s41586-020-2649-2 (cit. on pp. 41, 93).

[Hec+18] Simon Hechler et al. “Microscopic evidence of the connection between liquid-liquid transition and dynamical crossover in an ultraviscous metallic glass former.” In: *Physical Review Materials* 2.8 (Aug. 2018), p. 085603. ISSN: 2475-9953. DOI: 10.1103/PhysRevMaterials.2.085603 (cit. on pp. 3, 53, 55, 68, 80, 110).

[Heu08] Andreas Heuer. “Exploring the potential energy landscape of glass-forming systems: From inherent structures via metabasins to macroscopic transport.” In: *Journal of Physics Condensed Matter* 20.37 (2008). ISSN: 09538984. DOI: 10.1088/0953-8984/20/37/373101 (cit. on pp. 11, 13).

[Hod95] I M Hodge. “Physical aging in polymer glasses.” In: *Science (New York, N.Y.)* 267.5206 (1995), pp. 1945–1947. ISSN: 0036-8075. DOI: 10.1126/science.267.5206.1945 (cit. on pp. 1, 15).

[HP00] Bruno C. Hancock and Michael Parks. “What is the true solubility advantage for amorphous pharmaceuticals?” In: *Pharmaceutical Research* 17.4 (Apr. 2000), pp. 397–404. ISSN: 07248741. DOI: 10.1023/A:1007516718048 (cit. on p. 60).

[HS16] Carlos Herrero Gómez and Konrad Samwer. “Stress and temperature dependence of the avalanche dynamics during creep deformation of metallic glasses.” In: *Scientific Reports* 6.1 (Dec. 2016), p. 33503. ISSN: 2045-2322. DOI: 10.1038/srep33503 (cit. on p. 2).

[Ins83] NORAN Instruments. *Energy-dispersive X-ray microanalysis. An Introduction*. Tech. rep. Middleton, Wisconsin: Ecole polytechnique federale de Lausanne, 1983, p. 68 (cit. on p. 23).

[Kah+09] Annelen Kahl et al. “Dynamical and quasistatic structural relaxation paths in Pd[sub 40]Ni[sub 40]P[sub 20] glass.” In: *Appl. Phys. Lett.* 95.20 (2009), p. 201903. ISSN: 00036951. DOI: 10.1063/1.3266828 (cit. on p. 82).

[KB97] Walter Kob and Jean-Louis Barrat. “Aging Effects in a Lennard-Jones Glass.” In: *Physical Review Letters* 78.24 (June 1997), pp. 4581–4584. ISSN: 0031-9007. DOI: 10.1103/PhysRevLett.78.4581 (cit. on p. 1).

[Kea+07] Kenneth L. Kearns et al. “Influence of substrate temperature on the stability of glasses prepared by vapor deposition.” In: *The Journal of Chemical Physics* 127.15 (Oct. 2007), p. 154702. ISSN: 0021-9606. DOI: 10.1063/1.2789438 (cit. on pp. 2, 60, 70, 71).

[Kea+08] Kenneth L. Kearns et al. “Hiking down the Energy Landscape: Progress Toward the Kauzmann Temperature via Vapor Deposition.” In: *The Journal of Physical Chemistry B* 112.16 (Apr. 2008), pp. 4934–4942. ISSN: 1520-6106. DOI: 10.1021/jp7113384 (cit. on pp. 2, 16, 60, 71).

[Key+07] Aaron S. Keys et al. “Measurement of growing dynamical length scales and prediction of the jamming transition in a granular material.” In: *Nature Physics* 3.4 (Apr. 2007), pp. 260–264. ISSN: 1745-2473. DOI: 10.1038/nphys572 (cit. on p. 81).

[Kir+96] S. Kirsch et al. “Multispeckle autocorrelation spectroscopy and its application to the investigation of ultraslow dynamical processes.” In: *The Journal of Chemical Physics* 104.4 (Jan. 1996), pp. 1758–1761. ISSN: 0021-9606. DOI: 10.1063/1.470761 (cit. on p. 46).

[KLP10] Smarajit Karmakar, Edan Lerner, and Itamar Procaccia. “Statistical physics of the yielding transition in amorphous solids.” In: *Physical Review E - Statistical, Nonlinear, and Soft Matter Physics* 82.5 (Nov. 2010), p. 055103. ISSN: 15393755. DOI: 10.1103/PhysRevE.82.055103 (cit. on p. 85).

[Koh54] Rudolf Kohlrausch. “Theorie des elektrischen Rückstandes in der Leidener Flasche.” In: *Annalen der Physik und Chemie* 167.2 (1854), pp. 179–214. ISSN: 00033804. DOI: 10.1002/andp.18541670203 (cit. on p. 52).

[Koh63] Friedrich Kohlrausch. “Ueber die elastische Nachwirkung bei der Torsion.” In: *Annalen der Physik und Chemie* 195.7 (1863), pp. 337–368. ISSN: 00033804. DOI: 10.1002/andp.18631950702 (cit. on p. 67).

[Kov64] A. J. Kovacs. “Transition vitreuse dans les polymères amorphes. Etude phénoménologique.” In: *Fortschritte der Hochpolymeren-Forschung*. Vol. 3. 3. Berlin, Heidelberg: Springer, Sept. 1964, pp. 394–507. ISBN: 978-3-540-37073-4. DOI: 10.1007/BFb0050366 (cit. on pp. 1, 9, 15, 70).

[Kri+14] Jon-Olaf Krisponeit et al. “Crossover from random three-dimensional avalanches to correlated nano shear bands in metallic glasses.” In: *Nature Communications* 5.1 (Dec. 2014), p. 3616. ISSN: 2041-1723. DOI: 10.1038/ncomms4616 (cit. on pp. 3, 105, 106, 112).

[KSZ15] Johannes Krausser, Konrad Samwer, and Alessio Zaccone. “Interatomic repulsion softness directly controls the fragility of supercooled metallic melts.” In: *Proceedings of the National Academy of Sciences* 112.45 (Nov. 2015), pp. 13762–13767. ISSN: 0027-8424. DOI: 10.1073/pnas.1503741112 (cit. on p. 13).

[Kwa12] Paweł Kwaśniewski. “Probing Dynamics of Hard Sphere Suspensions at High Volume Fractions with Coherent X-rays.” PhD Thesis. Joseph Fourier University, 2012 (cit. on pp. 32, 43, 44).

[KWD60] W. Klement, R. H. Willens, and Pol Duwez. “Non-crystalline Structure in Solidified Gold–Silicon Alloys.” In: *Nature* 187.4740 (Sept. 1960), pp. 869–870. ISSN: 0028-0836. DOI: 10.1038/187869b0 (cit. on p. 1).

[Lag+18] Alexandra E. Lagogianni et al. “Plastic avalanches in the so-called elastic regime of metallic glasses.” In: *The European Physical Journal B* 91.6 (June 2018), p. 104. ISSN: 1434-6028. DOI: 10.1140/epjb/e2018-90051-7 (cit. on pp. 104, 106, 112).

[LC09] Anaël Lemaître and Christiane Caroli. “Rate-dependent avalanche size in athermally sheared amorphous solids.” In: *Physical Review Letters* 103.6 (2009), pp. 1–4. ISSN: 00319007. DOI: 10.1103/PhysRevLett.103.065501 (cit. on p. 3).

[Leh12] Robert L. Leheny. “XPCS: Nanoscale motion and rheology.” In: *Current Opinion in Colloid & Interface Science* 17.1 (Feb. 2012), pp. 3–12. ISSN: 13590294. DOI: 10.1016/j.cocis.2011.11.002 (cit. on p. 46).

[Lei+09] Michael Leitner et al. “Atomic diffusion studied with coherent X-rays.” In: *Nature Materials* 8.9 (2009), pp. 717–720. ISSN: 14764660. DOI: 10.1038/nmat2506 (cit. on p. 47).

[Lei+12] Michael Leitner et al. “Time-resolved study of the crystallization dynamics in a metallic glass.” In: *Physical Review B* 86.6 (Aug. 2012), p. 064202. ISSN: 1098-0121. DOI: 10.1103/PhysRevB.86.064202 (cit. on p. 32).

[Len01] B. Lengeler. “Coherence in X-ray physics.” In: *Naturwissenschaften* 88.6 (June 2001), pp. 249–260. ISSN: 0028-1042. DOI: 10.1007/s001140100221 (cit. on p. 46).

[Leo+10] Edgar Leon-Gutierrez et al. “Size Effects and Extraordinary Stability of Ultrathin Vapor Deposited Glassy Films of Toluene.” In: *The Journal of Physical Chemistry Letters* 1.1 (Jan. 2010), pp. 341–345. ISSN: 1948-7185. DOI: 10.1021/jz900178u (cit. on p. 60).

[LEP13] Ivan Lyubimov, M. D. Ediger, and Juan J. de Pablo. “Model vapor-deposited glasses: Growth front and composition effects.” In: *The Journal of Chemical Physics* 139.14 (Oct. 2013), p. 144505. ISSN: 0021-9606. DOI: 10.1063/1.4823769 (cit. on p. 2).

[LGB15] Weidong Li, Yanfei Gao, and Hongbin Bei. “On the correlation between microscopic structural heterogeneity and embrittlement behavior in metallic glasses.” In: *Scientific Reports* 5.1 (Dec. 2015), p. 14786. ISSN: 2045-2322. DOI: 10.1038/srep14786 (cit. on p. 71).

[LH10] Sébastien Léonard and Peter Harrowell. “Macroscopic facilitation of glassy relaxation kinetics: Ultrastable glass films with front-like thermal response.” In: *Journal of Chemical Physics* 133.24 (2010), pp. 1–12. ISSN: 00219606. DOI: 10.1063/1.3511721 (cit. on p. 2).

[LH91] Edward T. Lu and Russell J. Hamilton. “Avalanches and the distribution of solar flares.” In: *The Astrophysical Journal* 380 (Oct. 1991), p. L89. ISSN: 0004-637X. DOI: 10.1086/186180 (cit. on p. 86).

[Liu+16] Chen Liu et al. “Driving Rate Dependence of Avalanche Statistics and Shapes at the Yielding Transition.” In: *Physical Review Letters* 116.6 (Feb. 2016), p. 065501. ISSN: 0031-9007. DOI: 10.1103/PhysRevLett.116.065501 (cit. on p. 104).

[Liu+17] Chaoren Liu et al. “Sub- T g relaxation times of the α process in metallic glasses.” In: *Journal of Non-Crystalline Solids* 471.June (Sept. 2017), pp. 322–327. ISSN: 00223093. DOI: 10.1016/j.jnoncrysol.2017.06.014 (cit. on pp. 53, 55).

[Lou00] Rodney Loudon. *The quantum theory of light*. Oxford: OUP Oxford, 2000. ISBN: 0198501773 (cit. on p. 45).

[LS87] Randall A. LaViolette and Frank H. Stillinger. “Enumeration of random packings for atomic substances.” In: *Physical Review B* 35.11 (Apr. 1987), pp. 5446–5452. ISSN: 0163-1829. DOI: 10.1103/PhysRevB.35.5446 (cit. on p. 11).

[LSS07] Xiao Gang Lu, Malin Selleby, and Bo Sundman. “Calculations of thermophysical properties of cubic carbides and nitrides using the Debye-Grüneisen model.” In: *Acta Materialia* 55.4 (2007), pp. 1215–1226. ISSN: 13596454. DOI: 10.1016/j.actamat.2006.05.054 (cit. on p. 82).

[Lun+00] Peter Lunkenheimer et al. “Glassy dynamics.” In: *Contemporary Physics* 41.1 (Jan. 2000), pp. 15–36. ISSN: 0010-7514. DOI: 10.1080/001075100181259 (cit. on pp. 2, 14).

[Lun+05] Peter Lunkenheimer et al. “Glassy Aging Dynamics.” In: *Physical Review Letters* 95.5 (July 2005), p. 055702. ISSN: 0031-9007. DOI: 10.1103/PhysRevLett.95.055702 (cit. on p. 71).

[Luo+18] P. Luo et al. “Ultrastable metallic glasses formed on cold substrates.” In: *Nature Communications* 9.1 (2018). ISSN: 20411723. DOI: 10.1038/s41467-018-03656-4 (cit. on p. 60).

[Lüt+18] Martin Lüttich et al. “Anti-Aging in Ultrastable Metallic Glasses.” In: *Physical Review Letters* 120.13 (Mar. 2018), p. 135504. ISSN: 0031-9007. DOI: 10.1103/PhysRevLett.120.135504 (cit. on pp. 3, 4, 19, 55, 60, 61, 71).

[Ma+18] Hai-Tao Ma et al. “The role of Ag, Ca, Zr and Al in strengthening effects of ZK series alloys by altering G.P. zones stability.” In: *Acta Materialia* 147 (Apr. 2018), pp. 42–50. ISSN: 13596454. DOI: 10.1016/j.actamat.2018.01.010 (cit. on p. 71).

[Maa+14] R. Maaß et al. “A single shear band in a metallic glass: Local core and wide soft zone.” In: *Applied Physics Letters* 105.17 (Oct. 2014), p. 171902. ISSN: 0003-6951. DOI: 10.1063/1.4900791 (cit. on p. 105).

[Maa+15] R. Maaß et al. “Long range stress fields and cavitation along a shear band in a metallic glass: The local origin of fracture.” In: *Acta Materialia* 98 (2015), pp. 94–102. ISSN: 13596454. DOI: 10.1016/j.actamat.2015.06.062 (cit. on p. 105).

[Mad+10] Anders Madsen et al. “Beyond simple exponential correlation functions and equilibrium dynamics in x-ray photon correlation spectroscopy.” In: *New Journal of Physics* 12.5 (May 2010), p. 055001. ISSN: 1367-2630. DOI: 10.1088/1367-2630/12/5/055001 (cit. on pp. 53, 55).

[Max67] James Clerk Maxwell. “IV. On the dynamical theory of gases.” In: *Philosophical Transactions of the Royal Society of London* 157 (Dec. 1867), pp. 49–88. ISSN: 0261-0523. DOI: 10.1098/rstl.1867.0004 (cit. on p. 14).

[McK12] Gregory B. McKenna. “Physical Aging in Glasses and Composites.” In: *Long-Term Durability of Polymeric Matrix Composites*. Ed. by K. Pochiraju, G. Tandon, and G. Schoeppner. Boston, MA: Springer US, 2012, pp. 237–309. ISBN: 9789896540821. DOI: 10.1007/978-1-4419-9308-3_7 (cit. on p. 15).

[MFR15] Anders Madsen, Andrei Fluerasu, and Beatrice Ruta. "Structural Dynamics of Materials Probed by X-Ray Photon Correlation Spectroscopy." In: *Synchrotron Light Sources and Free-Electron Lasers*. Cham: Springer International Publishing, 2015, pp. 1–21. ISBN: 978-3-319-04507-8. DOI: 10.1007/978-3-319-04507-8_29-1 (cit. on pp. 2, 46).

[Mic16] Matthieu Micoulaut. "Relaxation and physical aging in network glasses: a review." In: *Reports on Progress in Physics* 79.6 (2016), p. 66504. DOI: 10.1088/0034-4885/79/6/066504 (cit. on p. 1).

[MMS16] Jayachandra Hari Mangalara, Michael D. Marvin, and David S. Simmons. "Three-Layer Model for the Emergence of Ultrastable Glasses from the Surfaces of Supercooled Liquids." In: *The Journal of Physical Chemistry B* 120.21 (June 2016), pp. 4861–4865. ISSN: 1520-6106. DOI: 10.1021/acs.jpcb.6b04736 (cit. on p. 20).

[Moy+76] C T Moynihan et al. "Structural relaxation in vitreous materials." In: *Annals of the New York Academy of Sciences* 279.1 The Glass Tra (Oct. 1976), pp. 15–35. ISSN: 0077-8923. DOI: 10.1111/j.1749-6632.1976.tb39688.x (cit. on p. 52).

[MS17] Gregory B. McKenna and Sindee L. Simon. "50th Anniversary Perspective : Challenges in the Dynamics and Kinetics of Glass-Forming Polymers." In: *Macromolecules* 50.17 (Sept. 2017), pp. 6333–6361. ISSN: 0024-9297. DOI: 10.1021/acs.macromol.7b01014 (cit. on p. 8).

[MZ15] Gregory B. McKenna and Jing Zhao. "Accumulating evidence for non-diverging time-scales in glass-forming fluids." In: *Journal of Non-Crystalline Solids* 407 (Jan. 2015), pp. 3–13. ISSN: 00223093. DOI: 10.1016/j.jnoncrysol.2014.08.012 (cit. on pp. 9, 15).

[New+22] Matt Newville et al. *lmfit/lmfit-py: 1.1.0*. Nov. 2022. DOI: 10.5281/zenodo.7370358 (cit. on p. 92).

[Nga+17] K. L. Ngai et al. "Quantitative explanation of the enhancement of surface mobility of the metallic glass Pd 40 Cu 30 Ni 10 P 20 by the Coupling Model." In: *Journal of Non-Crystalline Solids* 463 (May 2017), pp. 85–89. ISSN: 00223093. DOI: 10.1016/j.jnoncrysol.2017.03.002 (cit. on p. 2).

[Pas+19] Nidhi Pashine et al. "Directed aging, memory, and nature's greed." In: *Science Advances* 5.12 (Dec. 2019), pp. 1–8. ISSN: 2375-2548. DOI: 10.1126/sciadv.aax4215 (cit. on p. 1).

[PDG78] D.E. Polk, C.E. Dube, and B.C. Giessen. "The effect of oxygen additions on the properties of amorphous transition metal alloys." In: *Rapidly Quenched Metals III*. Ed. by B. Cantor. Vol. 1. London: The Metals Society, 1978, p. 220 (cit. on p. 1).

[Per94] Perkin Elmer. *Users Manual 7 Series/UNIX DSC 7 Differential Scanning Calorimeter*. Tech. rep. Norwalk, Connecticut U.S.A., 1994 (cit. on p. 22).

[PS13] Giorgio Parisi and Francesco Sciortino. "Structural glasses: Flying to the bottom." In: *Nature Materials* 12.2 (Jan. 2013), pp. 94–95. ISSN: 1476-1122. DOI: 10.1038/nmat3540 (cit. on pp. 2, 12, 16, 19, 20, 60, 71, 72).

[PT85] R. N. Pusey and R. J. A. Tough. "Particle Interactions." In: *Dynamic light scattering: Applications of Photon Correlation Spectroscopy*. Ed. by Robert Pecora. New York and London: Plenum Press, 1985. Chap. 4, pp. 85–180. ISBN: 0-306-41790-1 (cit. on p. 36).

[RAA15] Zamaan Raza, Björn Alling, and Igor A Abrikosov. "Computer simulations of glasses: the potential energy landscape." In: *Journal of Physics: Condensed Matter* 27.29 (July 2015), p. 293201. ISSN: 0953-8984. DOI: 10.1088/0953-8984/27/29/293201 (cit. on pp. 11, 16, 60).

[RDD03] Ranko Richert, Kalyan Duvvuri, and Lien-Thi Duong. "Dynamics of glass-forming liquids. VII. Dielectric relaxation of supercooled tris -naphthylbenzene, squalane, and decahydroisoquinoline." In: *The Journal of Chemical Physics* 118.4 (Jan. 2003), pp. 1828–1836. ISSN: 0021-9606. DOI: 10.1063/1.1531587 (cit. on p. 70).

[Ric17] Ranko Richert. "Nonlinear dielectric effects in liquids: a guided tour." In: *Journal of Physics: Condensed Matter* 29.36 (Sept. 2017), p. 363001. ISSN: 0953-8984. DOI: 10.1088/1361-648X/aa7cc4 (cit. on p. 2).

[Ric93] Ranko Richert. "Origin of dispersion in dipolar relaxations of glasses." In: *Chemical Physics Letters* 216.1-2 (Dec. 1993), pp. 223–227. ISSN: 00092614. DOI: 10.1016/0009-2614(93)E1251-B (cit. on p. 55).

[Rie+19] Birte Riechers et al. "Ultrastable and polyamorphic states of vapor-deposited 2-methyltetrahydrofuran." In: *The Journal of Chemical Physics* 150.21 (June 2019), p. 214502. ISSN: 0021-9606. DOI: 10.1063/1.5091796 (cit. on pp. 2, 71).

[Rie+22] Birte Riechers et al. “Predicting nonlinear physical aging of glasses from equilibrium relaxation via the material time.” In: *Science Advances* 8.11 (Mar. 2022), pp. 1–9. ISSN: 2375-2548. DOI: 10.1126/sciadv.abl9809 (cit. on pp. 1, 15).

[Rod+22] Cristian Rodriguez-Tinoco et al. “Ultrastable glasses: new perspectives for an old problem.” In: *La Rivista del Nuovo Cimento* 45.5 (May 2022), pp. 325–406. ISSN: 0393-697X. DOI: 10.1007/s40766-022-00029-y (cit. on p. 2).

[RPE17] Beatrice Ruta, Eloi Pineda, and Zach Evenson. “Relaxation processes and physical aging in metallic glasses.” In: *Journal of Physics: Condensed Matter* 29.50 (Dec. 2017), p. 503002. ISSN: 0953-8984. DOI: 10.1088/1361-648X/aa9964 (cit. on pp. 15, 55, 76, 82, 105).

[RS17] Birte Riechers and Konrad Samwer. “Nonlinear response and avalanche behavior in metallic glasses.” In: *The European Physical Journal Special Topics* 226.14 (Aug. 2017), pp. 2997–3021. ISSN: 1951-6355. DOI: 10.1140/epjst/e2017-70087-9 (cit. on p. 2).

[Ruo+04] G Ruoccoa et al. “Landscapes and fragilities.” In: *Journal of Chemical Physics* 120.22 (2004), pp. 10666–10680. DOI: 10.1063/1.1736628 (cit. on p. 13).

[Rut+12] Beatrice Ruta et al. “Atomic-Scale Relaxation Dynamics and Aging in a Metallic Glass Probed by X-Ray Photon Correlation Spectroscopy.” In: *Physical Review Letters* 109.16 (Oct. 2012), p. 165701. ISSN: 0031-9007. DOI: 10.1103/PhysRevLett.109.165701 (cit. on pp. 3, 32, 55, 60).

[Rut+13a] Beatrice Ruta et al. “Compressed correlation functions and fast aging dynamics in metallic glasses.” In: *The Journal of Chemical Physics* 138.5 (Feb. 2013), p. 054508. ISSN: 0021-9606. DOI: 10.1063/1.4790131 (cit. on pp. 53, 80, 82).

[Rut+13b] Beatrice Ruta et al. “Relaxation dynamics and aging in structural glasses.” In: *AIP Conference Proceedings*. Vol. 1518. 2013, pp. 181–188. ISBN: 9780735411418. DOI: 10.1063/1.4794566 (cit. on p. 68).

[Rut+14] Beatrice Ruta et al. “Structural and dynamical properties of Mg65Cu25Y10 metallic glasses studied by in situ high energy X-ray diffraction and time resolved X-ray photon correlation spectroscopy.” In: *Journal of Alloys and Compounds* 615 (Dec. 2014),

S45–S50. ISSN: 09258388. DOI: 10.1016/j.jallcom.2013.12.162 (cit. on p. 68).

[Rut+20] Beatrice Ruta et al. "Wave-Vector Dependence of the Dynamics in Supercooled Metallic Liquids." In: *Physical Review Letters* 125.5 (July 2020), p. 055701. ISSN: 0031-9007. DOI: 10.1103/PhysRevLett.125.055701 (cit. on p. 53).

[San+11] Christopher Sanborn et al. "Direct Measurement of Microstructural Avalanches during the Martensitic Transition of Cobalt Using Coherent X-Ray Scattering." In: *Physical Review Letters* 107.1 (June 2011), p. 015702. ISSN: 0031-9007. DOI: 10.1103/PhysRevLett.107.015702 (cit. on p. 85).

[SB19] Camille Scalliet and Ludovic Berthier. "Rejuvenation and Memory Effects in a Structural Glass." In: *Physical Review Letters* 122.25 (June 2019), p. 255502. ISSN: 0031-9007. DOI: 10.1103/PhysRevLett.122.255502 (cit. on pp. 77, 82).

[Sci05] Francesco Sciortino. "Potential energy landscape description of supercooled liquids and glasses." In: *Journal of Statistical Mechanics: Theory and Experiment* 2005.05 (May 2005), P05015. ISSN: 1742-5468. DOI: 10.1088/1742-5468/2005/05/P05015 (cit. on p. 11).

[SDM01] James P Sethna, Karin A Dahmen, and Christopher R Myers. "Crackling noise." In: *Nature* 410.6825 (Mar. 2001), pp. 242–250. ISSN: 0028-0836. DOI: 10.1038/35065675 (cit. on p. 85).

[SEP13] Sadanand Singh, M. D. Ediger, and Juan J. de Pablo. "Ultrastable glasses from in silico vapour deposition." In: *Nature Materials* 12.2 (Jan. 2013), pp. 139–144. ISSN: 1476-1122. DOI: 10.1038/nmat3521 (cit. on pp. 2, 9, 15, 16, 60, 71).

[Sie43] A. J. F. Siegert. "On the Fluctuations in Signals Returned by Many Independently Moving Scatters." In: *MIT Radiation Laboratory Report* 465 (1943) (cit. on p. 46).

[SJ21] Ekhard K. H. Salje and Xiang Jiang. "Crackling noise and avalanches in minerals." In: *Physics and Chemistry of Minerals* 48.5 (May 2021), p. 22. ISSN: 0342-1791. DOI: 10.1007/s00269-021-01138-6 (cit. on pp. 85, 86).

[SP11] Sadanand Singh and Juan J. de Pablo. "A molecular view of vapor deposited glasses." In: *The Journal of Chemical Physics* 134.19 (May 2011), p. 194903. ISSN: 0021-9606. DOI: 10.1063/1.3586805 (cit. on pp. 2, 60).

[Sti95] Frank H. Stillinger. "A Topographic View of Supercooled Liquids and Glass Formation." In: *Science (New York, N.Y.)* 267.5206 (1995), pp. 1935–1939 (cit. on pp. 11, 13, 60).

[Str77] Leendert Cornelis Elisa Struik. "Physical aging in amorphous polymers and other materials." PhD Thesis. Delft University of Technology, Apr. 1977. ISBN: 0444416552 (cit. on pp. 1, 15).

[Sut+91] Mark Sutton et al. "Observation of speckle by diffraction with coherent X-rays." In: *Nature* 352.6336 (Aug. 1991), pp. 608–610. ISSN: 0028-0836. DOI: 10.1038/352608a0 (cit. on pp. 32, 46).

[SW84] Frank H. Stillinger and Thomas A. Weber. "Packing Structures and Transitions in Liquids and Solids." In: *Science* 225.4666 (Sept. 1984), pp. 983–989. ISSN: 0036-8075. DOI: 10.1126/science.225.4666.983 (cit. on p. 11).

[Swa+07] Stephen F. Swallen et al. "Organic Glasses with Exceptional Thermodynamic and Kinetic Stability." In: *Science (New York, N.Y.)* 315.5810 (Jan. 2007), pp. 353–6. ISSN: 1095-9203. DOI: 10.1126/science.1135795 (cit. on pp. 1, 2, 16, 20, 59, 60).

[Swa+08] Stephen F. Swallen et al. "Molecular view of the isothermal transformation of a stable glass to a liquid." In: *The Journal of Chemical Physics* 128.21 (June 2008), p. 214514. ISSN: 0021-9606. DOI: 10.1063/1.2919570 (cit. on p. 60).

[SWS07] Peter Schall, D. A. Weitz, and Frans Spaepen. "Structural Rearrangements That Govern Flow in Colloidal Glasses." In: *Science* 318.5858 (Dec. 2007), pp. 1895–1899. ISSN: 0036-8075. DOI: 10.1126/science.1149308 (cit. on p. 3).

[Thu+96] T. Thurn-Albrecht et al. "Photon correlation spectroscopy of colloidal palladium using a coherent x-ray beam." In: *Physical Review Letters* 77.27 (1996), pp. 5437–5440. ISSN: 10797114. DOI: 10.1103/PhysRevLett.77.5437 (cit. on p. 47).

[TV18] Lin Tian and Cynthia A. Volkert. "Measuring Structural Heterogeneities in Metallic Glasses Using Transmission Electron Microscopy." In: *Metals* 8.12 (Dec. 2018), p. 1085. ISSN: 2075-4701. DOI: 10.3390/met8121085 (cit. on p. 3).

[Van54] Léon Van Hove. "Correlations in Space and Time and Born Approximation Scattering in Systems of Interacting Particles." In: *Physical Review* 95.1 (July 1954), pp. 249–262. ISSN: 0031-899X. DOI: 10.1103/PhysRev.95.249 (cit. on p. 15).

[VGT00] Paul M. Voyles, J. M. Gibson, and M. M. J. Treacy. "Fluctuation microscopy: a probe of atomic correlations in disordered materials." In: *Journal of Electron Microscopy* 49.2 (Jan. 2000), pp. 259–266. ISSN: 0022-0744. DOI: 10.1093/oxfordjournals.jmicro.a023805 (cit. on p. 3).

[Vir+20] Pauli Virtanen et al. "SciPy 1.0: Fundamental Algorithms for Scientific Computing in Python." In: *Nature Methods* 17 (2020), pp. 261–272. DOI: 10.1038/s41592-019-0686-2 (cit. on pp. 67, 90).

[Viv+94] Eduard Vives et al. "Distributions of avalanches in martensitic transformations." In: *Physical Review Letters* 72.11 (Mar. 1994), pp. 1694–1697. ISSN: 0031-9007. DOI: 10.1103/PhysRevLett.72.1694 (cit. on p. 85).

[Wag+11] Hannes Wagner et al. "Local elastic properties of a metallic glass." In: *Nature Materials* 10.6 (June 2011), pp. 439–442. ISSN: 1476-1122. DOI: 10.1038/nmat3024 (cit. on p. 2).

[Wan+15] X.D. Wang et al. "Free-volume dependent atomic dynamics in beta relaxation pronounced La-based metallic glasses." In: *Acta Materialia* 99 (Oct. 2015), pp. 290–296. ISSN: 13596454. DOI: 10.1016/j.actamat.2015.08.010 (cit. on pp. 68, 70).

[Wan+16] J. Q. Wang et al. "Increasing the kinetic stability of bulk metallic glasses." In: *Acta Materialia* 104 (Feb. 2016), pp. 25–32. ISSN: 13596454. DOI: 10.1016/j.actamat.2015.11.048 (cit. on p. 60).

[Wan12] Wei Hua Wang. "The elastic properties, elastic models and elastic perspectives of metallic glasses." In: *Progress in Materials Science* 57.3 (Apr. 2012), pp. 487–656. ISSN: 00796425. DOI: 10.1016/j.pmatsci.2011.07.001 (cit. on pp. 8, 60, 71).

[Was+08] Yoshio Waseda et al. "On the glass forming ability of liquid alloys." In: *Science and Technology of Advanced Materials* 9.2 (Apr. 2008), p. 023003. ISSN: 1468-6996. DOI: 10.1088/1468-6996/9/2/023003 (cit. on p. 10).

[Wel+13] Roger C. Welch et al. "Dynamics of Glass Relaxation at Room Temperature." In: *Physical Review Letters* 110.26 (June 2013), p. 265901. ISSN: 0031-9007. DOI: 10.1103/PhysRevLett.110.265901 (cit. on p. 16).

[WLG05] Wei Hua Wang, J.J. Lewandowski, and A. Lindsay Greer. "Understanding the Glass-forming Ability of Cu50Zr50 Alloys in Terms of a Metastable Eutectic." In: *Journal of Materials Research* 20.09 (Sept. 2005), pp. 2307–2313. ISSN: 0884-2914. DOI: 10.1557/jmr.2005.0302 (cit. on p. 1).

[Woj+09] Z. Wojnarowska et al. "Broadband dielectric relaxation study at ambient and elevated pressure of molecular dynamics of pharmaceutical: indomethacin." In: *Journal of Physical Chemistry B* 113.37 (2009), pp. 12536–12545. ISSN: 15206106. DOI: 10.1021/jp905162r (cit. on p. 1).

[Wu+18] Zhen Wei Wu et al. "Stretched and compressed exponentials in the relaxation dynamics of a metallic glass-forming melt." In: *Nature Communications* 9.1 (Dec. 2018), p. 5334. ISSN: 2041-1723. DOI: 10.1038/s41467-018-07759-w (cit. on pp. 53, 55).

[WW70] Graham Williams and David C. Watts. "Non-symmetrical dielectric relaxation behaviour arising from a simple empirical decay function." In: *Transactions of the Faraday Society* 66.1 (1970), p. 80. ISSN: 0014-7672. DOI: 10.1039/tf9706600080 (cit. on pp. 52, 67).

[Xue+16] R. J. Xue et al. "Enhanced kinetic stability of a bulk metallic glass by high pressure." In: *Applied Physics Letters* 109.22 (Nov. 2016), p. 221904. ISSN: 0003-6951. DOI: 10.1063/1.4968834 (cit. on pp. 60, 70).

[Yan+21] Fan Yang et al. "Periodic island-layer-island growth during deposition of ultrastable metallic glasses." In: *Communications Materials* 2.1 (Dec. 2021), p. 75. ISSN: 2662-4443. DOI: 10.1038/s43246-021-00180-9 (cit. on p. 20).

[YL03] H Yardimci and R. L Leheny. "Memory in an aging molecular glass." In: *Europhysics Letters (EPL)* 62.2 (Apr. 2003), pp. 203–209. ISSN: 0295-5075. DOI: 10.1209/epl/i2003-00347-0 (cit. on p. 77).

[YLS13] Hai-Bin Yu, Yuansu Luo, and Konrad Samwer. "Ultrastable metallic glass." In: *Advanced Materials* 25.41 (2013), pp. 5904–5908. ISSN: 09359648. DOI: 10.1002/adma.201302700 (cit. on pp. 2, 16, 19, 20, 60–62).

[Yu+13] Hai-Bin Yu et al. "Chemical influence on β-relaxations and the formation of molecule-like metallic glasses." In: *Nature Communications* 4.July (July 2013), p. 2204. ISSN: 2041-1723. DOI: 10.1038/ncomms3204 (cit. on p. 72).

[Zap+98] Stefano Zapperi et al. “Dynamics of a ferromagnetic domain wall: Avalanches, depinning transition, and the Barkhausen effect.” In: *Physical Review B* 58.10 (Sept. 1998), pp. 6353–6366. ISSN: 0163-1829. DOI: 10.1103/PhysRevB.58.6353 (cit. on p. 85).

[Zha+17] Kai Zhang et al. “Ultrastable Amorphous Sb 2 Se 3 Film.” In: *The Journal of Physical Chemistry B* 121.34 (Aug. 2017), pp. 8188–8194. ISSN: 1520-6106. DOI: 10.1021/acs.jpcb.7b03408 (cit. on p. 2).

[Zha+22] Yong Zhao et al. “Ultrastable metallic glass by room temperature aging.” In: *Science Advances* 8.33 (Aug. 2022), pp. 1–9. ISSN: 2375-2548. DOI: 10.1126/sciadv.abn3623 (cit. on pp. 1, 2, 81, 110).

[Zhe+19] Qiuju Zheng et al. “Understanding Glass through Differential Scanning Calorimetry.” In: *Chemical Reviews* 119.13 (July 2019), pp. 7848–7939. ISSN: 0009-2665. DOI: 10.1021/acs.chemrev.8b00510 (cit. on pp. 2, 21, 22).